



Aeromagnetic Solutions Incorporated

**Coherence of the geomagnetic field and implications for noise
reduction using mesospheric magnetometry**

J. Bradley Nelson

Date: Sept 2016

Contract #: NICOP - N62909-15-1-2054

Report #: ASI-2016- 9 (N62909-15-1-2054-Task 1)

DISTRIBUTION STATEMENT A. Approved for public release; distribution is unlimited

REPORT DOCUMENTATION PAGE					Form Approved OMB No. 0704-0188	
<p>The public reporting burden for this collection of information is estimated to average 1 hour per response, including the time for reviewing instructions, searching existing data sources, gathering and maintaining the data needed, and completing and reviewing the collection of information. Send comments regarding this burden estimate or any other aspect of this collection of information, including suggestions for reducing the burden, to Department of Defense, Washington Headquarters Services, Directorate for Information Operations and Reports (0704-0188), 1215 Jefferson Davis Highway, Suite 1204, Arlington, VA 22202-4302. Respondents should be aware that notwithstanding any other provision of law, no person shall be subject to any penalty for failing to comply with a collection of information if it does not display a currently valid OMB control number.</p> <p>PLEASE DO NOT RETURN YOUR FORM TO THE ABOVE ADDRESS.</p>						
1. REPORT DATE (DD-MM-YYYY)		2. REPORT TYPE		3. DATES COVERED (From - To)		
09/01/2016		Technical Report #1		July 2015 - September 2016		
4. TITLE AND SUBTITLE Coherence of the geomagnetic field and implications for noise reduction using mesospheric magnetometry				5a. CONTRACT NUMBER		
				5b. GRANT NUMBER N62909-15-1-2054		
				5c. PROGRAM ELEMENT NUMBER		
6. AUTHOR(S) J. Bradley Nelson				5d. PROJECT NUMBER 1000002333		
				5e. TASK NUMBER Task 1		
				5f. WORK UNIT NUMBER		
7. PERFORMING ORGANIZATION NAME(S) AND ADDRESS(ES) Aeromagnetic Solutions Incorporated 2486 Orient Park Drive Gloucester, ON, Canada, K1B5L9				8. PERFORMING ORGANIZATION REPORT NUMBER ASI-2016- 9 (N62909-15-1-2054-Task 1)		
9. SPONSORING/MONITORING AGENCY NAME(S) AND ADDRESS(ES) Office of Naval Research Global 86 Blenheim Crescent Ruislip, MIDDX HA4 7HB United Kingdom				10. SPONSOR/MONITOR'S ACRONYM(S) ONRG		
				11. SPONSOR/MONITOR'S REPORT NUMBER(S)		
12. DISTRIBUTION/AVAILABILITY STATEMENT DISTRIBUTION STATEMENT A. Approved for public release; distribution is unlimited						
13. SUPPLEMENTARY NOTES						
14. ABSTRACT ONR Code 321 funded FASORtronics LLC to demonstrate the ability to measure high-altitude magnetic fields using ground-based laser-excitation of Sodium ions in the ionosphere (contract N00014-14-C-0110). The aim of the project was to determine if the magnetic field variations measured at high-altitude can be used for geomagnetic noise cancellation in airborne magnetic anomaly detection (MAD) systems. Aeromagnetics Solutions Incorporated was awarded NICOP N62909-15-1-2054 to assist with the experimental setup, determine the coherence between the groundstation measurements, and evaluate several geomagnetic noise reduction algorithms. This report describes this work.						
15. SUBJECT TERMS magnetic anomaly detection (MAD), geomagnetic field, coherence, magnetic noise reduction, mesosphere, remote magnetometry						
16. SECURITY CLASSIFICATION OF:			17. LIMITATION OF ABSTRACT	18. NUMBER OF PAGES	19a. NAME OF RESPONSIBLE PERSON	
a. REPORT	b. ABSTRACT	c. THIS PAGE			J. Bradley Nelson	
U	U	U	UU	61	19b. TELEPHONE NUMBER (Include area code) 1-613-841-4640	

Table of Contents

Table of Contents	2
1. Introduction	3
2. Groundstation magnetic measurements July 2015	4
2.1 Locations of groundstations.....	4
2.2 Equipment used	9
2.3 Data pre-processing	10
2.4 Coherence analysis for the July 11-12 and July 12-13 data	11
2.5 Noise cancellation algorithms and results for July 11-12 and 12-13	15
3. Groundstation magnetic measurements October 2015	19
3.1 Locations of the groundstations	19
3.2 Coherence analysis for the Oct 8-9 data.....	21
3.3 Noise cancellation results for Oct 8-9 data.....	22
4. Conclusions	24
References	26
Appendix A: Time and frequency-domain plots of all groundstation vs. groundstation noise cancellation and coherence analysis.....	27
A.1 Night of Jul 11-12	27
A.2 Night of July 12-13	40
A.3 Night of July Oct 8-9	52

1. Introduction

ONR Code 321 is funding FASORtronics LLC in collaboration with the University of Arizona to demonstrate the ability to measure high-altitude magnetic fields using ground-based laser-excitation of Sodium ions in the ionosphere (contract N00014-14-C-0110). The aim of the project is to determine if the magnetic field variations measured at high-altitude can be used for geomagnetic noise cancellation in airborne magnetic anomaly detection (MAD) systems. FASORtronics specializes in the design and manufacture of laser systems to create “guide stars” for astronomical telescopes incorporating adaptive optics. They have expertise in making the high power, single frequency, solid-state lasers and wavelength converters that form the foundation of the Frequency Addition Source of Optical Radiation (FASOR) concept. Two high power single-frequency infrared laser beams are mixed in a non-linear crystal to produce a single-frequency yellow output beam resonant with high-altitude Sodium atoms. A full description of the FASORtronics equipment, experimental setup, calibration, etc. is beyond the scope of this report. However, such information is expected to be contained in the FASORtronics’ final report on contract N00014-14-C-0110.

Aeromagnetics Solutions Incorporated has extensive experience in MAD noise reduction processing (Ref 1), and was awarded NICOP N62909-15-1-2054 to assist with the experimental setup, determine the coherence between the groundstation measurements, and to access a variety of time and frequency-domain methods for noise cancellation between groundstation measurements. If the mesospheric magnetic measurements obtained by FASORtronics have low enough noise levels to discern geomagnetic variations, then the NICOP would also include analysis of the mesospheric and groundstation magnetic measurement to quantify mesospheric-to-groundstation coherence and noise reduction performance.

The mesospheric measurements are made at an altitude of approximately 100 km above the Earth’s surface where the Sodium ions exist (Ref 2), while a groundstation is necessarily located on the Earth’s surface. This is a significant separation and in order to appreciate the potential for mesospheric-groundstation coherence/noise cancellation performance, it is important to understand what the magnetic field relationships are over similar horizontal distances on the ground. That is, if the signals measured at two groundstations separated by 100 km are not coherent, then it will not be surprising if the signals measured in the mesosphere and groundstation are not coherent. However, if there is extremely-high coherence between signals measured at two groundstations separated by > 100 km, then we might expect significant coherence between the mesosphere and groundstation signals.

To determine the coherence of the geomagnetic field as a function of horizontal separation and the noise reduction performance of various time and frequency-domain algorithms, groundstation magnetometers were set up at various locations in Arizona to collect long segments of geomagnetic data. Total-magnetic field (TF) and component magnetic field (X,Y,Z) data were recorded at four groundstations during the night of July 11-12 and July 12-13, 2015. The FASORtronics guide star system was operated at the Stewart Observatory Kuiper Telescope on Mt. Bigelow, near Tucson AZ on these same nights. They were able to optimize the performance of their laser system on these nights, but bad weather prevented them from making any mesospheric magnetic measurements. Section 2 describes the groundstation experiment in detail and gives the results of the groundstation-to-groundstation coherence and noise-reduction analysis.

Based on these results, new secure groundstation locations were chosen for the next experiment in October 2015. These locations were chosen to ensure the horizontal separations were adequate to

determine coherence of the geomagnetic field over distances > 100 km, and to eliminate the requirement for someone to safeguard the groundstation sensors during the measurements.

On the night of Oct 8-9, 2015, FASORtronics operated their guide star system at the Stewart Observatory. This night was chosen based on predictions of high geomagnetic field activity obtained from Ref 3 in order to ensure a large signal-to-noise ratio for the mesospheric measurements. Unfortunately, drift in their reference oscillator masked any geomagnetic signals in their data. However, the groundstations were set up at the new locations and TF and (X,Y,Z) components of the geomagnetic field were recorded. Section 3 describes this experiment in detail and gives the results of the groundstation-to-groundstation coherence and noise-reduction analysis.

On Dec 20-22, 2015 FASORtronics again attempted to gather mesospheric magnetic measurements at the Stewart Observatory, but again bad weather occurred. No groundstations were set up for this experiment, but data from the Tucson Geomagnetic Observatory were available.

On March 24-25, 2016 FASORtronics again attempted to collect gather mesospheric magnetic measurements at the Stewart Observatory. They had replaced their reference oscillator and so had solved their drift issues. Unfortunately the geomagnetic field was very quiet on that night so it was only possible to make a measurement of the average DC magnetic field in the mesosphere, not the time variations of that field. Those measurements used the last of the funds from contract N00014-14-C-0110 so it is unlikely that any further mesospheric measurements will be done before the end date of Aeromagnetic Solutions Incorporated's NICOP. Consequently, this report addresses only the coherence of the geomagnetic field between groundstations and the noise reduction analysis performed on those data. Section 4 contains the conclusions drawn from this work.

2. Groundstation magnetic measurements July 2015

2.1 Locations of groundstations

Three of the groundstations were in the same locations for both the night of July 11-12 and July 12-13. These were the United States Geological Survey (USGS) Tucson Geomagnetic Observatory (denoted TUC1 and TUC2 in the remainder of this report), the Stewart Observatory (denoted ST1 and ST2), and the Kearney, AZ airport (denoted K1 and K2). On the night of July 11-12, the fourth groundstation was located south of Peridot, AZ (denoted P) and on the night of July 12-13, this groundstation was moved to the Tinto National Forest (denoted T). Figure 1 shows these five locations as well as the spot directly beneath where the FASORtronics laser illuminated the mesosphere for all of their testing. Figures 2-6 show close-up views of each of the groundstation locations with distances to the nearest roads, etc. marked.

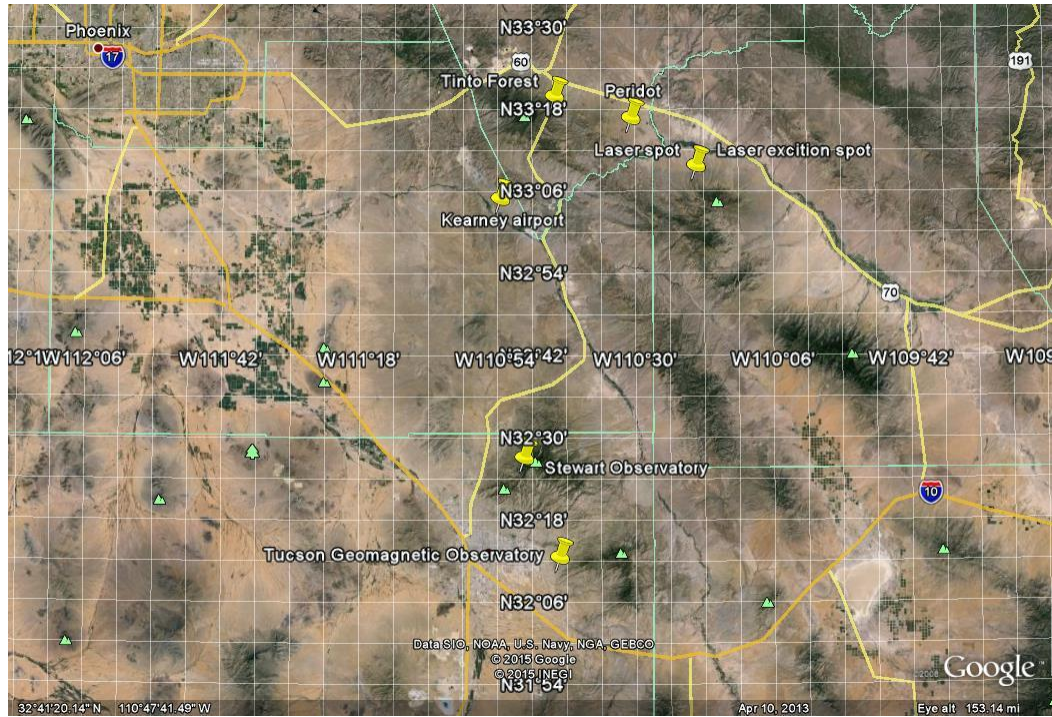


Figure 1. Locations of the five groundstations and the spot directly beneath where the FASORtrons laser illuminated the mesosphere.

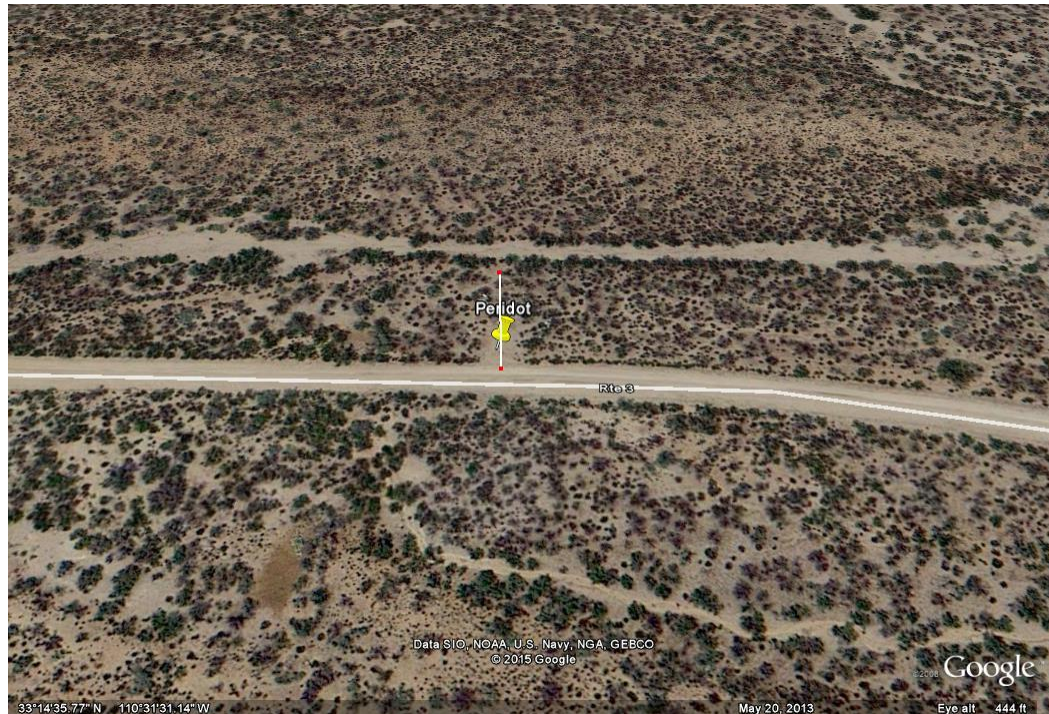


Figure 2. Close-up view of the Peridot groundstation location. Sensor = 30 m north of Route 3 (gravel road).

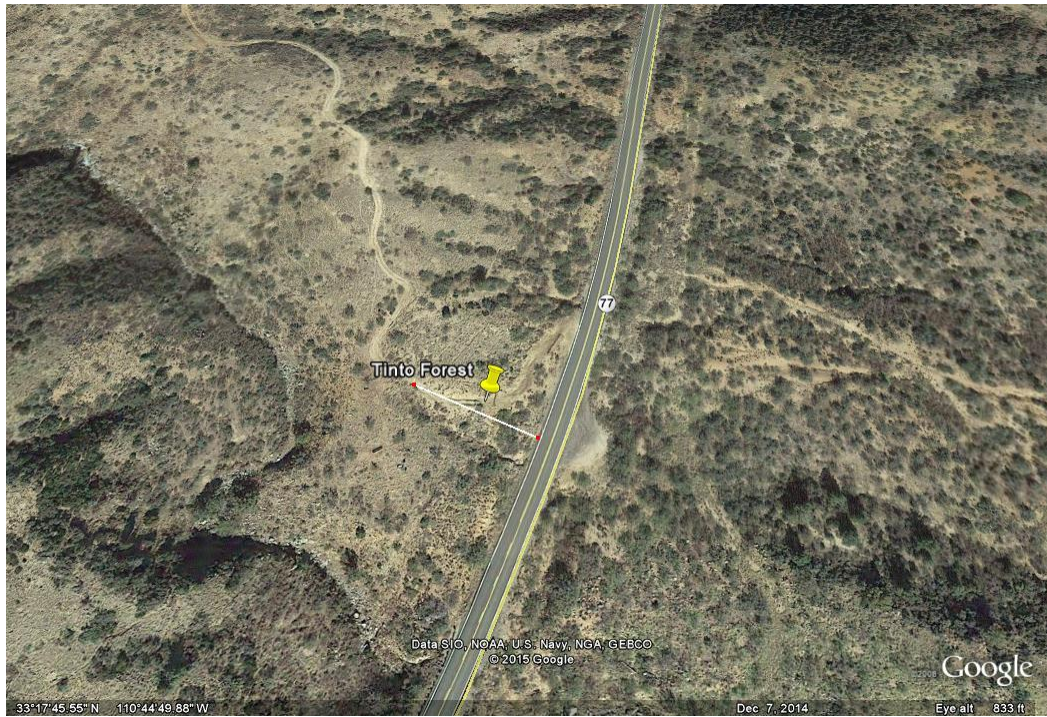


Figure 3. Close-up view of the Tinto Forest groundstation location. Sensor = 50 m west of Highway 77 (asphalt road) on a gravel Forestry road.



Figure 4. Close-up view of the Kearney Airport groundstation location. Sensor = 270 m south of railway; 40 m south of the turning ramp; 115 m south of Airport Road (gravel).

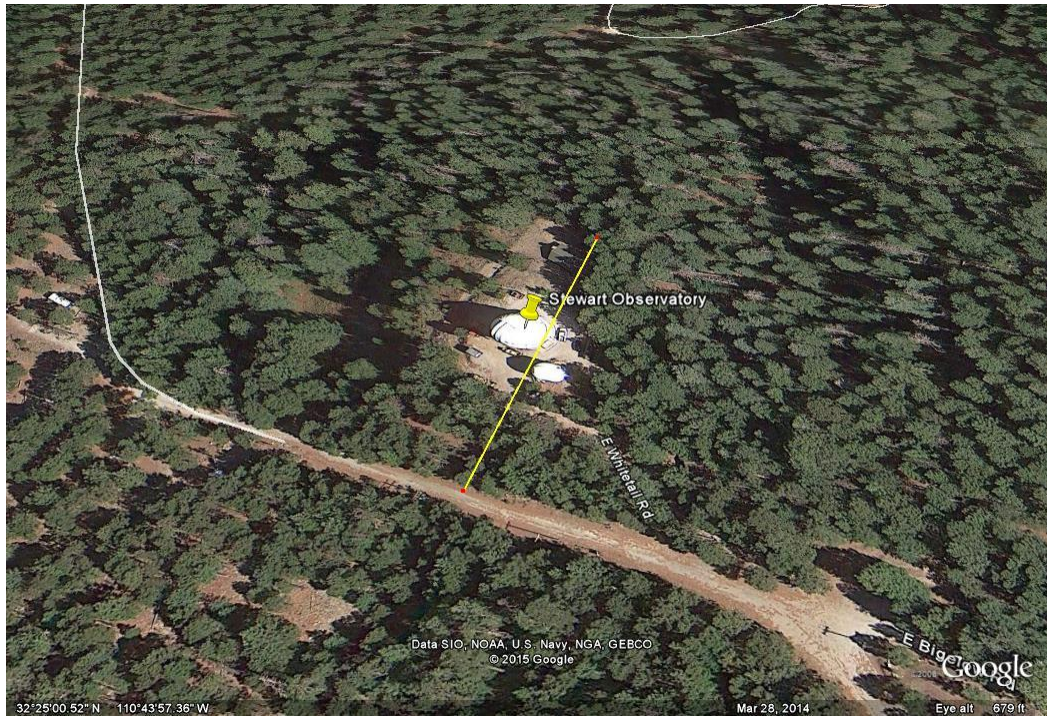


Figure 5. Close-up view of the Stewart Observatory groundstation location. Sensor = 115 m north of gravel road; 50 m north of the Observatory; 15 m north of the dormitory.

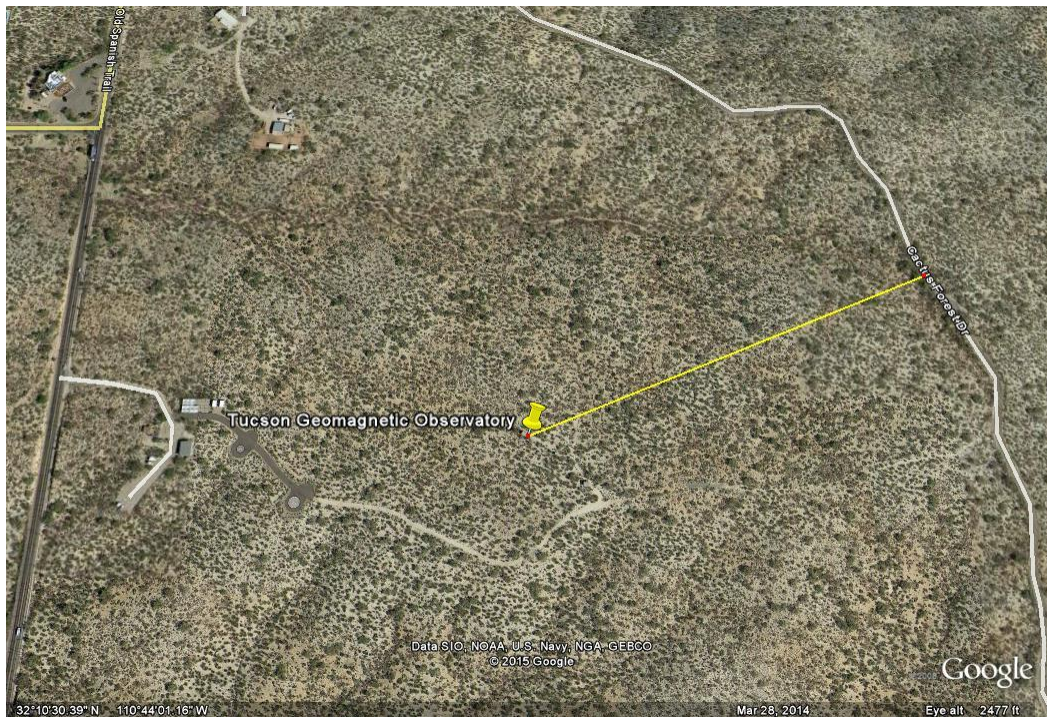


Figure 6. Close-up view of the Tucson USGS Observatory groundstation location. Sensor = 270 m east of Observatory buildings; 400 m from Old Spanish Trail (asphalt street); 400 west of Cactus Forest Drive (asphalt street).

The exact coordinates for each location are given in Table 1. Table 2 gives the horizontal separation of each of these 6 points from each other.

Table 1. Coordinates for the five groundstation locations and the FASORtronics laser excitation point for the July 2015 trials.

Location	Denoted	Latitude (°N)	Longitude (°W)
Laser excitation point	L	33.1270	110.3360
Peridot	P	33.2433	110.5254
Tinto Forrest	T	33.2958	110.7474
Kearney Airport	K1 (July 11-12) K2 (July 12-13)	33.0464	110.9051
Stewart Observatory	ST1 (July 11-12) ST2 (July 12-13)	32.4169	110.7326
Tucson USGS Observatory	TUC1 (July 11-12) TUC2 (July 12-13)	32.1745	110.7337

Table 2. Horizontal separation of the five groundstation locations and the FASORtronics laser excitation point for the July 2015 trials.

Location	Distance (km)					
	Laser excitation point	Peridot	Tinto Forest	Kearney Airport	Stewart Observatory	Tucson USGS Observatory
Laser excitation point	0	22	43	54	87	112
Peridot	22	0	21	42	94	120
Tinto Forrest	43	21	0	31	98	125
Kearney Airport	54	42	31	0	72	98
Stewart Observatory	87	94	98	72	0	27
Tucson USGS Observatory	112	120	125	98	27	0

Tables 3 is a subset of the data in Table 2, showing the separation of the groundstations for the night of July 11-12: Table 4 shows the same quantities for the night of July 12-13.

Table 3. Separation of various groundstations for the night of July 11-12.

	Distance (km)			
Location	P	K1	ST1	TUC1
P	0	42	94	120
K1	42	0	72	98
ST1	94	72	0	27
TUC1	120	98	27	0

Table 4. Separation of various groundstations for the night of July 12-13.

	Distance (km)			
Location	T	K2	ST2	TUC2
T	0	31	98	125
K2	31	0	72	98
ST2	98	72	0	27
TUC2	125	98	27	0

2.2 Equipment used

The Kearney (K1 & K2), Peridot (P), and Tinto Forest (T) groundstations were supplied by the USGS and consisted of:

- NAROD 3-axis vector magnetometer to measure the magnetic field components
- a 12 Volt car battery to supply power
- an electronics box containing
 - a single-board computer to collect the data
 - a National Instruments CompactRIO data acquisition system including a 24-bit A/D card
 - a GPS receiver to tag the data with UTC time
 - a USB thumbdrive to store the data.

The X,Y,Z data were sampled at 1000 Hz, but boxcar-filtered down to 100 Hz, then boxcar-filtered down to 10 Hz, then boxcar-filtered down to 1 Hz. The analysis in this report was performed using the 1 Hz UTC-time-tagged vector component data. The total-field (TF) was created from the equation:

$$TF = \sqrt{X^2 + Y^2 + Z^2} \quad .$$

The Tucson Geomagnetic Observatory equipment, described in more detail in Ref 4, consists of:

- a tri-axial NAROD fluxgate magnetometer for gathering X,Y,Z data
- a proton magnetometer that measures the total magnetic field (TF).

The data were recorded at 1 Hz and time-stamped with UTC, which was obtained from a GPS receiver. The data were obtained from Ref 5.

The Stewart Observatory groundstation consisted of a Geometrics G823 Cesium total-field magnetometer with an RS-232 output. The sample rate was nominally 10 Hz, based on the internal oscillator in the sensor electronics. However, a laptop running REALTERM.EXE was used to record the digital data and a time signal from the laptop's clock was added to the RS-232 data stream for each data point recorded. A Symmetricom NTP100-GPS timing unit was connected to the laptop in order to keep the computer's time synchronized with to UTC, but unfortunately the software was not set up correctly. Thus the time-stamp on the ST1 and ST2 data had to be adjusted based on its correlation with the TUC1 and TUC2 signals. (see Section 2.3)

2.3 Data pre-processing

All data analysis was conducted using the commercial software IDL, and the analysis procedures were written by Aeromagnetic Solutions Incorporated. The data pre-processing steps consisted of:

- 1) visually inspecting/correcting the magnetic data from each groundstation as required to eliminate spikes, steps, and glitches.
- 2) comparing the Peridot (P) and Stewart Observatory (ST1 & ST2) magnetic data with log notes to determine when vehicles passing on the road generated magnetic anomalies. Akima splines or linear interpolations were used to remove these known anomalies.
- 3) comparing the magnetic data from all groundstations to determine if there were any train signatures present in the Kearney Airport (K1 & K2) data, and if so, removing them with Akima splines or linear interpolations.
- 4) comparing the magnetic data from all groundstations to determine if there were any vehicle signatures present in the Tinto Forest (T) data, and if so, removing them with Akima splines or linear interpolations.
- 5) correcting the time-stamp on the ST1 data by calculating the lag that produced the highest correlation with the TUC1 data. The ST1 data were collected with the G823 electronics inside a plastic bag along with the GPS electronics and the laptop, which caused the G823 electronics to become very hot. The purpose of the bag was keep rain out of the electronics and connections. The correlation between ST1 and TUC1 data was quite poor unless the average sample rate was assumed to be 10.000513 Hz instead of 10 Hz. A synthetic time-stamp for the ST1 data was generated assuming a true sample rate of 10.000513 Hz and an offset from UTC of 4 hours + 20 seconds.
- 6) the ST2 data were collected with the G823 electronics in a separate plastic bag, which resulted in the electronics staying much cooler. A similar correlation analysis vs. the TUC2 data showed that the sample rate could be assumed to be exactly 10 Hz, and the offset from UTC was 4 hours + 27 seconds. Thus a synthetic time-stamp for the ST2

data was generated assuming a true sample rate of 10 Hz and an offset from UTC of 4 hours + 27 seconds.

7) the ST1 and ST2 data were filtered with a 4th-order digital Bessel filter with a 3 dB point at 1 Hz. The resulting signal was time-reversed and passed through the same filter a second time. The output was then time-reversed again, which resulted in an 8th-order filter with a 3-dB point at 1 Hz, but with no phase delay compared to the original data.

8) the start and end times when all groundstations were operating were identified.

9) all groundstation data were re-sampled to exactly 1 Hz between those start and end times.

This produced time-aligned groundstation X,Y,Z,TF data for TUC1, K1, and P, and only TF for ST1 for the night of July 11-12. Time-aligned groundstation X,Y,Z,TF data for TUC2, K2, and T, and only TF for ST2 were created for the night of July 12-13. These data sets were used in the coherence and noise cancellation analyses described in sections 2.4 and 2.5..

2.4 Coherence analysis for the July 11-12 and July 12-13 data

Each 1 Hz file was high-pass filtered with a 4th-order digital Bessel filter with a 3 dB point at 0.001 Hz. The first 3000 data points (50 minutes) were not used in any of the subsequent analyses in order to avoid any ringing in the filters.

Two coherence calculations were performed:

1) TF_a vs. TF_b

2) TF_a vs. $(X,Y,Z)_b$

where the subscript “a” and “b” refer to the various groundstations. For example, if a = TUC1, then b could be ST1, K1, or P. All combinations of groundstation coherence were calculated. Figure 7 shows a typical example of the coherence calculated for TF_a vs. TF_b .

The coherence drops off very quickly above approximately 0.03 Hz. The reason is that the amplitudes of the geomagnetic signals also drop off very quickly above 0.03 Hz as shown in Figure 8.

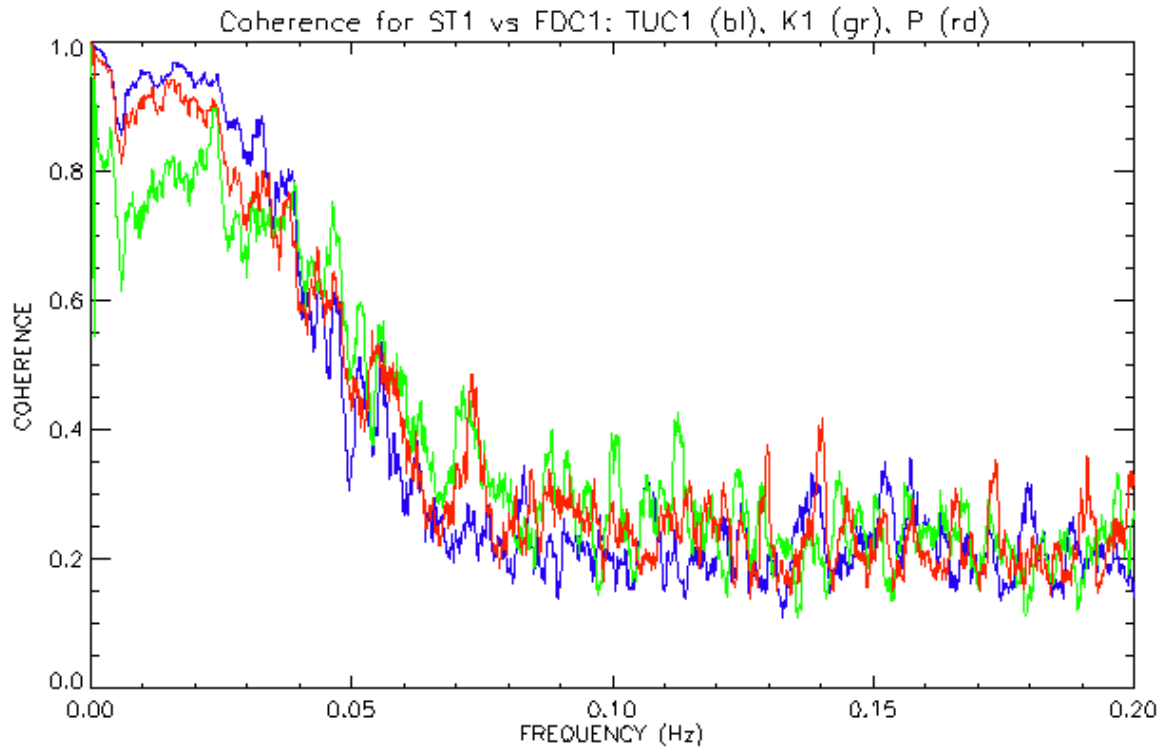


Figure 7. Coherence of TF measured at ST1 vs. TF measured at TUC1 (blue), K1 (green) and P (red) on the night of July 11-12.

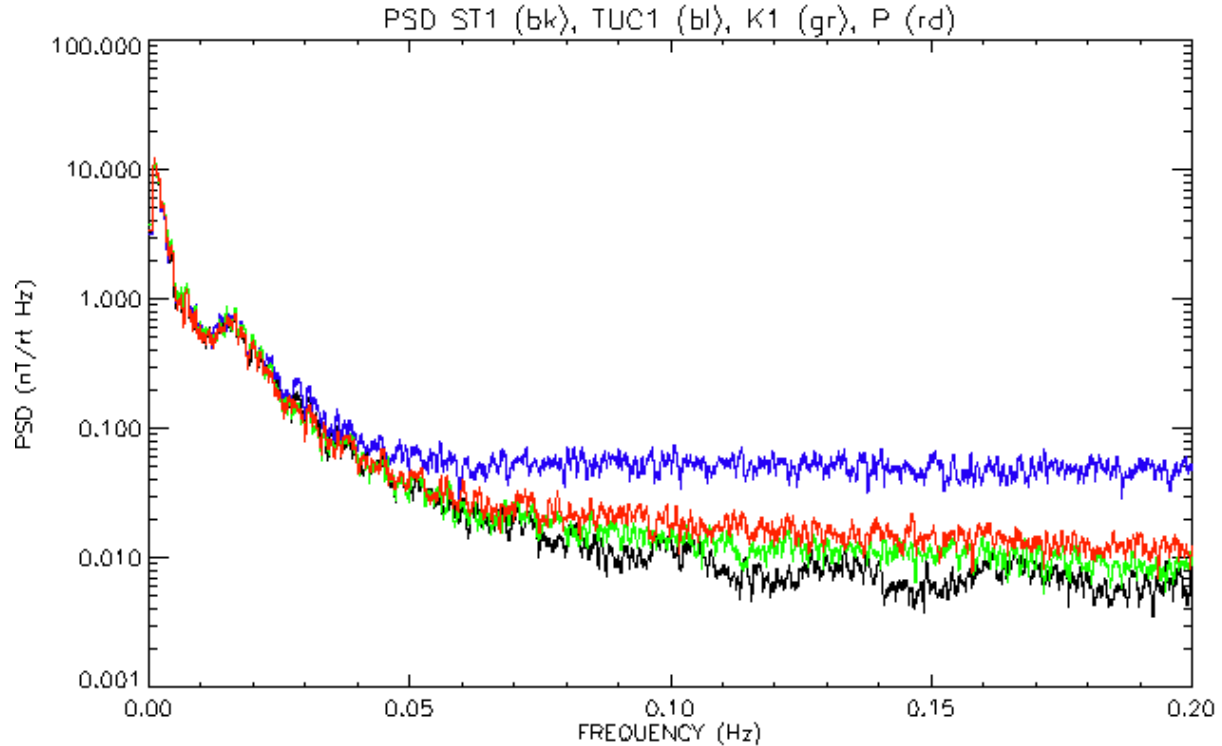


Figure 8. Power spectral density (PSD) of TF measured at ST1 (black), TUC1 (blue), K1 (green) and P (red) on the night of July 11-12.

Since only the frequencies below 0.03 Hz contain a significant amount of power, and the very lowest frequencies can contain artifacts, the average TF_a vs. TF_b coherence was calculated between the frequencies 0.005 and 0.03 Hz for all combinations of groundstation signals. The results of the TF_a vs. TF_b coherence analysis for the data collected on the night of July 11-12 are summarized in Tables 5. Table 6 summarizes the results from the data collected on the night of July 12-13.

Table 5. Coherence between the TF measurements at each groundstation for the night of July 11-12.

	Coherence 0.005 – 0.03 Hz for TF_a vs TF_b			
	ST1	TUC1	K1	P
ST1	1	0.92	0.76	0.87
TUC1	0.92	1	0.73	0.86
K1	0.76	0.73	1	0.87
P	0.87	0.86	0.87	1

Table 6. Coherence between the TF measurements at each groundstation for the night of July 12-13.

	Coherence 0.005 – 0.03 Hz for TF_a vs TF_b			
	ST2	TUC2	K2	T
ST2	1	0.92	0.82	0.91
TUC2	0.92	1	0.82	0.95
K2	0.82	0.82	1	0.91
T	0.91	0.95	0.91	1

Table 7 summarizes the results from the TF_a vs. $(X,Y,Z)_b$ coherence analysis performed on the data collected on the night of July 11-12. Table 8 summarizes the results of a similar analysis on the data collected on the night of July 12-13.

Table 7. Coherence between the TF measurement at one groundstation and the (X,Y,Z) components measured at another groundstation for the night of July 11-12.

	Coherence 0.005 – 0.03 Hz for TF_a vs $(X,Y,Z)_b$			
	ST1	TUC1	K1	P
ST1	1	-	-	-
TUC1	0.96	1	0.97	0.97
K1	0.94	0.97	1	0.96
P	0.95	0.98	0.96	1

Table 8. Coherence between the TF measurement at one groundstation and the (X,Y,Z) components measured at another groundstation for the night of July 12-13.

	Coherence 0.005 – 0.03 Hz for TF _a vs (X,Y,Z) _b			
	ST2	TUC2	K2	T
ST2	-	-	-	-
TUC2	0.94	1	0.99	0.99
K2	0.94	0.99	1	0.99
T	0.94	0.99	0.99	1

The results from Tables 5 and 7 are combined with the distances between the various groundstations in Table 3 to create a plot of coherence vs. horizontal separation for both the TF_a vs. TF_b and TF_a vs. (X,Y,Z)_b on the night of July 11-12. This is shown in Figure 9. Similarly the results from Tables 6 and 8 are combined with the distances between the various groundstations in Table 4 to create a plot of coherence vs. horizontal separation for on the night of July 12-13. This is shown in Figure 10.

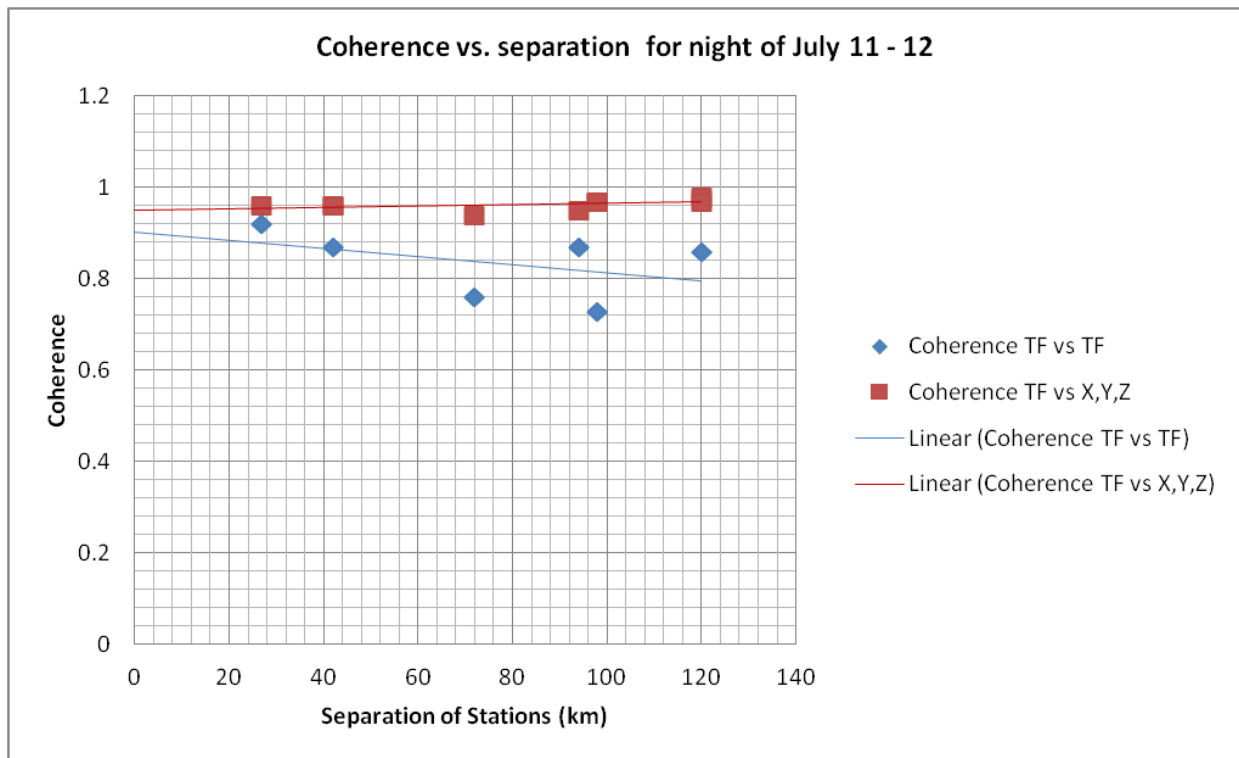


Figure 9. Coherence vs. separation for both types of coherence analysis for data collected on the night of July 11-12.

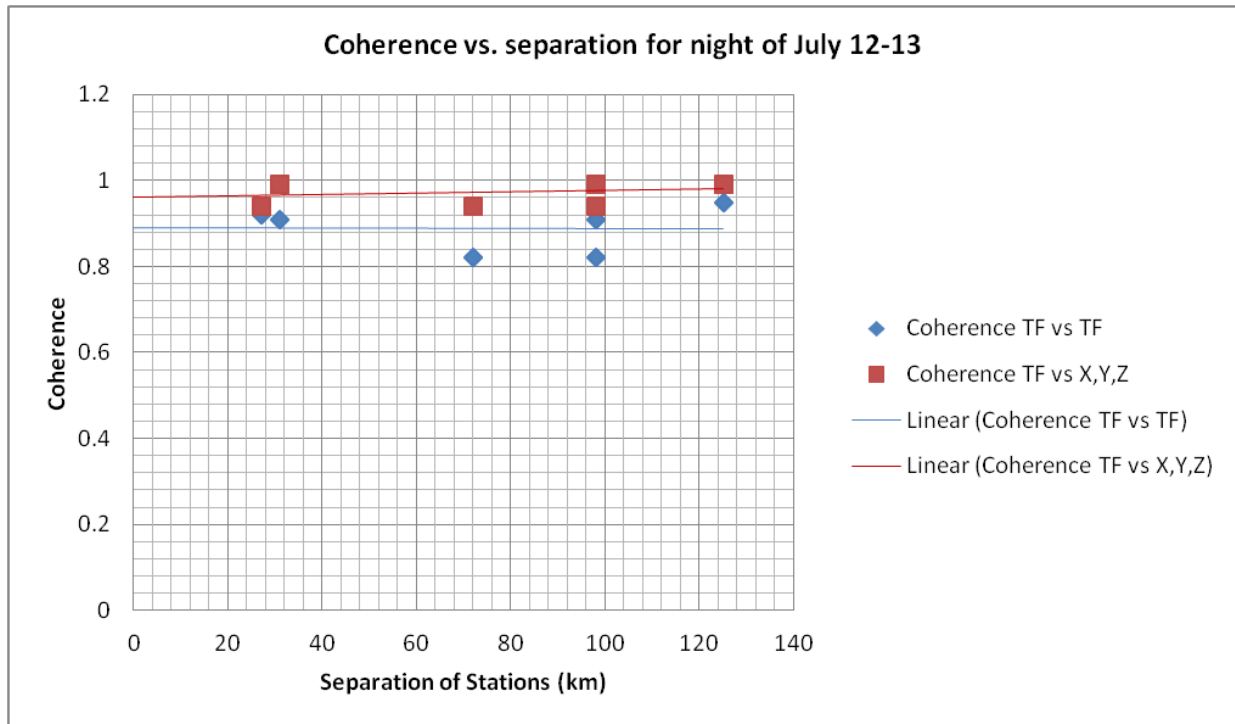


Figure 10. Coherence vs. separation for both types of coherence analysis for data collected on the night of July 12-13.

Figures 9 and 10 clearly indicate that:

- 1) the multi-parameter coherence analysis TF_a vs. $(X,Y,Z)_b$ yields a significantly higher coherence than does the single-parameter coherence analysis TF_a vs. TF_b .
- 2) while there is some loss of coherence with separations up to 130 km using the TF_a vs. TF_b method, there is virtually no loss of coherence using the multi-parameter method of TF_a vs. $(X,Y,Z)_b$.
- 3) the multi-parameter coherence method yields $C > 0.94$ out to separations of 125km.

However, it is also interesting to note that the highest coherence for the TF_a vs. TF_b method (0.95) actually occurred between TUC2 and T where the separation was 125 km. The apparent fall-off of TF_a vs. TF_b coherence may therefore be more a matter of data quality than of a true change in geomagnetic nature with distance.

2.5 Noise cancellation algorithms and results for July 11-12 and 12-13

Three time-domain noise reduction algorithms and two frequency-domain algorithms were investigated. These were:

Time-domain:

$$\text{Dif}_{ab} = \text{TF}_a - \text{TF}_b$$

$$\text{Dif2}_{ab} = \text{TF}_a - C_1 \text{TF}_b - C_2 \{\text{HILBERT TRANSFORM}(\text{TF}_b)\}$$

$$\text{Dif3}_{ab} = \text{TF}_a - C_x X_b - C_y Y_b - C_z Z_b$$

Frequency-domain (Ref 6):

Res1_{ab} = Residual from frequency-domain cancellation of TF_a vs. TF_b

Res3_{ab} = Residual from frequency-domain cancellation of TF_a vs. $(X,Y,Z)_b$.

Dif2_{ab} was found to be only slightly smaller than Dif_{ab} so the analysis was not pursued any further. Only the Dif_{ab} , Dif3_{ab} , Res1_{ab} , and Res3_{ab} analyses are reported in this document.

Tables 9-12 show the standard deviation (STD) of the raw and residuals using each of the other groundstation signals to reduce the geomagnetic noise for the night of July 11-12. The Improvement Ratio (IR) is defined as $\text{STD}(\text{TF raw})/\text{STD}(\text{residual from each type of processing})$. Tables 13-16 show the same quantities for the data collected on the night of July 12-13.

Table 9. Standard deviation and Improvement Ratio of ST1 vs. residual from 4 types of processing.

STD ST1 = 0.360

ST1 vs.	STD(dif)	STD(Dif3)	STD(Res1)	STD(Res3)	IR(dif)	IR(Dif3)	IR(Res1)	IR(Res3)
TUC1	0.060	0.048	0.041	0.039	6.0	7.5	8.8	9.2
K1	0.160	0.056	0.128	0.043	2.3	6.4	2.8	8.4
P	0.076	0.054	0.058	0.043	4.7	6.7	6.2	8.4

Table 10. Standard deviation and Improvement Ratio of K1 vs. residual from 4 types of processing.

STD K1 = 0.365

K1 vs.	STD(dif)	STD(Dif3)	STD(Res1)	STD(Res3)	IR(dif)	IR(Dif3)	IR(Res1)	IR(Res3)
TUC1	0.172	0.039	0.137	0.019	2.1	9.4	2.7	19.2
ST1	0.159	-	0.130	-	2.3	-	2.8	-
P	0.121	0.027	0.101	0.020	3.0	13.5	3.6	18.3

Table 11. Standard deviation and Improvement Ratio of P vs. residual from 4 types of processing.

STD P = 0.376

P vs.	STD(dif)	STD(Dif3)	STD(Res1)	STD(Res3)	IR(dif)	IR(Dif3)	IR(Res1)	IR(Res3)
TUC1	0.083	0.037	0.053	0.01	4.5	10.2	7.1	37.6
ST1	0.076	-	0.060	-	4.9	-	6.3	-
K1	0.121	0.031	0.103	0.021	3.1	12.1	3.7	17.9

Table 12. Standard deviation and Improvement Ratio of TUC1 vs. residual from 4 types of processing.
 $STD\ TUC1 = 0.372$

TUC1 vs.	STD(dif)	STD(Dif3)	STD(Res1)	STD(Res3)	IR(dif)	IR(Dif3)	IR(Res1)	IR(Res3)
ST1	0.060	-	0.048	-	6.2	-	7.8	-
K1	0.172	0.038	0.139	0.030	2.2	9.8	2.8	12.4
P	0.083	0.039	0.058	0.028	4.5	9.5	6.4	13.3

Table 13. Standard deviation and Improvement Ratio of ST2 vs. residual from 4 types of processing.
 $STD\ ST2 = 0.611$

ST2 vs.	STD(dif)	STD(Dif3)	STD(Res1)	STD(Res3)	IR(dif)	IR(Dif3)	IR(Res1)	IR(Res3)
TUC2	0.275	0.214	0.053	0.053	2.2	2.9	11.5	11.5
K2	0.313	0.224	0.217	0.054	2.0	2.7	2.8	11.3
T	0.247	0.202	0.083	0.055	2.5	3.0	7.4	11.1

Table 14. Standard deviation and Improvement Ratio of K2 vs. residual from 4 types of processing.
 $STD\ K2 = 0.636$

K2 vs.	STD(dif)	STD(Dif3)	STD(Res1)	STD(Res3)	IR(dif)	IR(Dif3)	IR(Res1)	IR(Res3)
TUC2	0.252	0.060	0.218	0.020	2.5	10.6	2.9	31.8
ST2	0.313	-	0.216	-	2.0	-	2.9	-
T	0.183	0.030	0.157	0.017	3.5	21.2	4.1	37.4

Table 15. Standard deviation and Improvement Ratio of T vs. residual from 4 types of processing.
 $STD\ T = 0.682$

T vs.	STD(dif)	STD(Dif3)	STD(Res1)	STD(Res3)	IR(dif)	IR(Dif3)	IR(Res1)	IR(Res3)
TUC2	0.119	0.050	0.085	0.019	5.7	13.6	8.0	35.9
ST2	0.247	-	0.091	-	2.8	-	7.5	-
K2	0.183	0.030	0.175	0.015	3.7	22.7	3.9	45.5

Table 16. Standard deviation and Improvement Ratio of TUC2 vs. residual from 4 types of processing.
 $STD\ TUC2 = 0.649$

TUC2 vs.	STD(dif)	STD(Dif3)	STD(Res1)	STD(Res3)	IR(dif)	IR(Dif3)	IR(Res1)	IR(Res3)
ST2	0.276	-	0.061	-	2.4	-	10.6	-
K2	0.252	0.050	0.232	0.031	2.6	13.0	2.8	20.9
T	0.119	0.055	0.085	0.031	5.5	11.8	7.6	20.9

The following conclusions can be drawn from Tables 9-16:

- 1) the frequency-domain cancellation methods result in smaller residuals/higher Improvement Ratios than do the time-domain methods,
- 2) both the time and frequency-domain methods that use all three component signals (TF_a vs. $(X,Y,Z)_b$) yield smaller residuals/higher Improvement Ratios than do the methods that only use the total-field signals (TF_a vs. TF_b),
- 3) the average Improvement Ratio for the FDC method of (TF_a vs. TF_b) = $IR(Res1) = 5.2$,
- 4) the average Improvement Ratio for the FDC methods of (TF_a vs. $(X,Y,Z)_b$) = $IR(Res3) = 20.6$.

The Improvement Ratio data from Tables 9-12 have been combined with the separation data from Table 3 to yield a plot of IR vs. separation for the data collected on the night of July 11-12. This is shown in Figure 11. Figure 12 shows the same quantities for the data collected on the night of July 12-13.

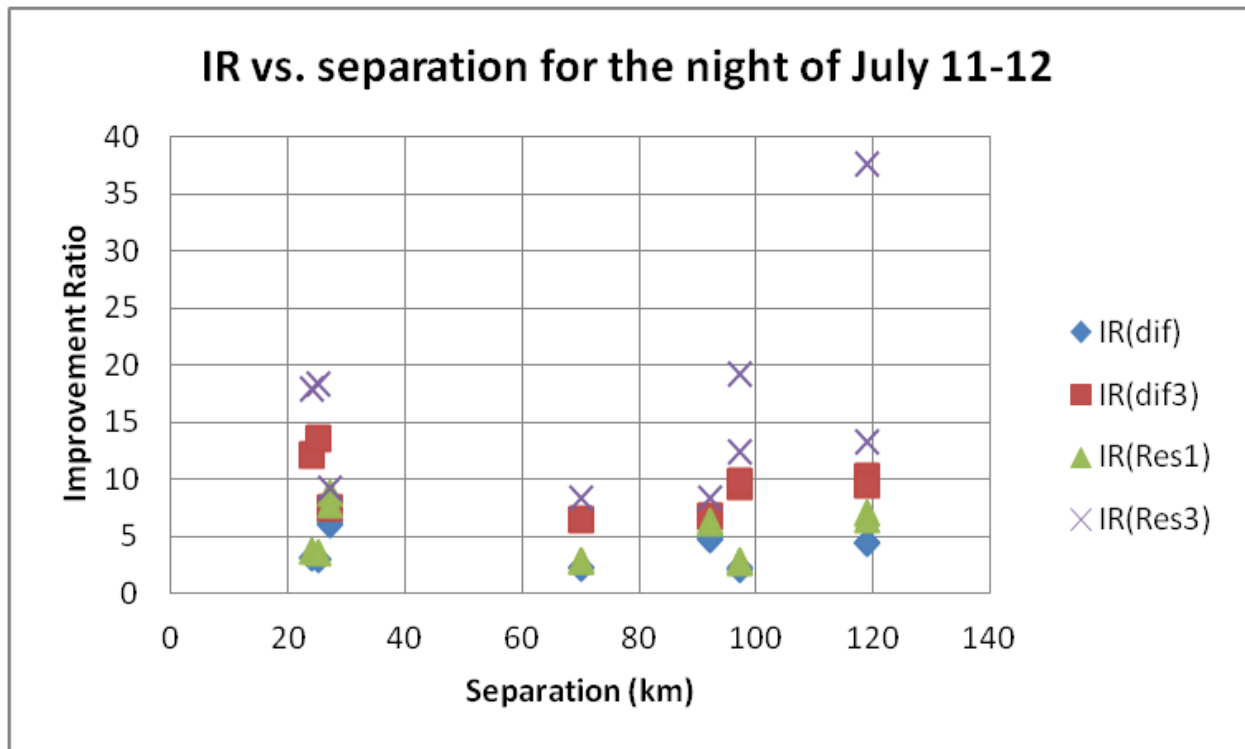


Figure 11. Improvement Ratio vs. separation for all types of noise-reduction processing applied to the data collected on the night of July 11-12.

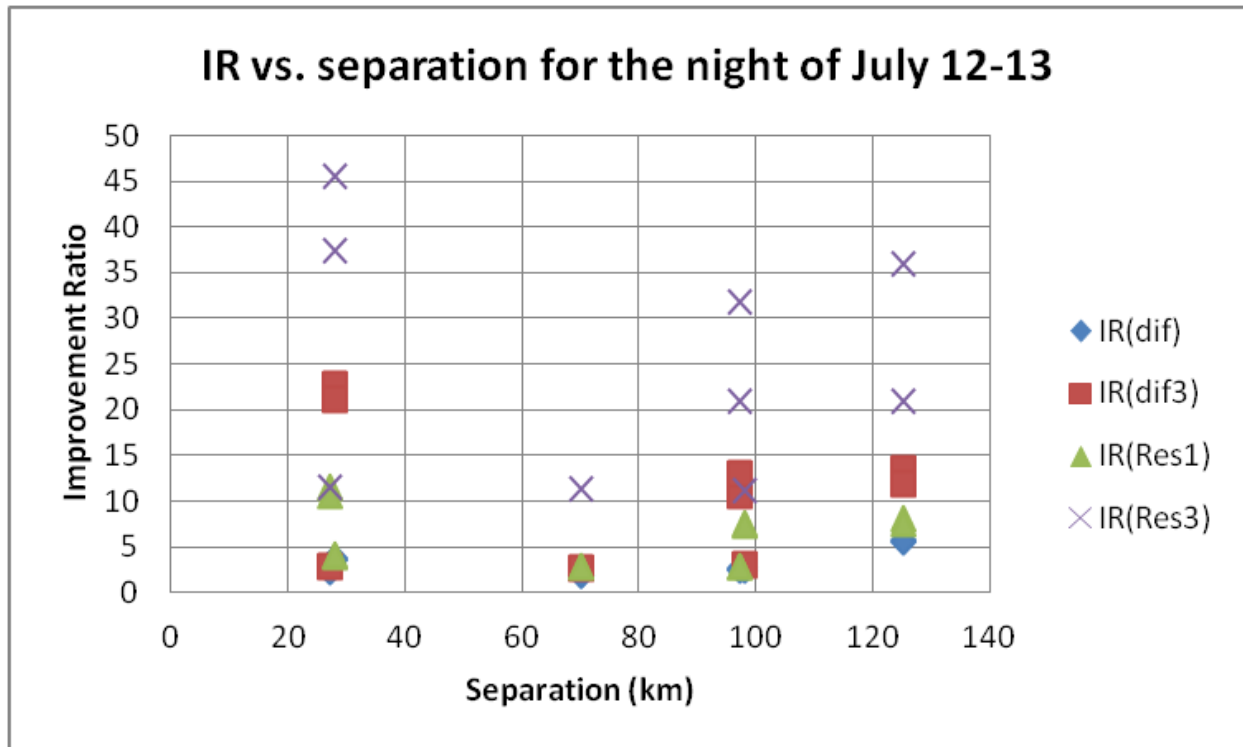


Figure 12. Improvement Ratio vs. separation for all types of noise-reduction processing applied to the data collected on the night of July 12-13.

There is no discernible pattern of Improvement Ratio vs. separation, which suggests that the actual noise reduction achieved may be more of a function of the quality of the data recorded at each groundstation.

3. Groundstation magnetic measurements October 2015

Similar pre-processing of the groundstation data from the night of Oct 8-9 was done to verify that the data were valid and free from man-made artifacts prior to conducting the same groundstation-to-groundstation analysis. Sections 3.1-3.3 contain all the information on the groundstation positions, coherence between groundstations using both TF_a vs. TF_b and TF_a vs. $(X,Y,Z)_b$ analyses, and the results from the same noise reduction analysis as applied to the Oct 8-9 data.

3.1 Locations of the groundstations

The same USGS groundstation at Tucson (TUC1) was used, and the same Geometrics G823 Cesium total-field magnetometer was set up at the Stewart Observatory (ST1), but the USGS basestation was set up at the Florence Military Reserve (FMR) instead of either the Tinto Forest or Peridot location as was used in July 2015. The Florence Military Reserve is a secure site that did not require anyone to stay with the groundstation equipment overnight. Figure 13 shows the positions of the three groundstations and the laser illumination spot during the Oct 8-9 test. Table 17-19 gives the locations of the three groundstation and the laser illumination spot and their separations.



Figure 13. Locations of the three groundstations and the spot directly beneath where the FASORtronics laser illuminated the mesosphere on the night of Oct 8-9.

Table 17. Coordinates for the three groundstation locations and the FASORtronics laser excitation point for the Oct 8-9 trial.

Location	Denoted	Latitude (°)	Longitude (°)
Laser excitation point	L	33.1270	110.3360
Florence Military Reserve	FMR	33.0833	111.3551
Stewart Observatory	ST1	32.4169	110.7326
Tucson USGS Observatory	TUC1	32.1745	110.7337

Table 18. Horizontal separation of the three groundstation locations and the FASORtronics laser excitation point for the Oct 8-9 trial.

Location	Laser excitation point	Florence Military Reserve	Stewart Observatory	Tucson USGS Observatory
Laser excitation point	0	95	87	112
Florence Military Reserve	95	0	94	116
Stewart Observatory	87	94	0	27
Tucson USGS Observatory	112	116	27	0

Table 19 is a subset of the data in Table 18, showing the separation of the groundstations for the night of Oct 8-9.

Table 19. Separation of various groundstations for the night of Oct 8-9.

Location	Distance (km)		
	TUC1	ST1	FMR
TUC1	0	27	116
ST1	27	0	94
FMR	116	94	0

3.2 Coherence analysis for the Oct 8-9 data

The results of the TF_a vs. TF_b coherence analysis for the data collected on the night of Oct 8-9 are summarized in Table 20. Table 21 summarizes the results from the TF_a vs. $(X,Y,Z)_b$ coherence analysis performed on the data collected on the night of Oct 8-9.

Table 20. Coherence between the TF measurements at each groundstation for the night of Oct 8-9.

	Coherence 0.005 – 0.03 Hz for TF_a vs TF_b		
	TUC1	ST1	FMR
TUC1	1	0.856	0.946
ST1	0.856	1	0.866
FMR	0.946	0.866	1

Table 21. Coherence between the TF measurement at one groundstation and the (X,Y,Z) components measured at another groundstation for the night of Oct 8-9.

	Coherence 0.005 – 0.03 Hz for TF _a vs. (X,Y,Z) _b		
	TUC1	ST1	FMR
TUC1	1	-	0.963
ST1	0.844	1	0.89
FMR	0.959	-	1

The results from Tables 20 and 21 were combined with the distances between the various groundstations in Tables 19 to create a plot of coherence vs. horizontal separation for both the TF_a vs. TF_b and TF_a vs. (X,Y,Z)_b coherence analysis. This is shown in Figure 14.

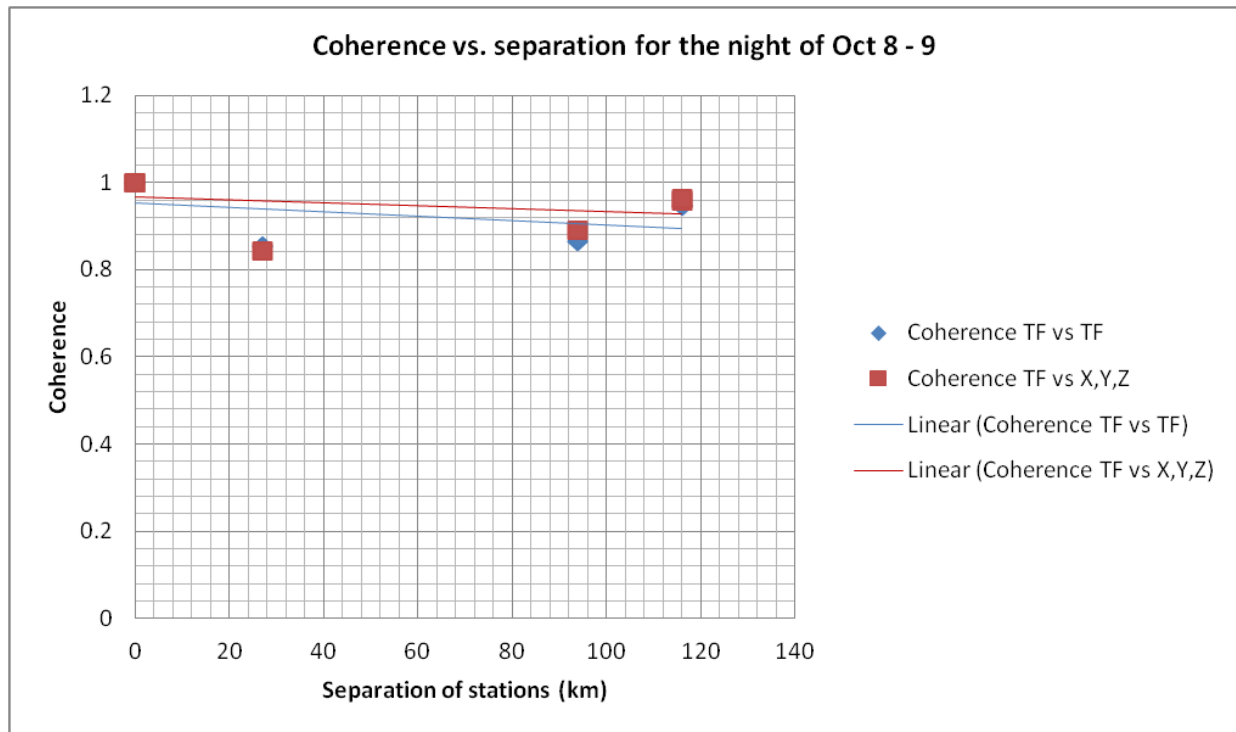


Figure 14. Coherence vs. separation for both types of coherence analysis for data collected on the night of Oct 8-9.

3.3 Noise cancellation results for Oct 8-9 data

Tables 22-24 show the standard deviation (STD) of the raw and residuals using each of the other groundstation signals to reduce the geomagnetic noise for the night of Oct 8-9. The Improvement Ratio (IR) is again defined as $\text{STD}(\text{TF raw})/\text{STD}(\text{residual from each type of processing})$.

Table 22. Standard deviation and Improvement Ratio of TUC1 vs. residual from 4 types of processing.
 $STD\ TUC1 = 0.361$

TUC1 vs.	STD(dif)	STD(dif3)	STD(Res1)	STD(Res3)	IR(dif)	IR(Dif3)	IR(Res1)	IR(Res3)
FMR	0.05	0.029	0.03	0.018	7.2	12.4	12.0	20.1
ST1	0.077	-	0.049	-	4.7	-	7.4	-

Table 23. Standard deviation and Improvement Ratio of ST1 vs. residual from 4 types of processing.
 $STD\ ST1 = 0.366$

ST1 vs.	STD(dif)	STD(dif3)	STD(Res1)	STD(Res3)	IR(dif)	IR(Dif3)	IR(Res1)	IR(Res3)
FMR	0.09	0.064	0.046	0.045	3.7	5.3	7.3	7.5
TUC1	0.077	0.06	0.047	0.039	4.4	5.6	7.1	8.6

Table 24. Standard deviation and Improvement Ratio of FMR vs. residual from 4 types of processing.
 $STD\ FMR = 0.391$

FMR vs.	STD(dif)	STD(dif3)	STD(Res1)	STD(Res3)	IR(dif)	IR(Dif3)	IR(Res1)	IR(Res3)
TUC1	0.05	0.03	0.033	0.02	7.8	13.0	11.8	19.6
ST1	0.09	-	0.052	-	4.3	-	7.5	-

The following conclusions can be drawn from Tables 22-24:

- 1) the frequency-domain cancellation methods result in smaller residuals/higher Improvement Ratios than do the time-domain methods,
- 2) both the time and frequency-domain methods that use all three component signals (TF_a vs. $(X,Y,Z)_b$) yield smaller residuals/higher Improvement Ratios than do the methods that only use the total-field signals (TF_a vs. TF_b),
- 3) the noise reduction obtained when the Stewart Observatory data are used as either the dependent or the independent variable in the analysis is significantly worse than when just the TUC1 and FMR data are used. This suggests that the ST1 data have additional noise in them that was not removed completely with the pre-processing,
- 4) if we eliminate the ST1 results, then the average Improvement Ratio for the FDC method of $(TF_a$ vs. $TF_b) = IR(Res1) = 11.9$,
- 5) if we eliminate the ST1 results, then the average Improvement Ratio for the FDC method of $(TF_a$ vs. $(X,Y,Z)_b) = IR(Res3) = 19.9$.

The Improvement Ratio data from Tables 22-24 have been combined with the separation data from Table 19 to yield a plot of IR vs. separation for the data collected on the night of Oct 8-9. This is shown in Figure 15.

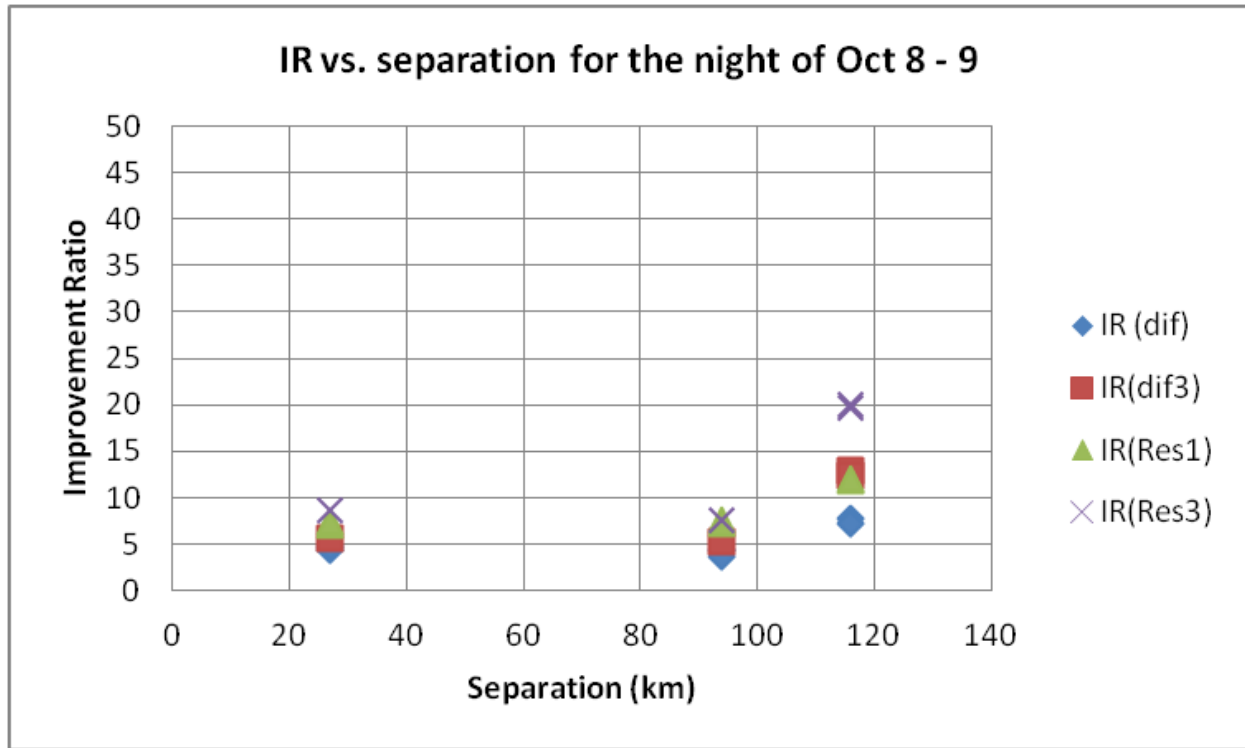


Figure 15. Improvement Ratio vs. separation for all types of noise-reduction processing applied to the data collected on the night of Oct 8-9.

The best Improvement Ratio is actually found at the maximum separation, which suggests that the actual noise reduction achieved is more of a function of the quality of the data recorded at each groundstation than it is of separation.

4. Conclusions

The following conclusions were drawn from the analysis of the 0.005-0.30 Hz band-pass filtered groundstation magnetic data collected at various locations on the nights of July 11-12, July 12-13, and October 8-9, 2015:

- 1) the frequency-domain cancellation methods result in smaller residuals/higher Improvement Ratios than do the time-domain methods,
- 2) both the time and frequency-domain methods that use all three component signals (TF_a vs. $(X,Y,Z)_b$) yield smaller residuals/higher Improvement Ratios than do the methods that only use the total-field signals (TF_a vs. TF_b),

- 3) there is no discernible pattern of Improvement Ratio vs. separation, which suggests that the actual noise reduction achieved may be more of a function of the quality of the data recorded at each groundstation,

The three data sets collected at the Stewart Observatory in the Oct 8-9 data set consistently yield poorer noise reduction and coherence vs. the other groundstations. They have not been included in the remaining conclusions because it was felt that the data quality from that location was affecting the results.

- 4) there were 14 measurements of the standard deviation of FDC processed residual for $(TF_a \text{ vs. } (X,Y,Z)_b) = \text{STD}(\text{Res3})$ contained in Tables 10,11,12,14,15,16, 22, and 24. The values ranged from 0.010 to 0.031 nT, with a mean value of 0.019 nT,
- 5) the standard deviations of those residuals show very little range dependence,
- 6) the standard deviation of the raw TF on the three nights ranged from 0.36-0.65 nT, but the standard deviation of the FDC residual for $(TF_a \text{ vs. } (X,Y,Z)_b)$ processing was not dependent on the amplitude of the geomagnetic activity,
- 7) the average Improvement Ratio for all data using the FDC processing of $(TF_a \text{ vs. } TF_b) = \text{IR}(\text{Res1})$ was 5.7 whereas the average for all data using the FDC processing of $(TF_a \text{ vs. } (X,Y,Z)_b) = \text{IR}(\text{Res3})$ was 20.5.

Taken together these lead to the following very simple conclusions:

- 7) when the data quality is very good, using FDC processing of $(TF_a \text{ vs. } (X,Y,Z)_b)$ will yield a residual with a standard deviation of ~ 0.02 nT when the separation of the groundstations is 125 km or less, regardless of whether the geomagnetic field is quiet ($\text{STD} = 0.36$ nT) or active ($\text{STD} = 0.65$ nT),
- 8) assuming the vertical coherence of the Earth's magnetic field is similar to the horizontal coherence, and since 125 km horizontal separation is greater than the vertical separation of the Sodium ion layer and the ground (100 km), this suggests that good coherence may exist between (X,Y,Z) geomagnetic signals measured on ground stations and TF measurements made in the mesosphere,

However, the objective of this work was to estimate the geomagnetic noise reduction that might be possible using mesospheric TF measurements to cancel TF variations in the geomagnetic field made near the Earth's surface. Looking at the Improvement Ratios for Dif_{ab} and $(TF_a \text{ vs. } TF_b)$ processing contained in Tables 9-16 and 22-24 leads to the following conclusion:

- 9) assuming the vertical coherence of the Earth's magnetic field is similar to the horizontal coherence, then using TF measurements made in the mesosphere to cancel geomagnetic noise in the total-field measurements near ground may give a cancellation factor of ~ 5.7 if the FDC method of processing $(TF_a \text{ vs. } TF_b)$ is used. While this is not a tremendous amount of noise reduction, it would still improve MAD detection ranges by approximately 80% assuming a $1/R^3$ fall off of signal with distance for the magnetic anomaly due to a submarine.

References

1. J. Bradley Nelson, *Geological and Geomagnetic Noise Reduction Along the Atlantic Continental Margin*, DRDC Atlantic Tech Memo 2007-002, October 2007
2. J. M. Highbie, S. M. Rochester, B. Patton, R. Holzlohner, D. Bonaccini Calia, and D. Budker, *Magnetometry with Mesospheric Sodium*, Proceedings of the National Academy of Sciences of the United States of America (PNAS), **V 108 No. 9**, p 3522–3525, 2011. doi: 10.1073/pnas.1013641108
3. <http://www.swpc.noaa.gov/products/27-day-outlook-107-cm-radio-flux-and-geomagnetic-indices>
4. <http://geomag.usgs.gov/monitoring/instrumentation.php>
5. <http://magweb.cr.usgs.gov/data/magnetometer/TUC/OneSecond/>
6. J.S. Bendat and A.G. Piersol, *Engineering Applications of Correlation and Spectral Analysis*, 1st ed. New York, NY: John Wiley and Sons, 1980

Appendix A: Time and frequency-domain plots of all groundstation vs. groundstation noise cancellation and coherence analysis

A.1 Night of Jul 11-12

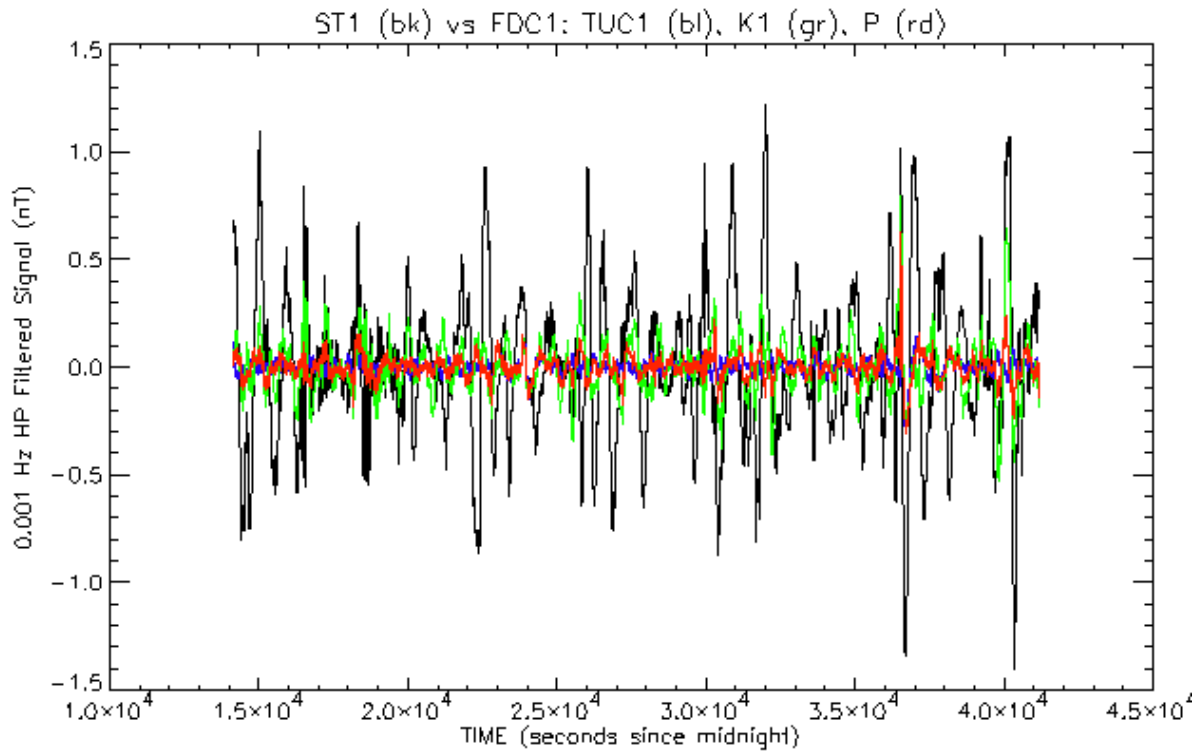


Figure A.1 TF from ST1 (black) vs. Res1 for TUC1 (blue), K1 (green), and P (red) on the night of July 11-12.

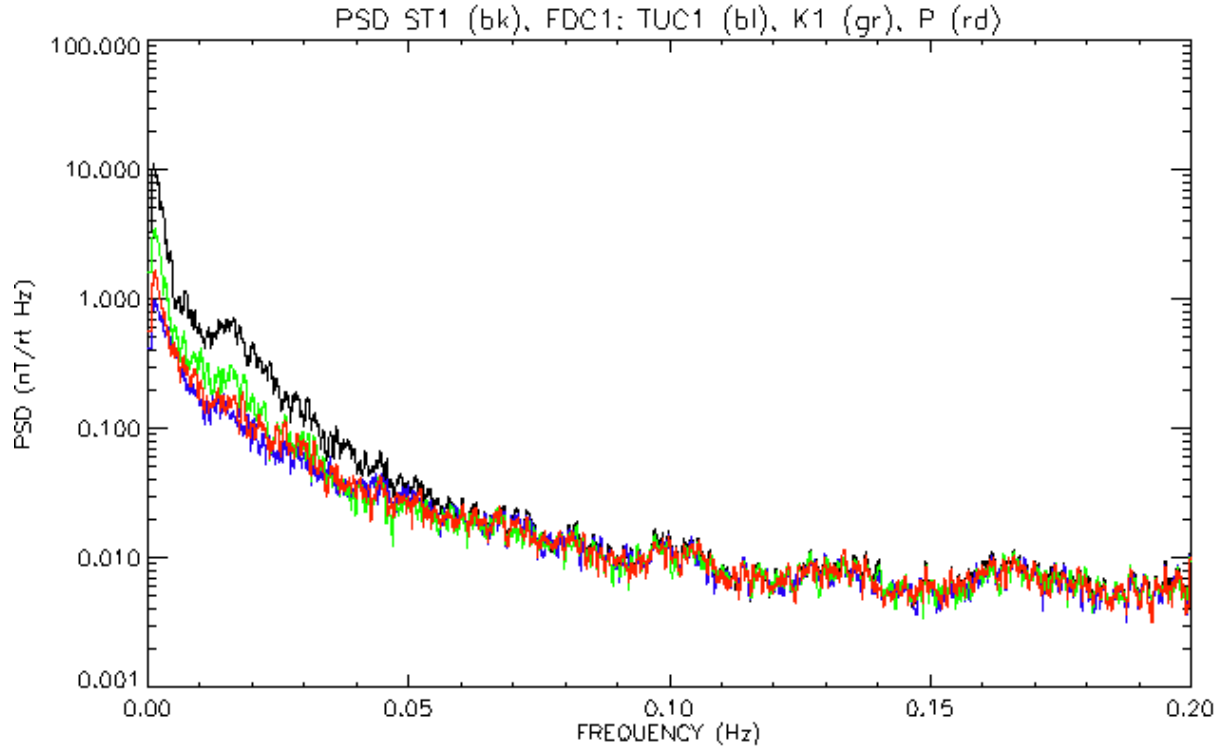


Figure A.2 PSD of TF at ST1 (black) vs. Res1 for TUC1 (blue), K1 (green), and P (red) for the night of July 11-12.

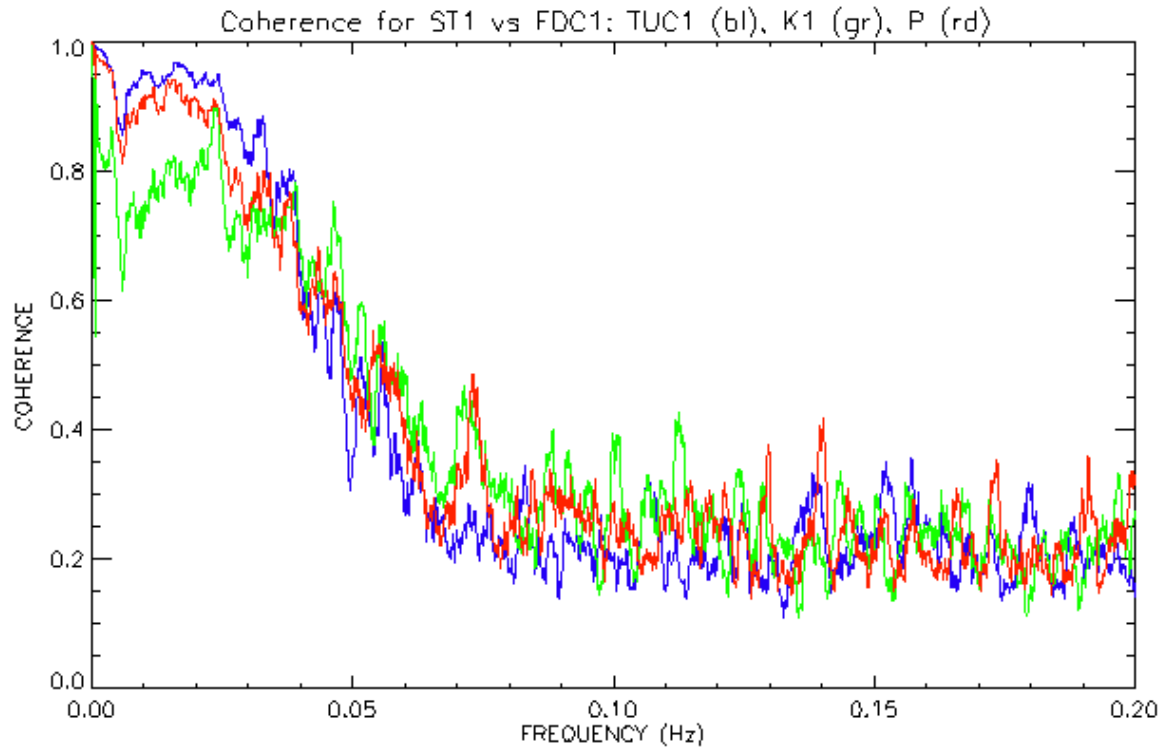


Figure A.3 Coherence of TF at ST1 vs. TF at TUC1 (blue), K1 (green), and P (red) for the night of July 11-12.

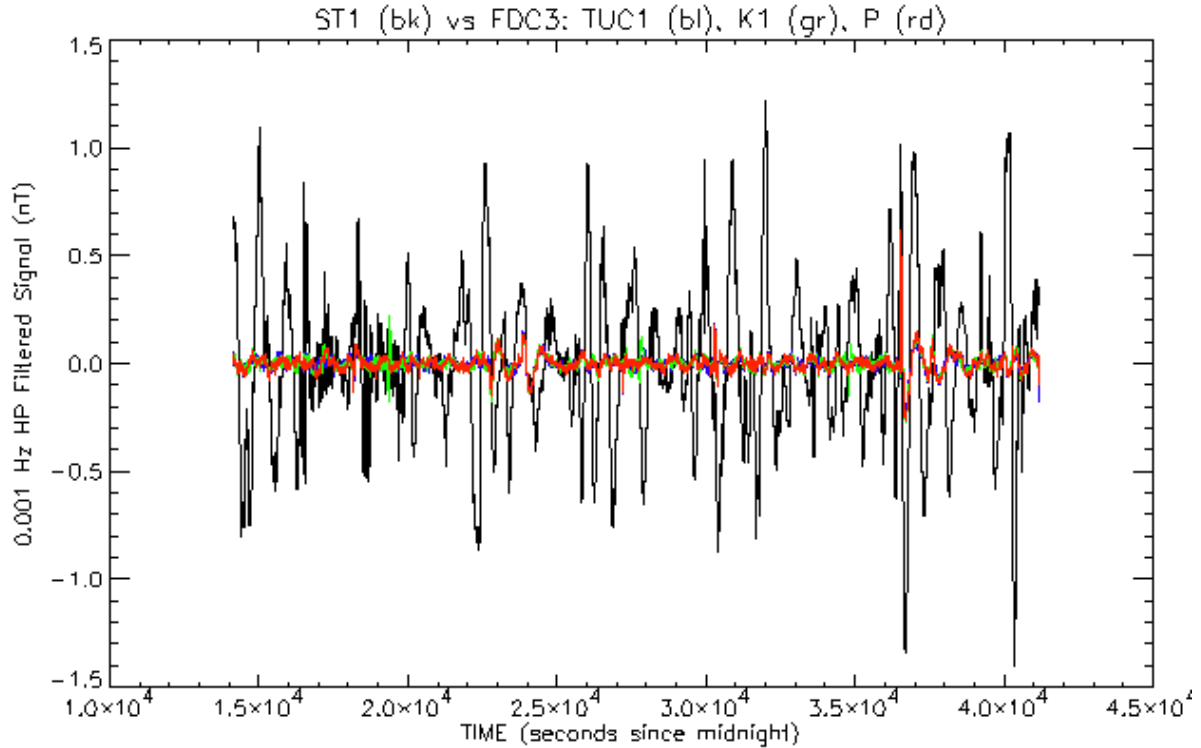


Figure A.4 TF from ST1 (black) vs. Res3 from TUC1 (blue), K1 (green), and P (red) on the night of July 11-12.

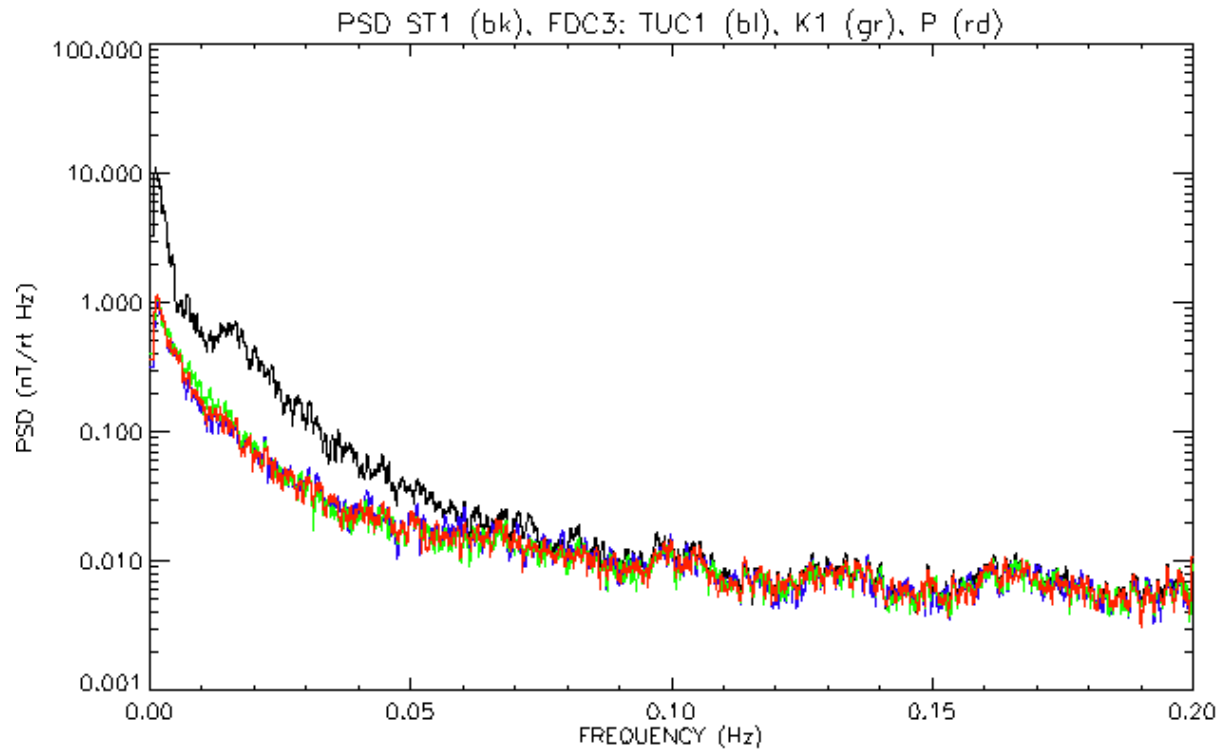


Figure A.5 PSD of TF at ST1 vs. Res3 for TUC1 (blue), K1 (green), and P (red) for the night of July 11-12.

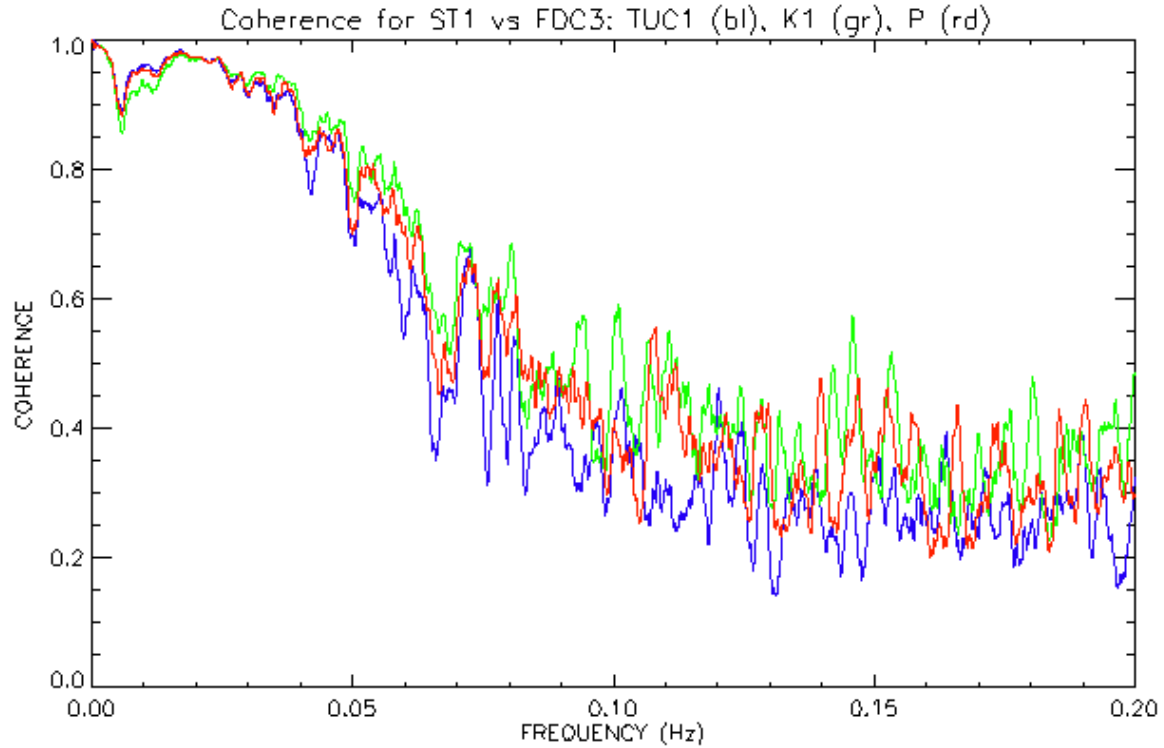


Figure A.6 Coherence of TF at ST1 vs. (X,Y,Z) at TUC1 (blue), K1 (green), and P (red) for the night of July 11-12.

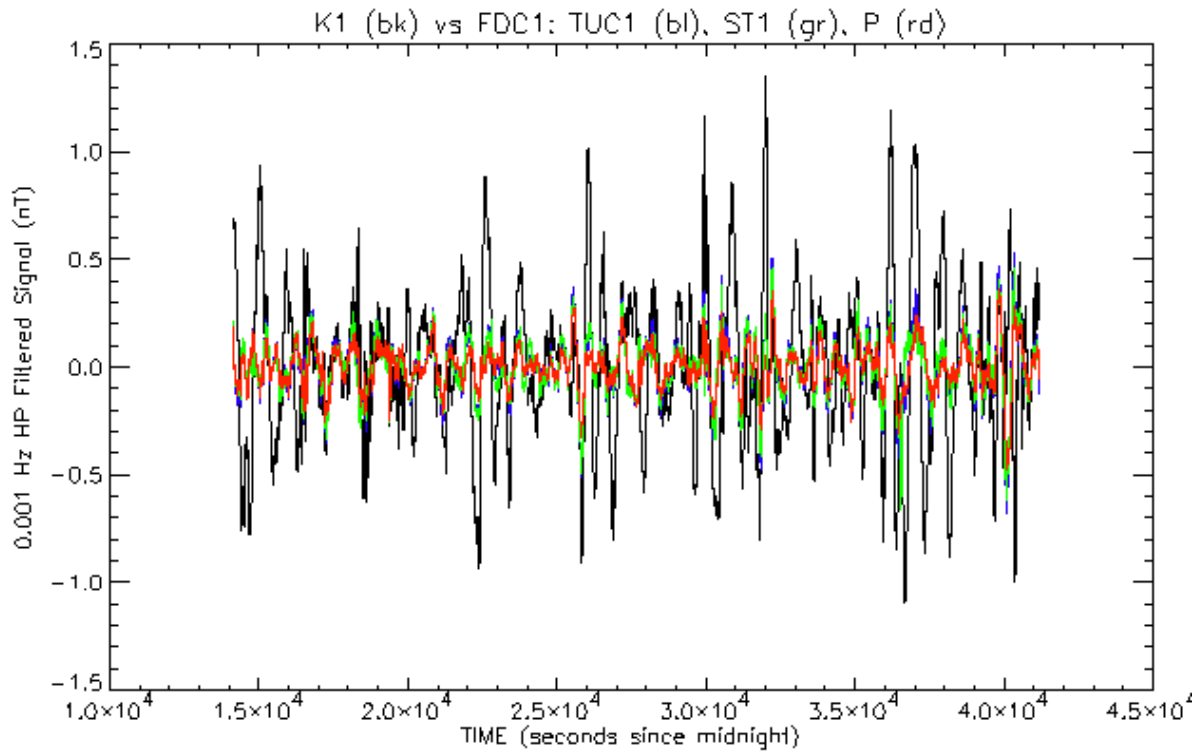


Figure A.7 TF from K1 (black) vs. Res1 for TUC1 (blue), ST1 (green), and P (red) on the night of July 11-12.

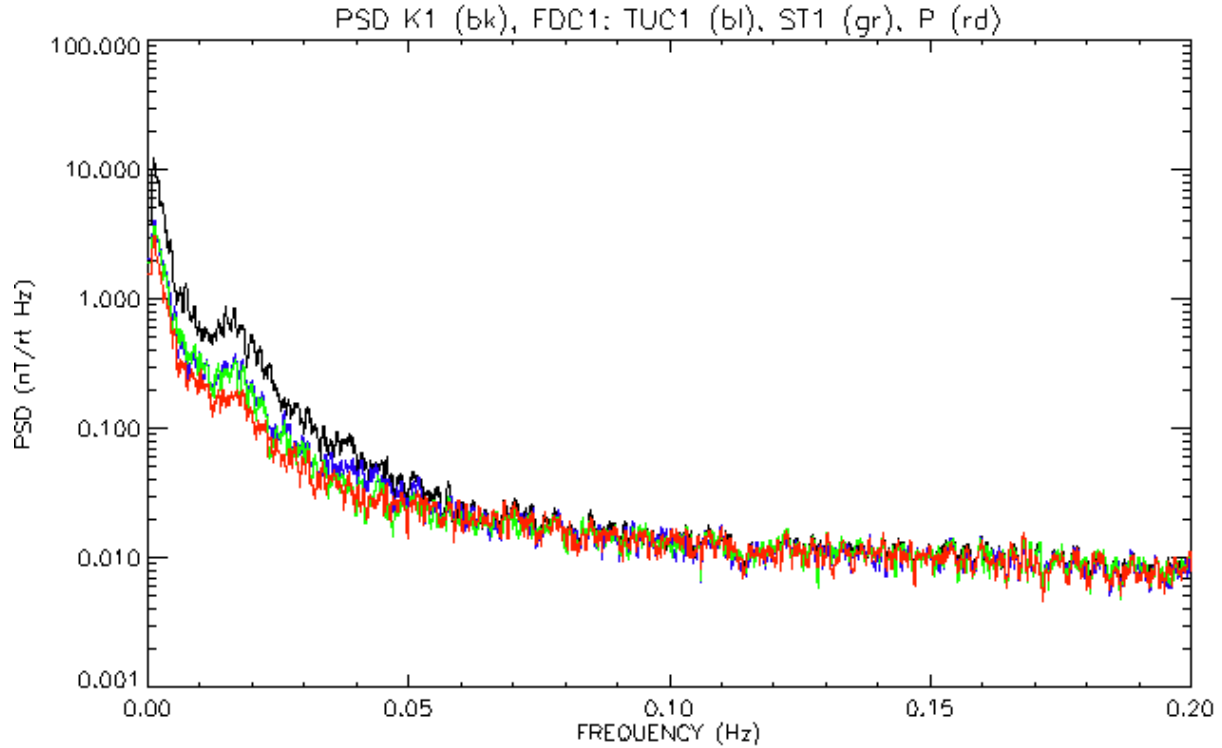


Figure A.8 PSD of TF at K1 (black) vs. Res1 for TUC1 (blue), ST1 (green), and P (red) for the night of July 11-12.

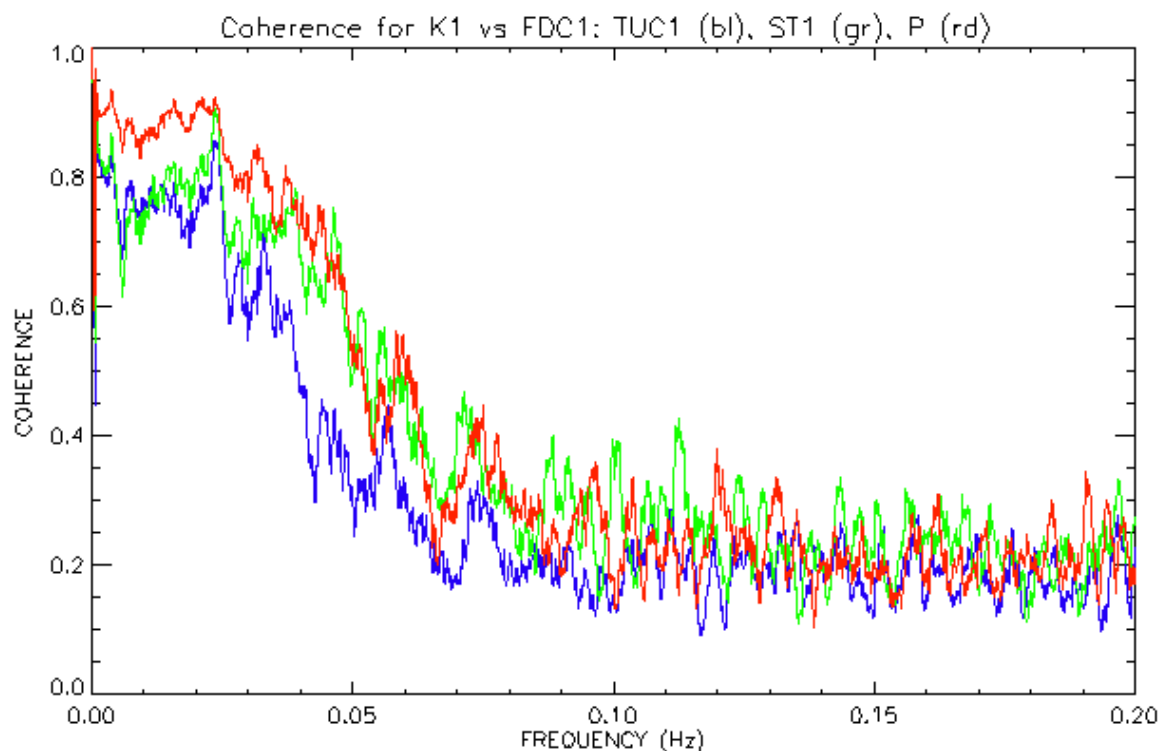


Figure A.9 Coherence of TF at K1 vs. TF at TUC1 (blue), ST1 (green), and P (red) for the night of July 11-12.

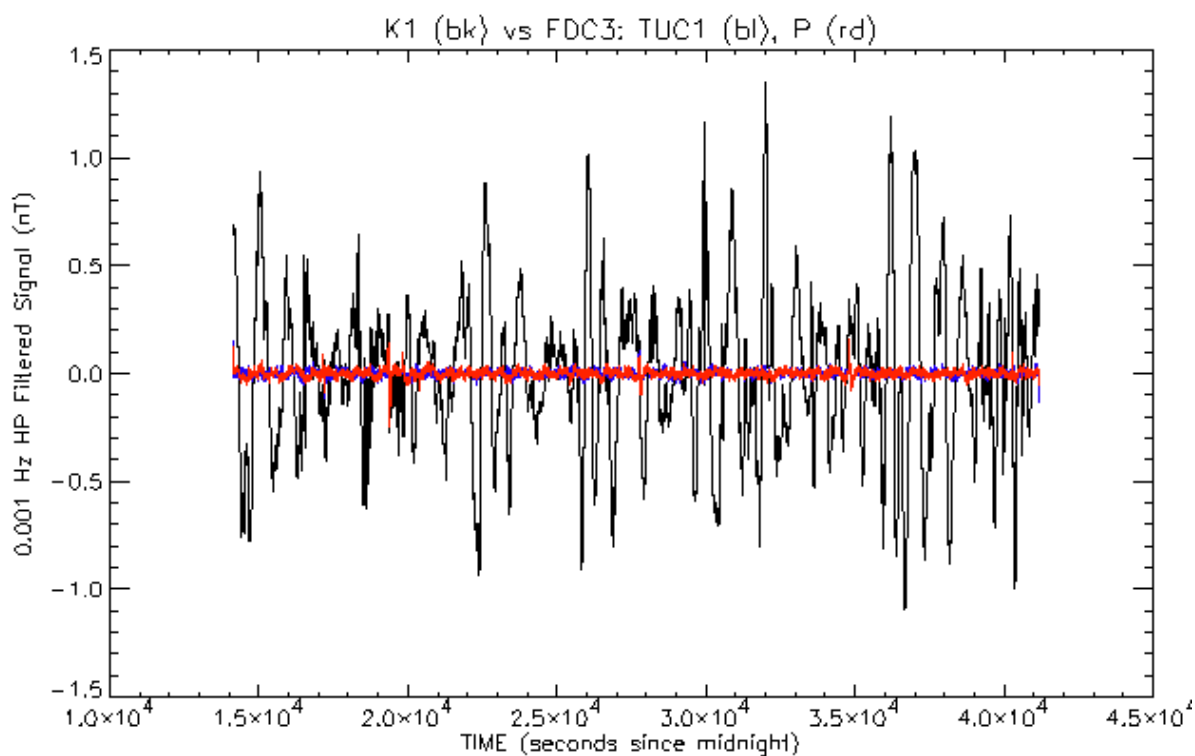


Figure A.10 TF from K1 (black) vs. Res3 from TUC1 (blue), and P (red) on the night of July 11-12.

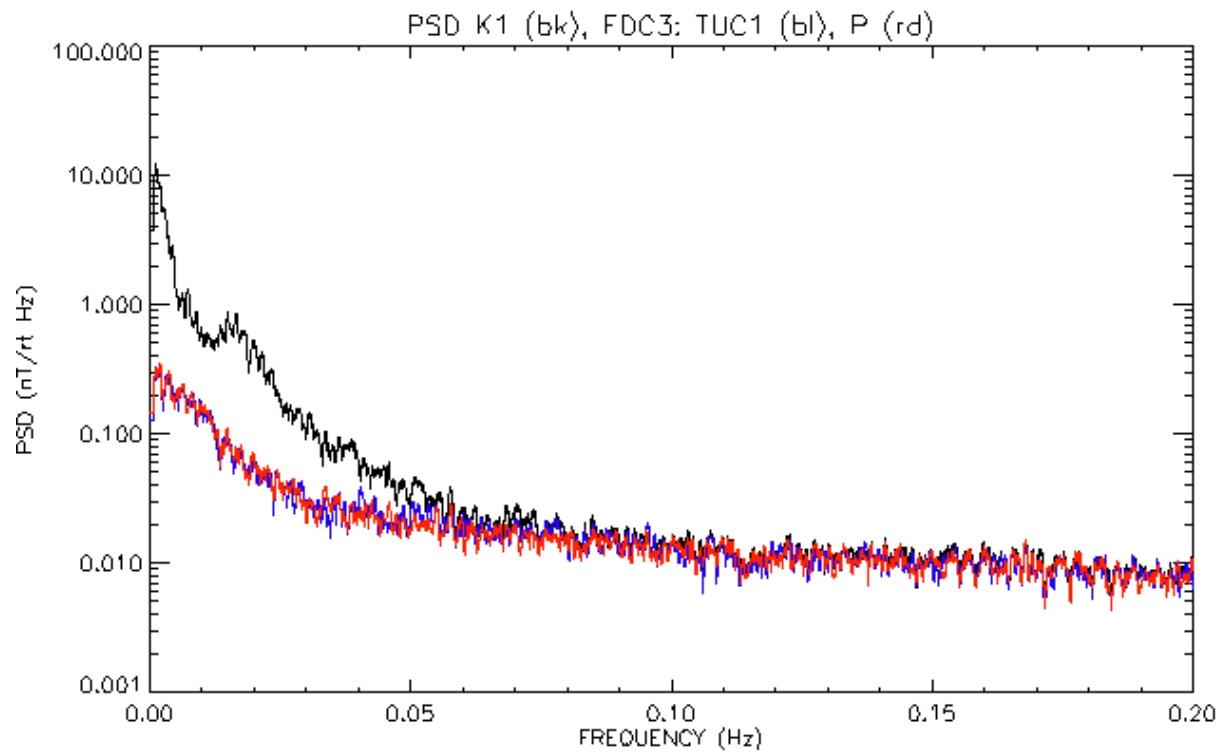


Figure A.11 PSD of TF at K1 vs. Res3 for TUC1 (blue), and P (red) for the night of July 11-12.

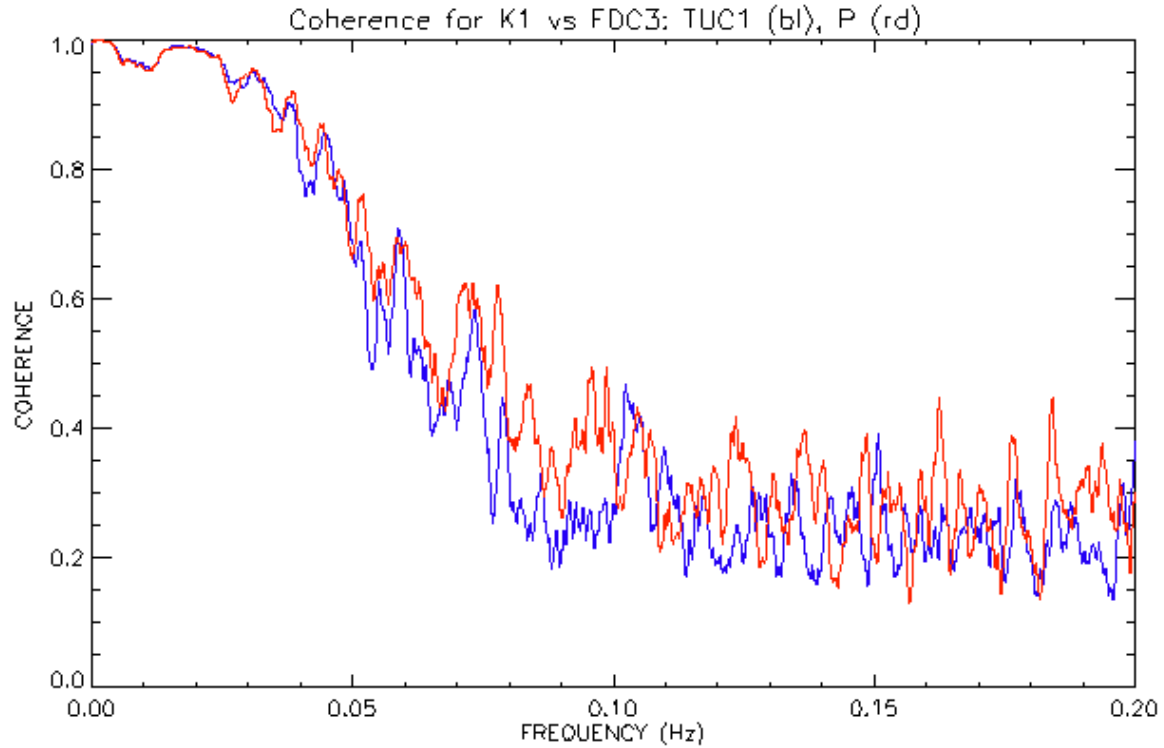


Figure A.12 Coherence of TF at K1 vs. (X,Y,Z) at TUC1 (blue), and P (red) for the night of July 11-12.

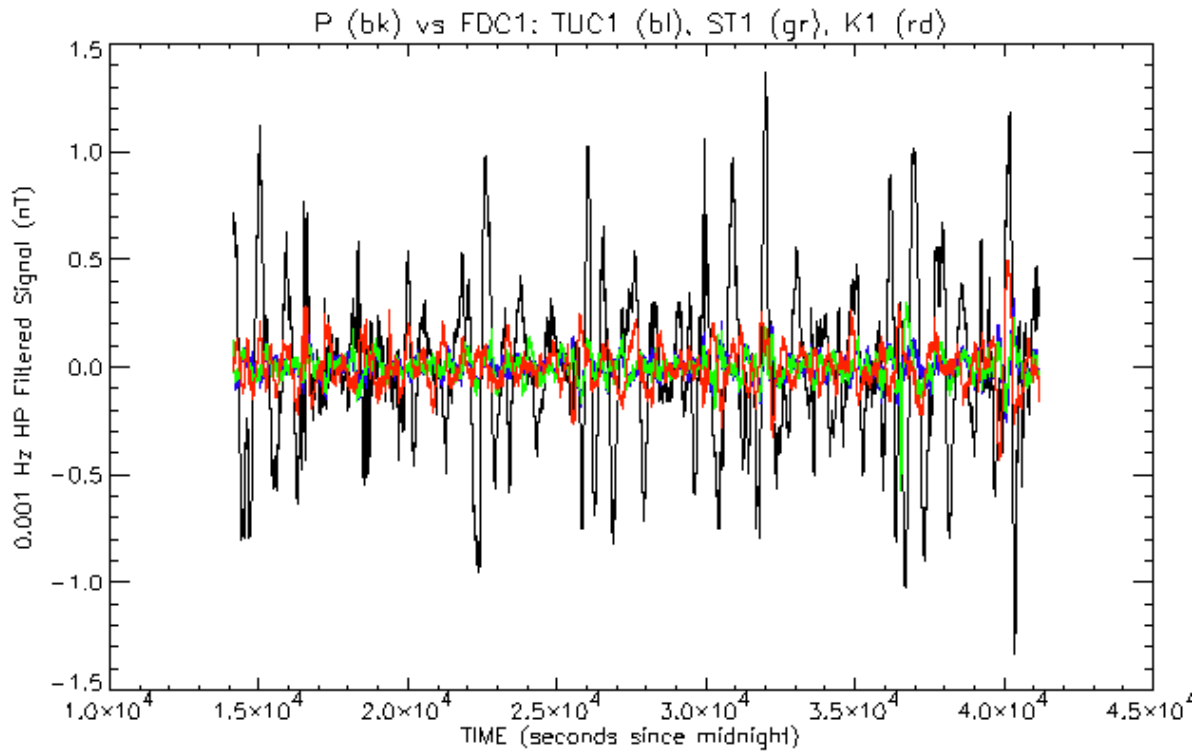


Figure A.13 TF from P (black) vs. Res1 for TUC1 (blue), ST1 (green), and K1 (red) on the night of July 11-12.

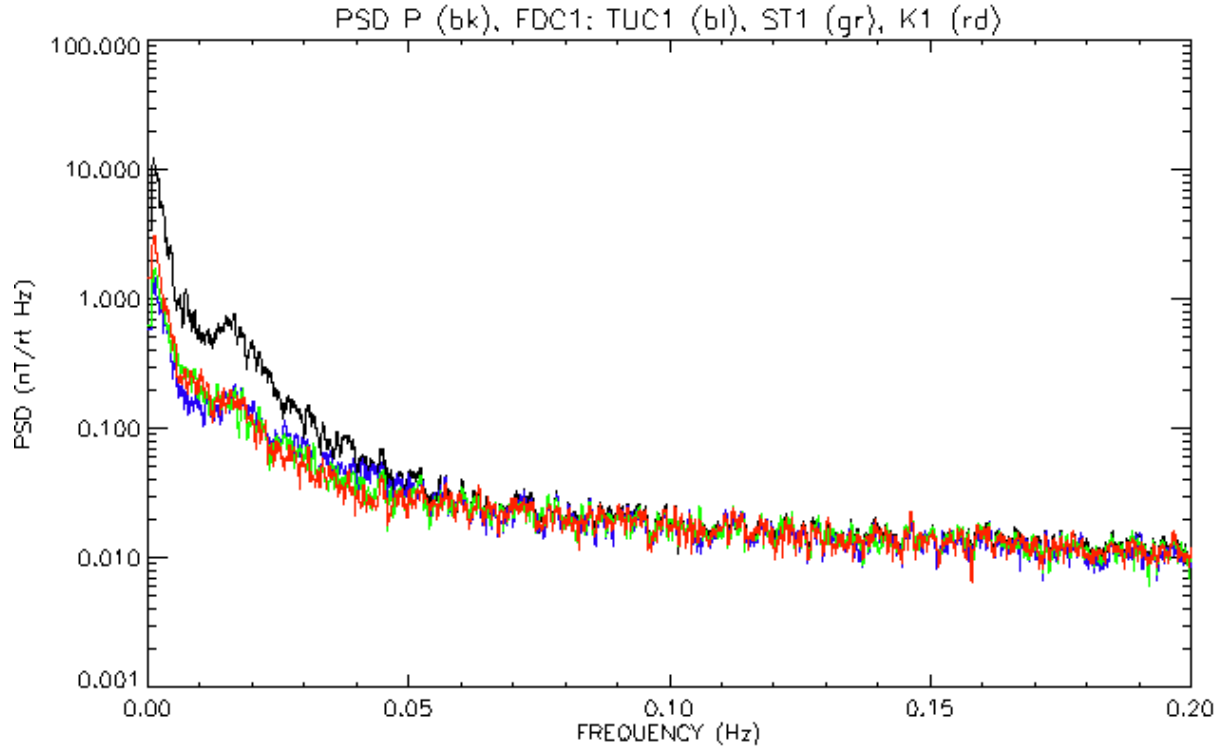


Figure A.14 PSD of TF at P (black) vs. Res1 for TUC1 (blue), ST1 (green), and K1 (red) for the night of July 11-12.

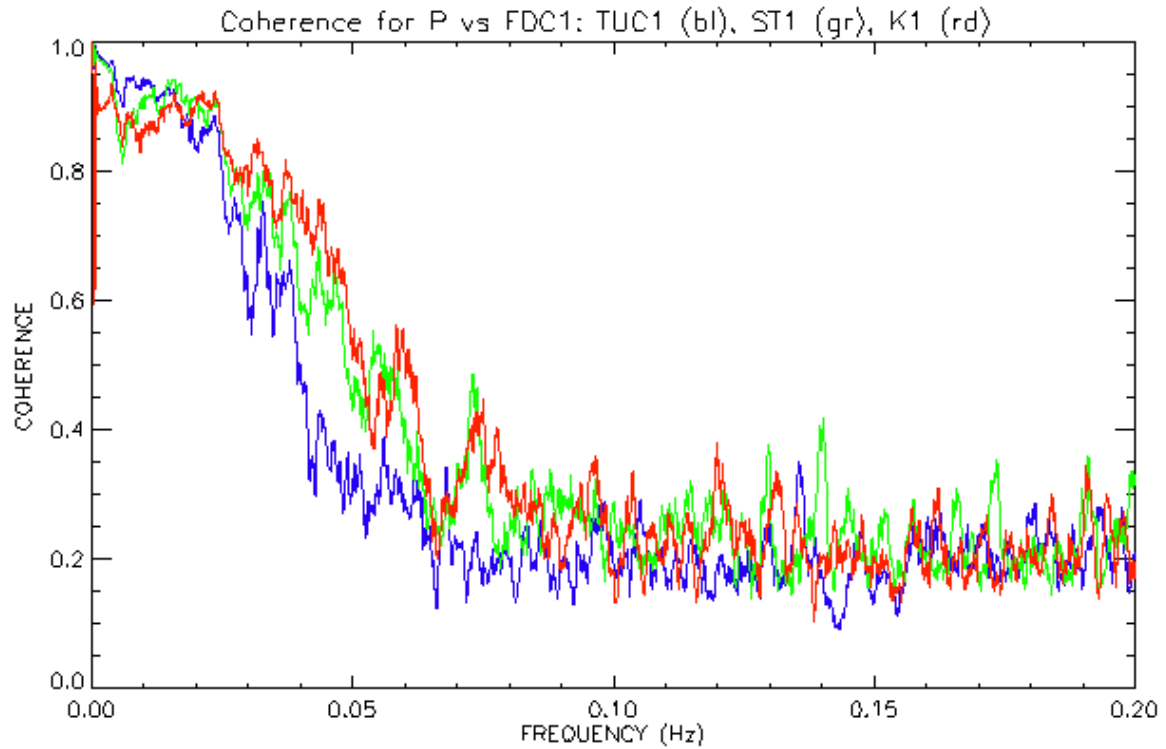


Figure A.15 Coherence of TF at P vs. TF at TUC1 (blue), ST1 (green), and K1 (red) for the night of July 11-12.

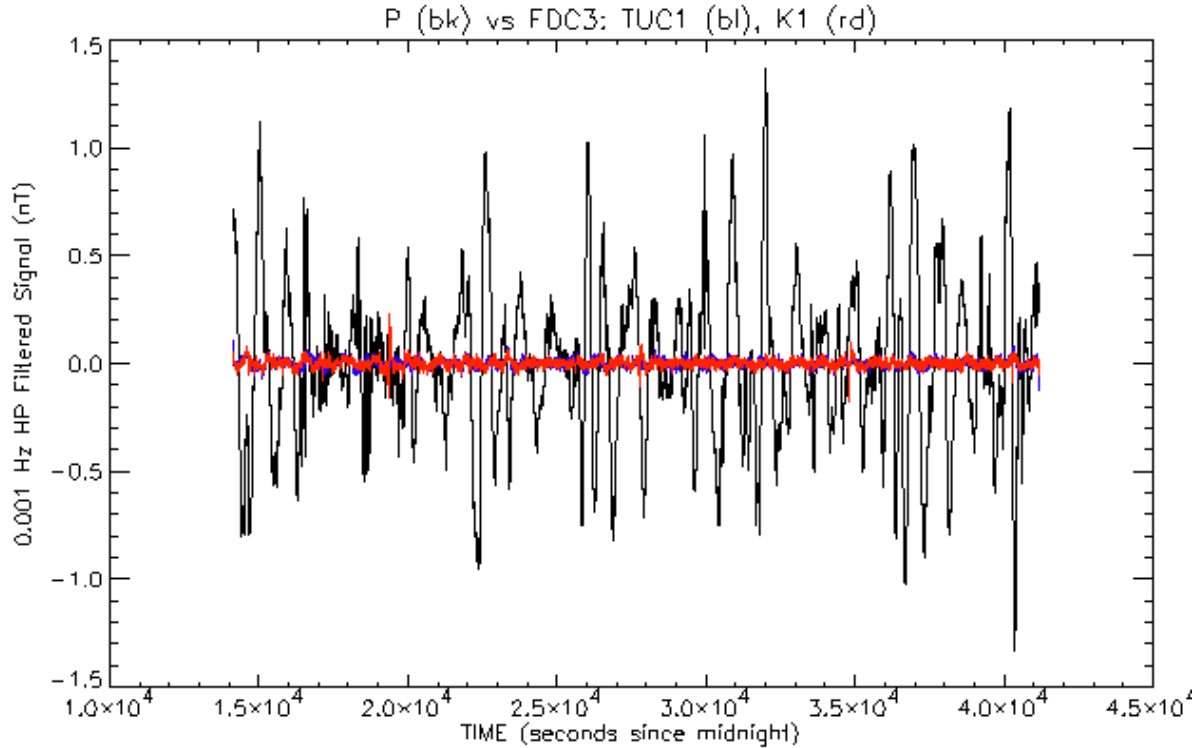


Figure A.16 TF from P (black) vs. Res3 from TUC1 (blue), K1 (red) on the night of July 11-12.

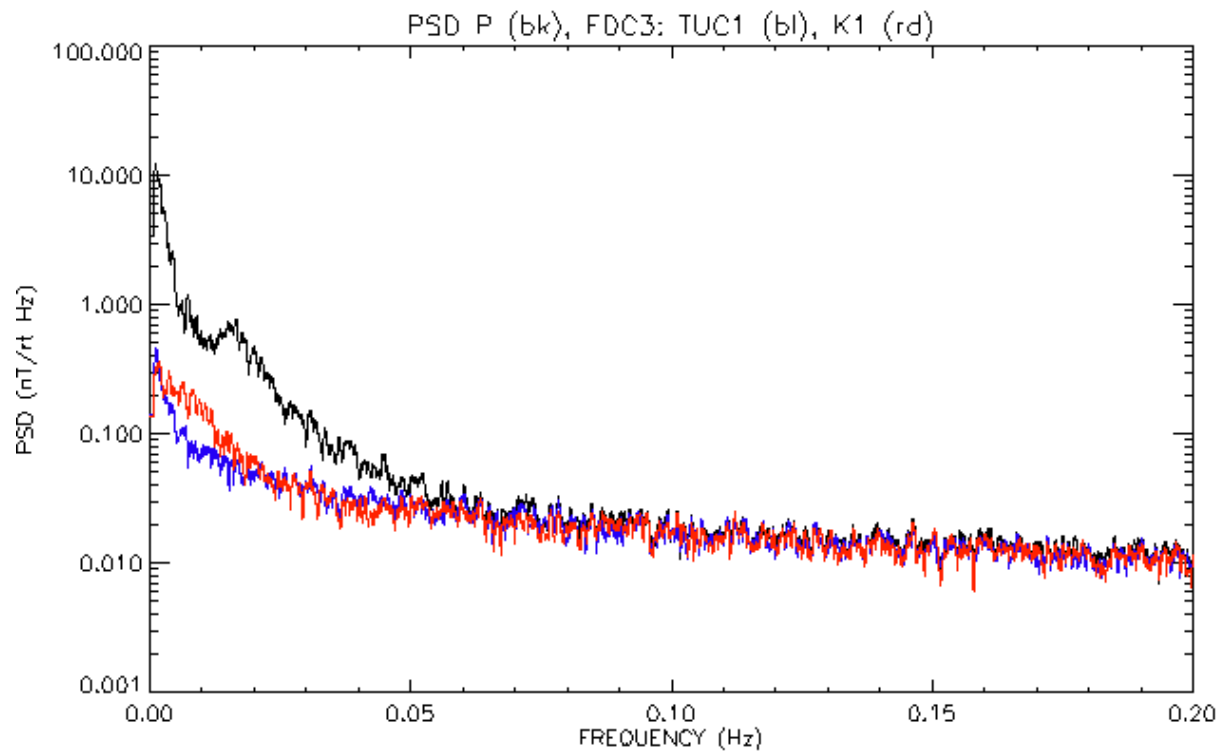


Figure A.17 PSD of TF at P vs. Res3 for TUC1 (blue), K1 (red) for the night of July 11-12.

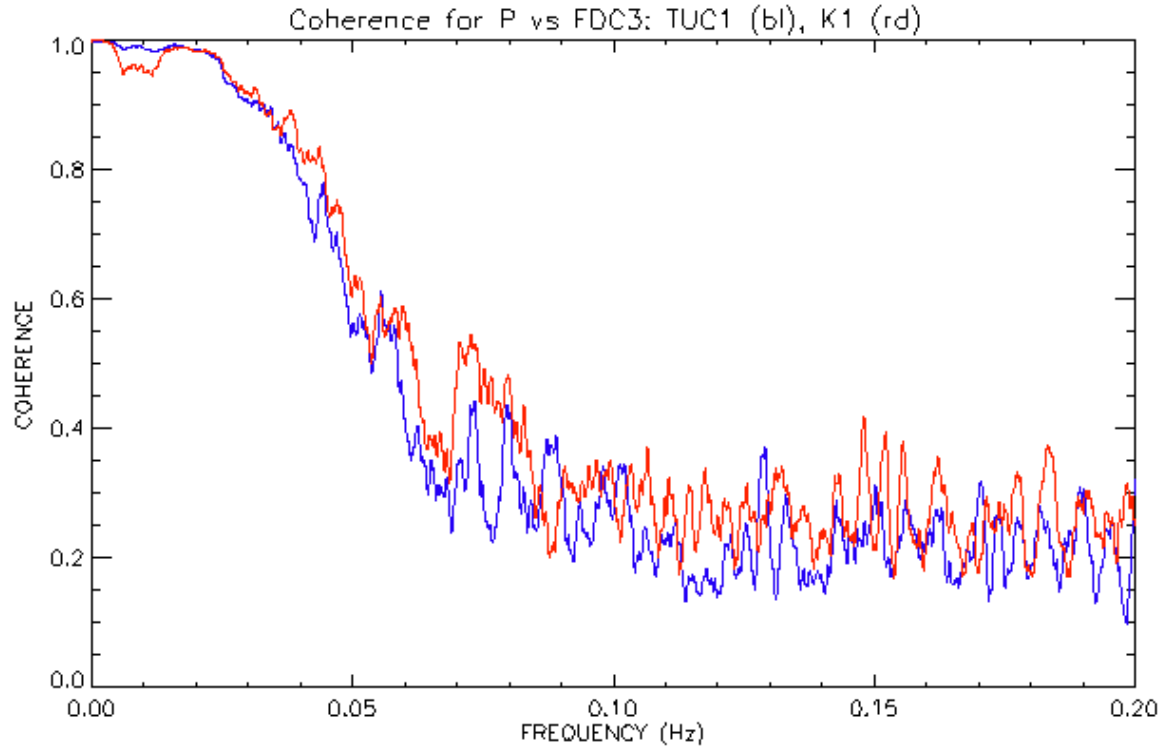


Figure A.18 Coherence of TF at P vs. (X,Y,Z) at TUC1 (blue), K1 (red) for the night of July 11-12.

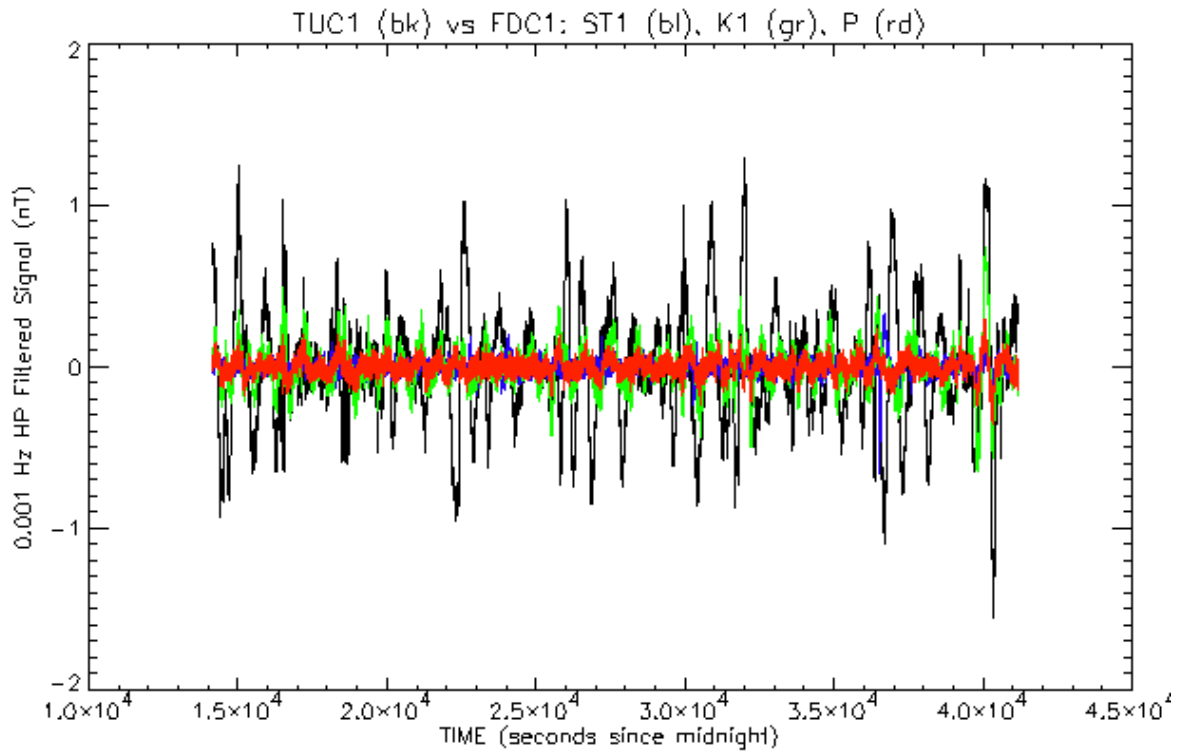


Figure A.19 TF from TUC1 (black) vs. Res1 for ST1 (blue), K1 (green), and P (red) on the night of July 11-12.

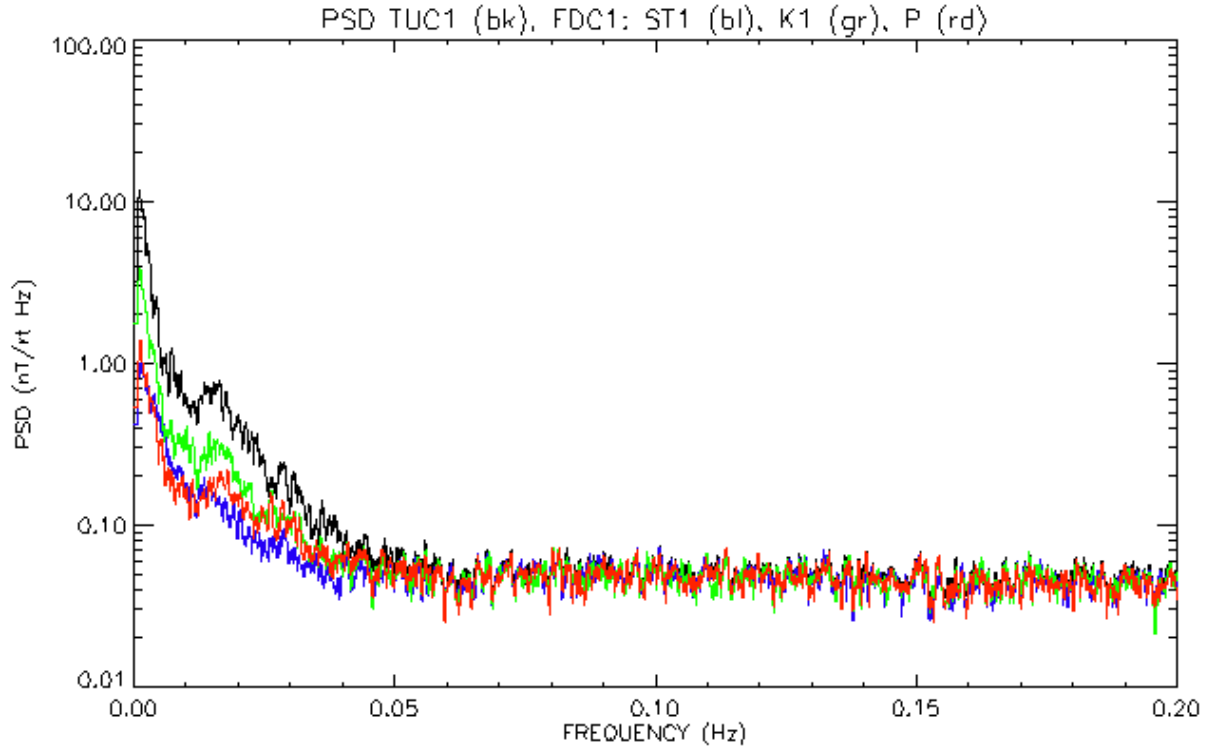


Figure A.20 PSD of TF at TUC1 (black) vs. Res1 for ST1 (blue), K1 (green), and P (red) for the night of July 11-12.

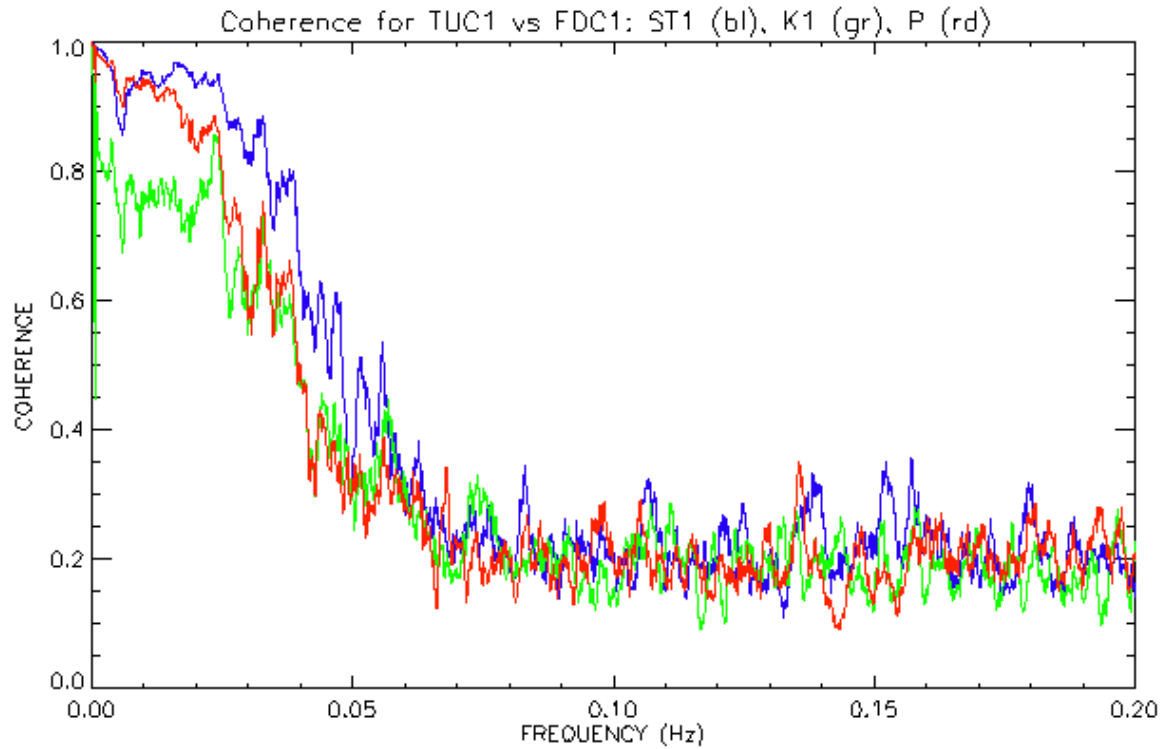


Figure A.21 Coherence of TF at TUC1 vs. TF at ST1 (blue), K1 (green), and P (red) for the night of July 11-12.

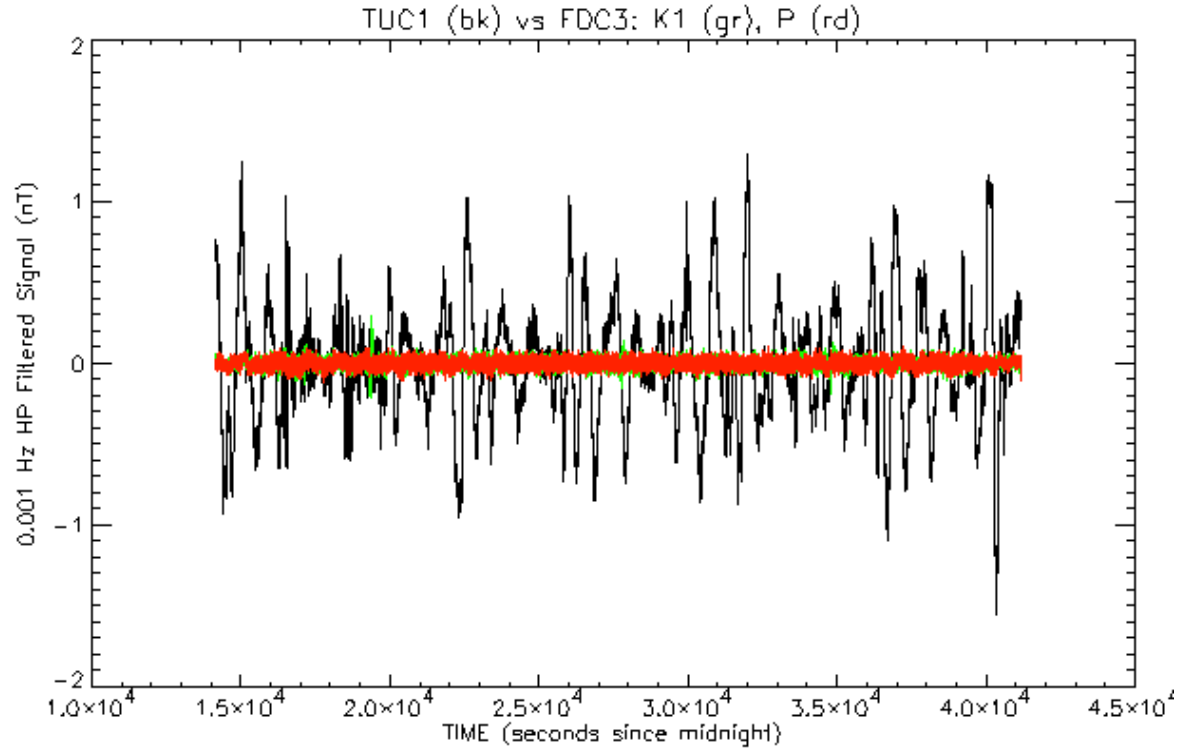


Figure A.22 TF from TUC1 (black) vs. Res3 from K1 (green), and P (red) on the night of July 11-12.

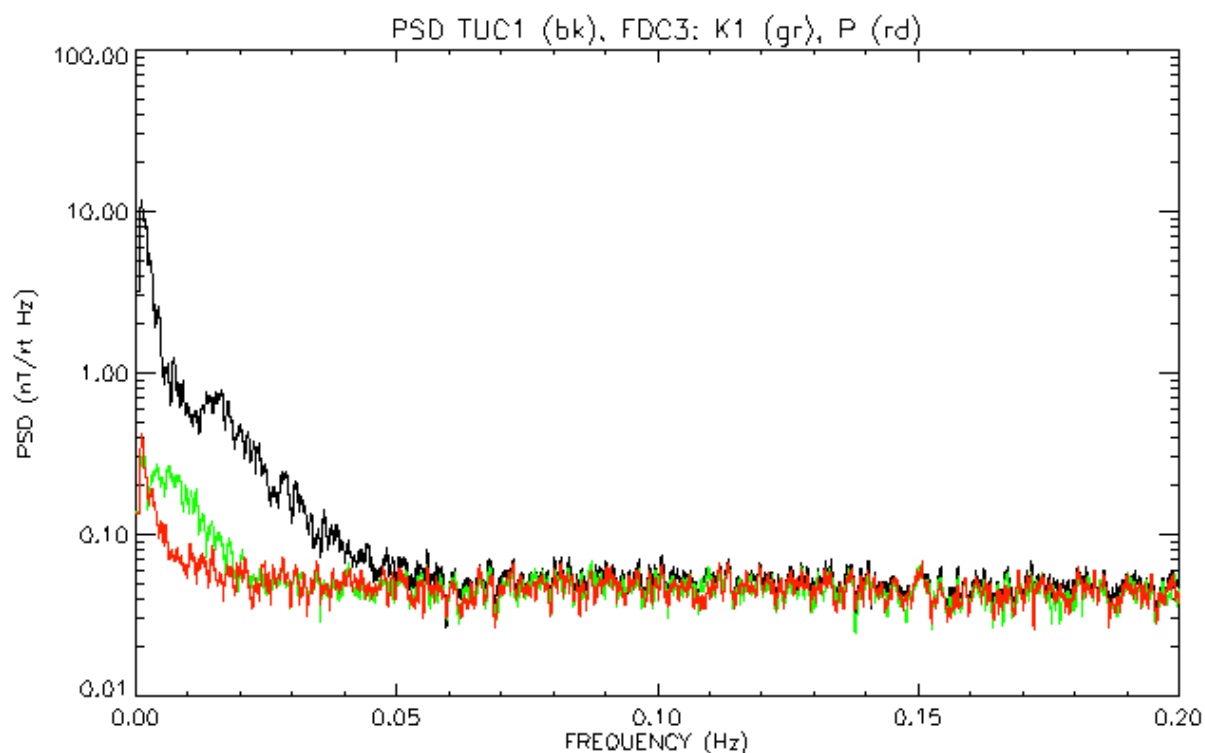


Figure A.23 PSD of TF at TUC1 vs. Res3 for K1 (green), and P (red) for the night of July 11-12.

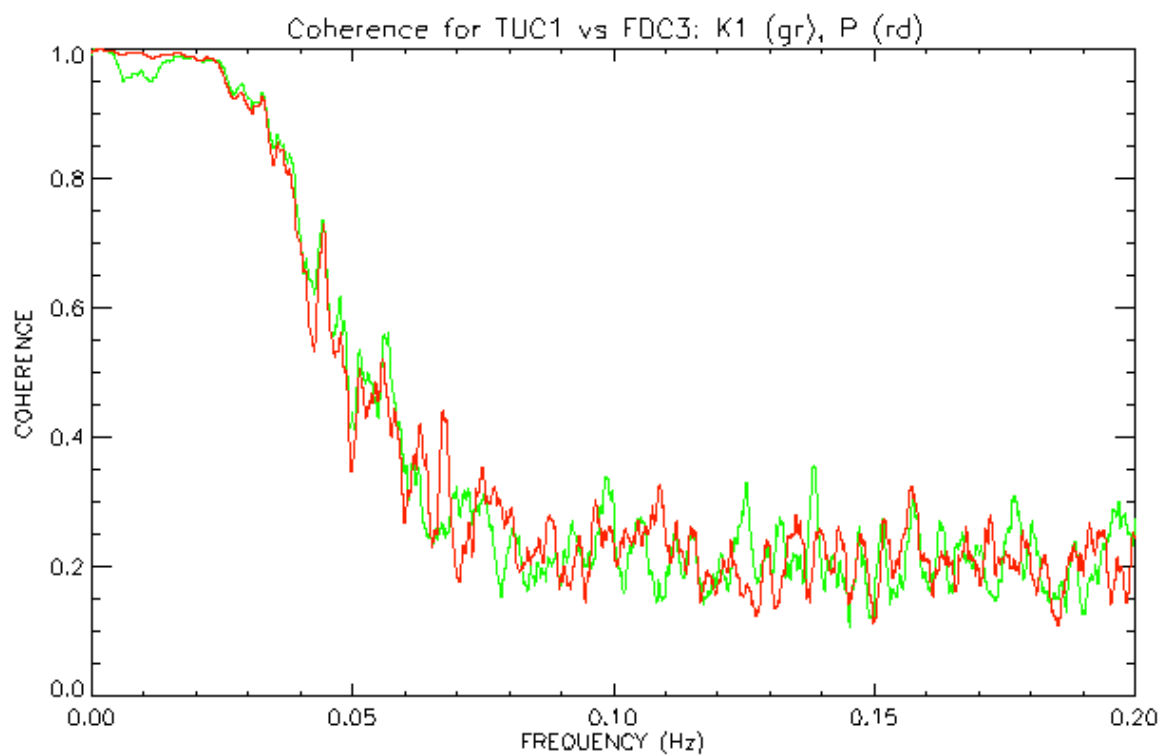


Figure A.24 Coherence of TF at TUC1 vs. (X,Y,Z) at K1 (green), and P (red) for the night of July 11-12.

A.2 Night of July 12-13

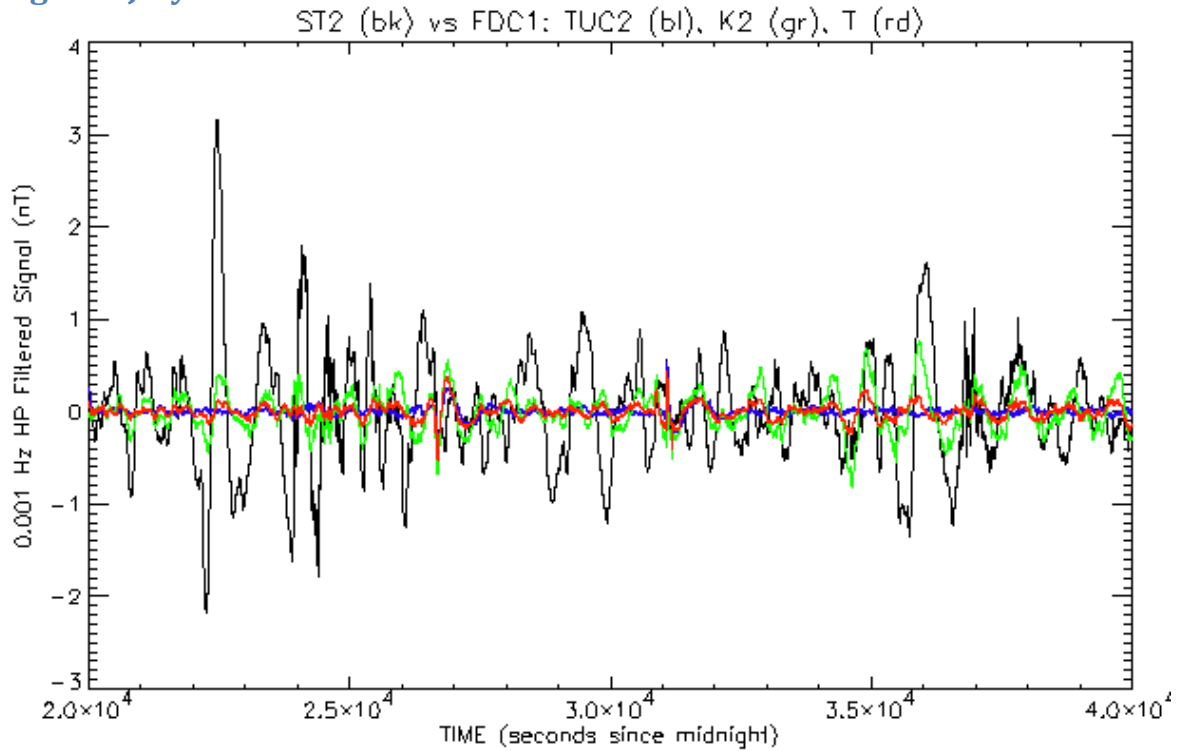


Figure A.25 TF from ST2 (black) vs. Res1 for TUC2 (blue), K2 (green), and T (red) on the night of July 12-13.

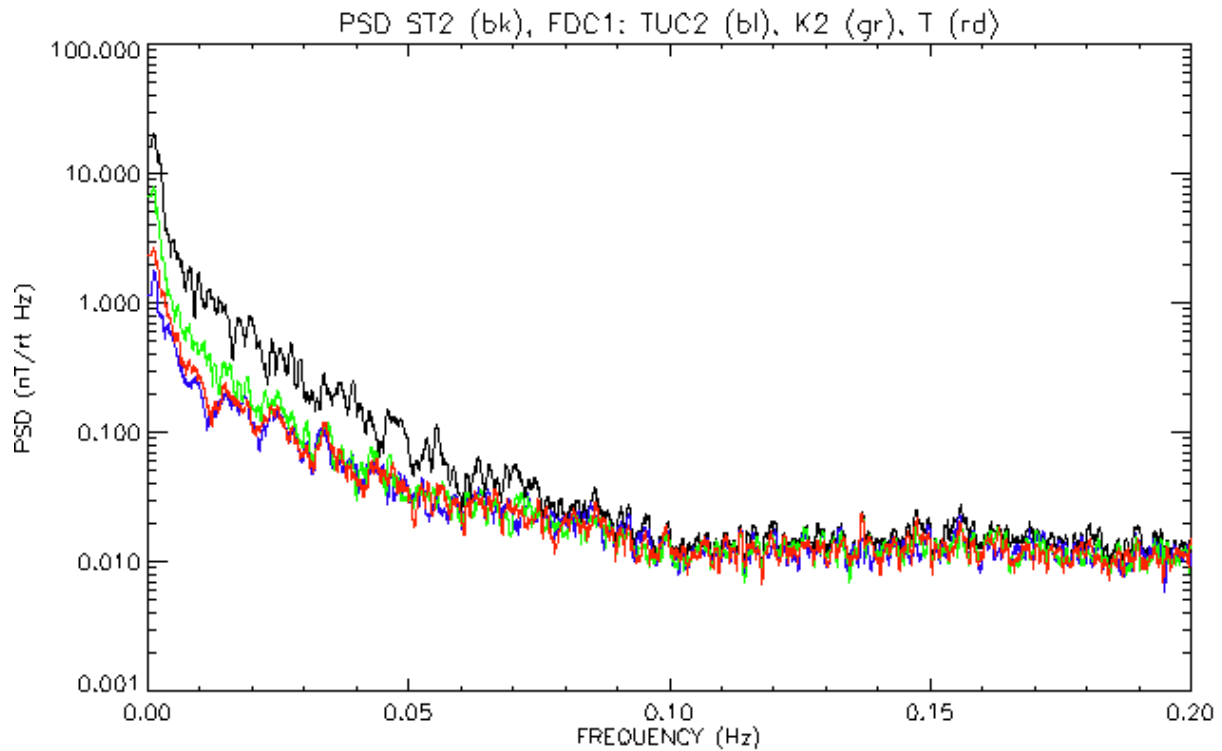


Figure A.26 PSD of TF at ST2 (black) vs. Res1 for TUC2 (blue), K2 (green), and T (red) for the night of July 12-13.

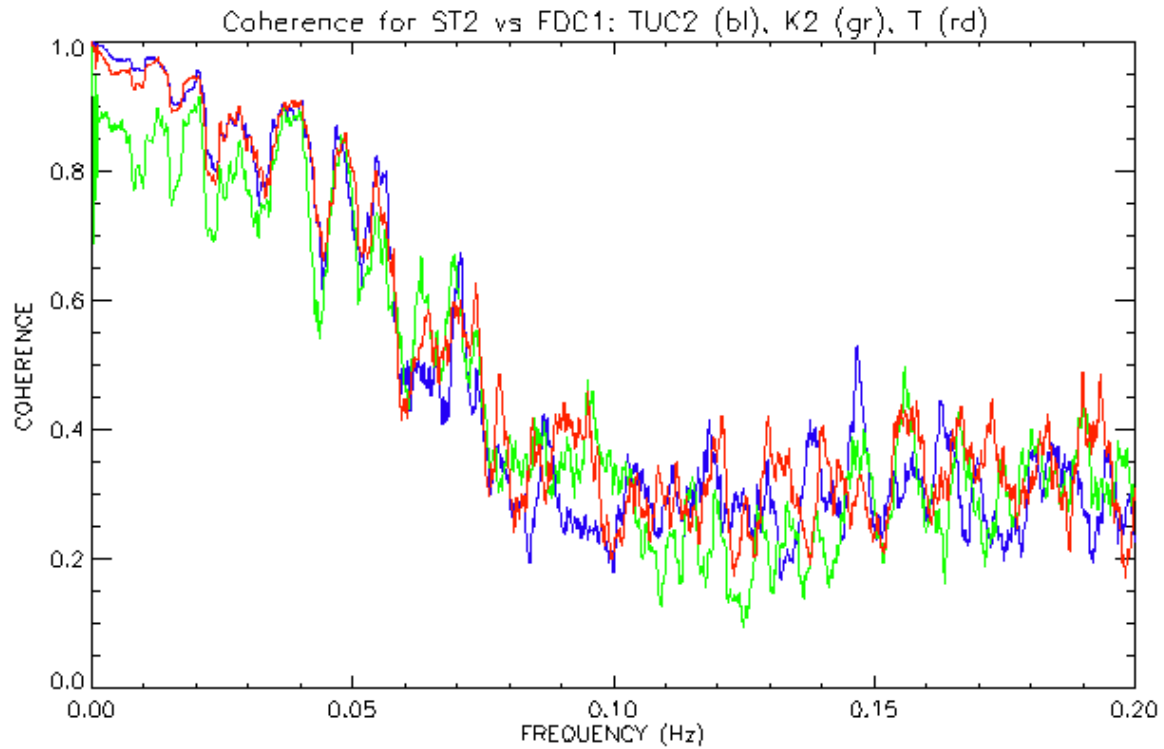


Figure A.27 Coherence of TF at ST2 vs. TF at TUC2 (blue), K2 (green), and T (red) for the night of July 12-13.

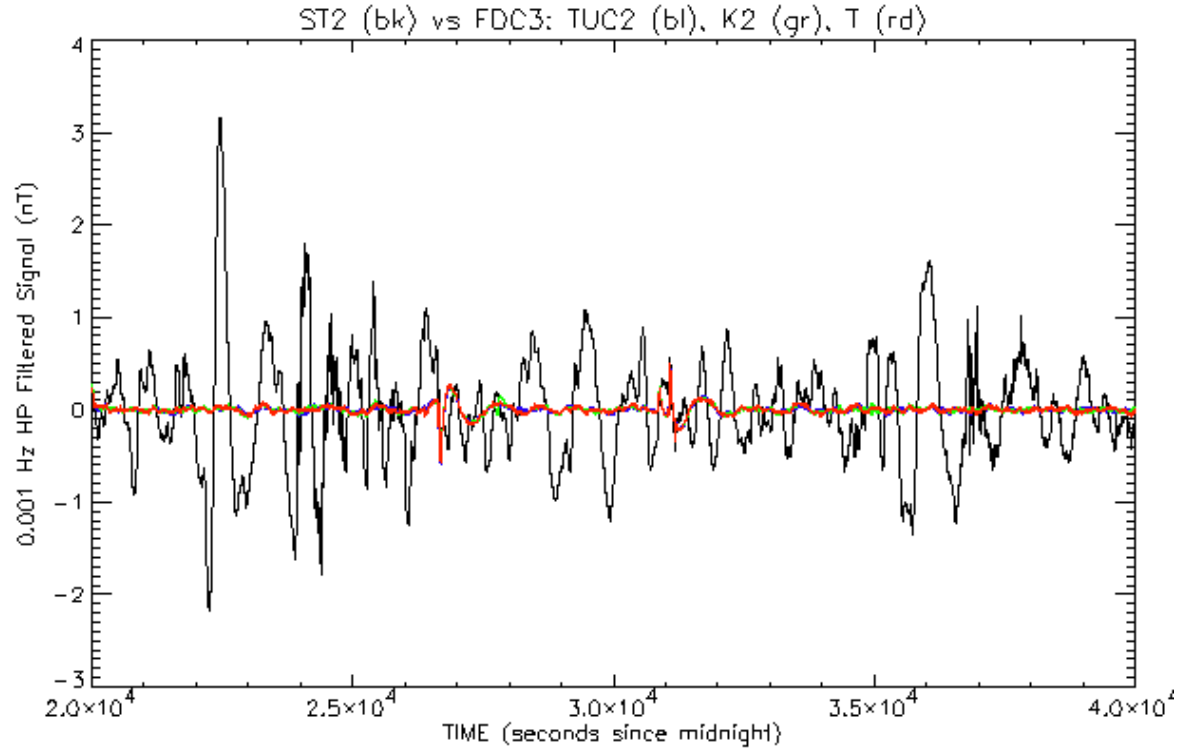


Figure A.28 TF from ST2 (black) vs. Res3 from TUC2 (blue), K2 (green), and T (red) on the night of July 12-13.

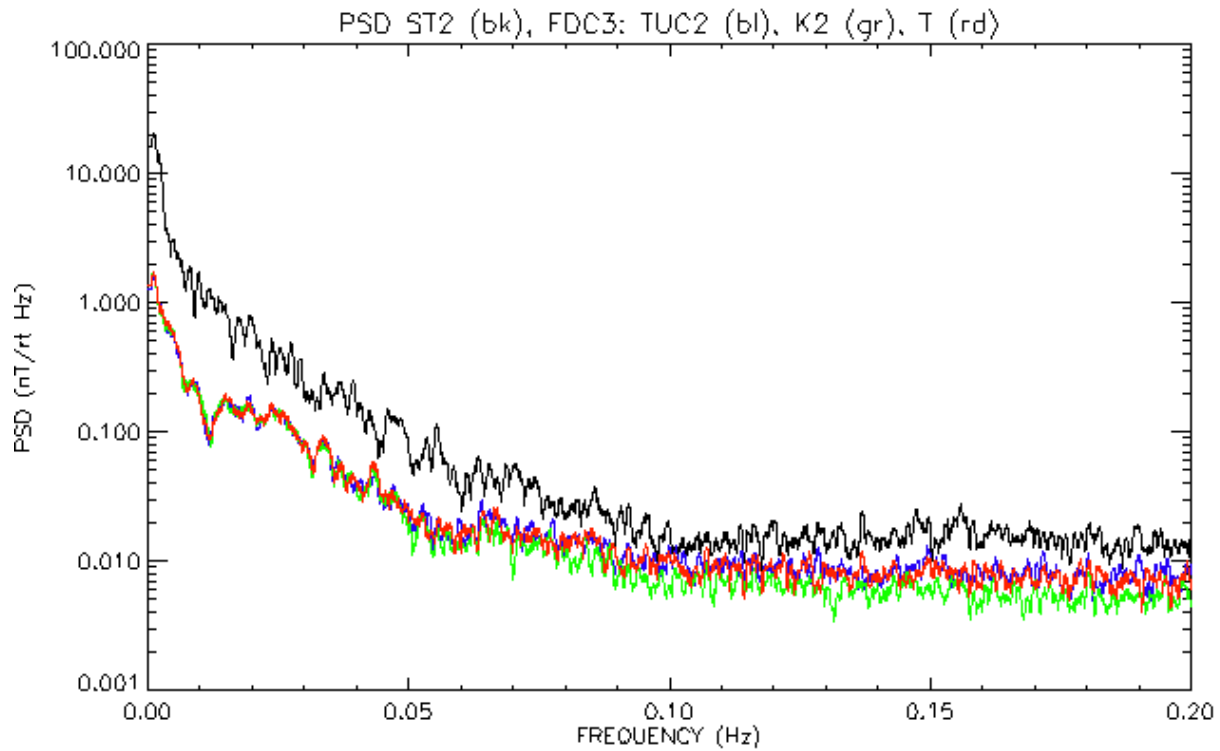


Figure A.29 PSD of TF at ST2 vs. Res3 for TUC2 (blue), K2 (green), and T (red) for the night of July 12-13.

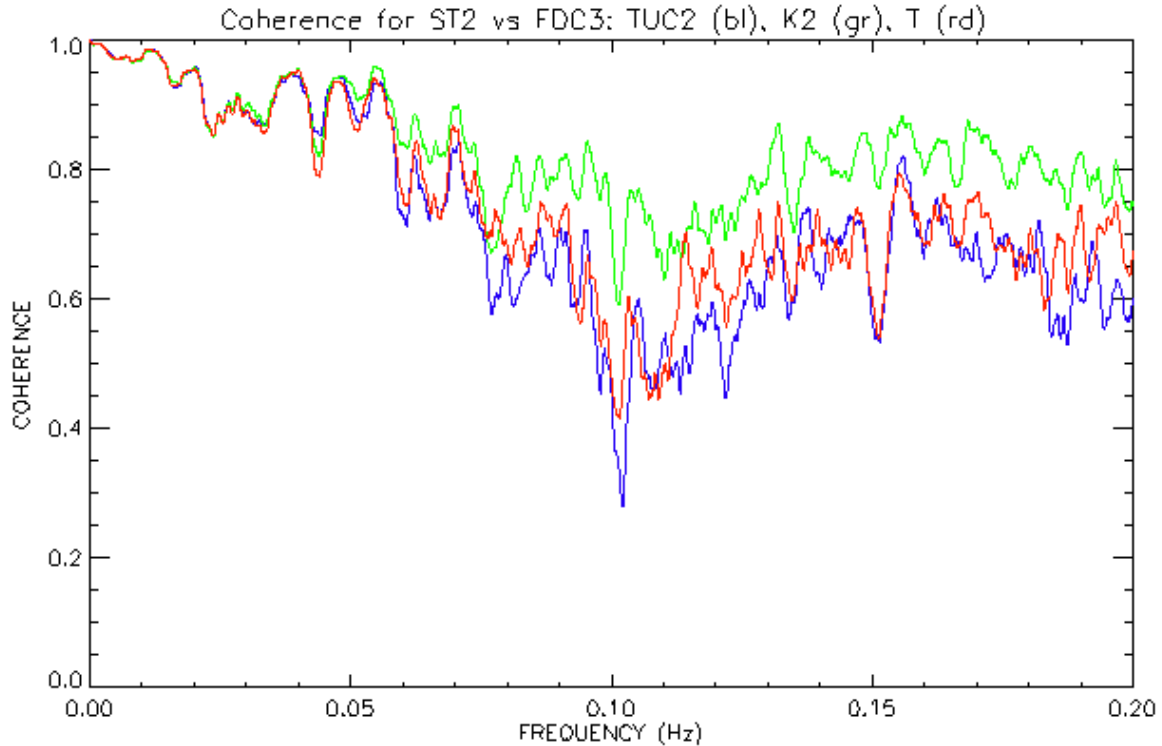


Figure A.30 Coherence of TF at ST2 vs. (X,Y,Z) at TUC2 (blue), K2 (green), and T (red) for the night of July 12-13.

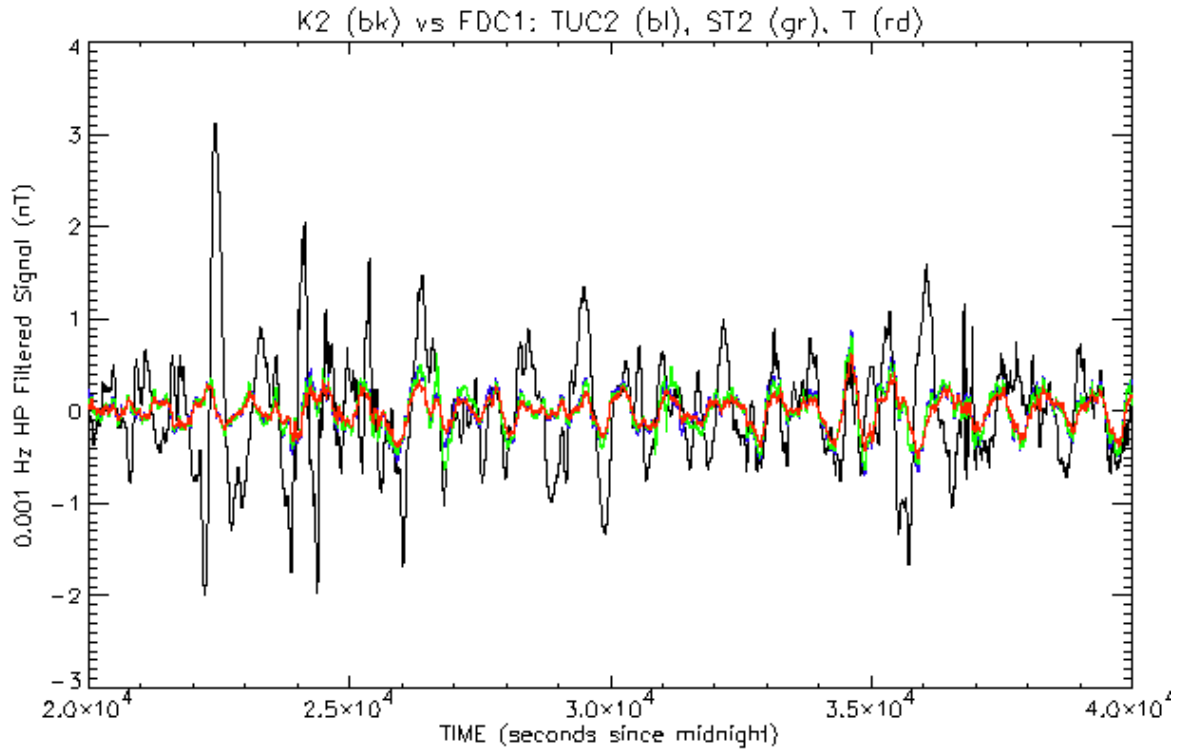


Figure A.31 TF from K2 (black) vs. Res1 for TUC2 (blue), ST2 (green), and T (red) on the night of July 12-13.

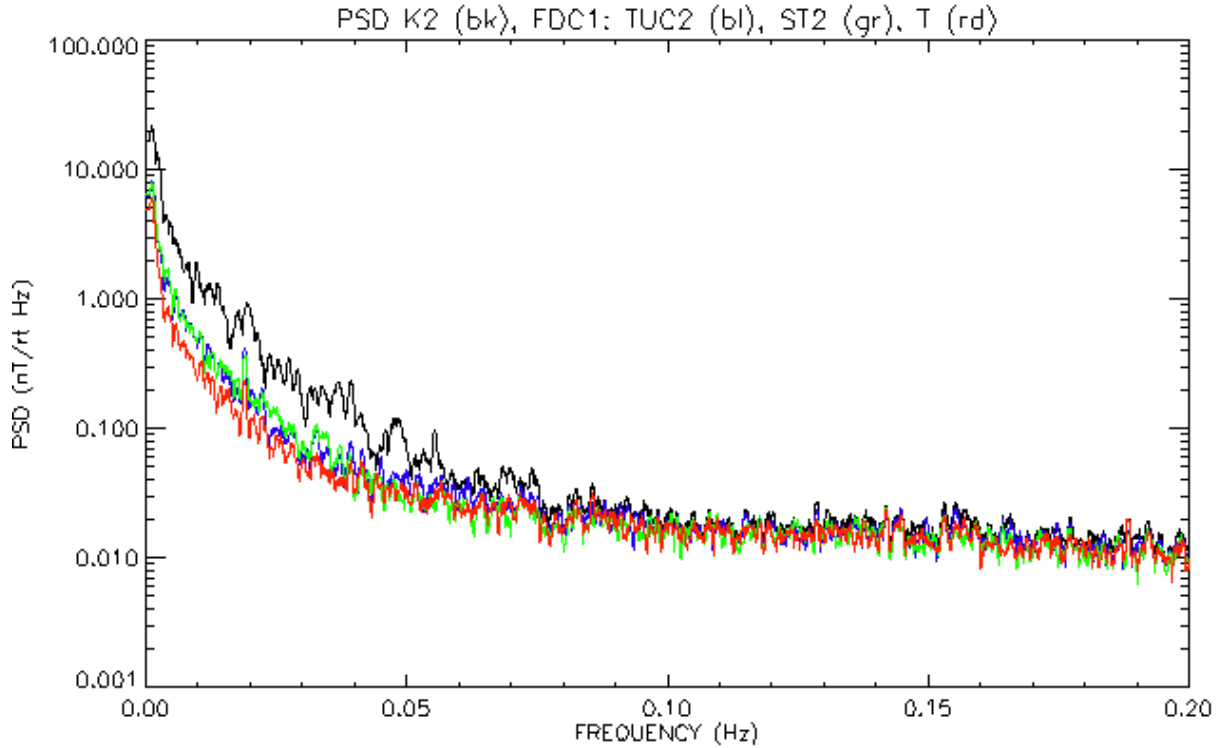


Figure A.32 PSD of TF at K2 (black) vs. Res1 for TUC2 (blue), ST2 (green), and T (red) for the night of July 12-13.

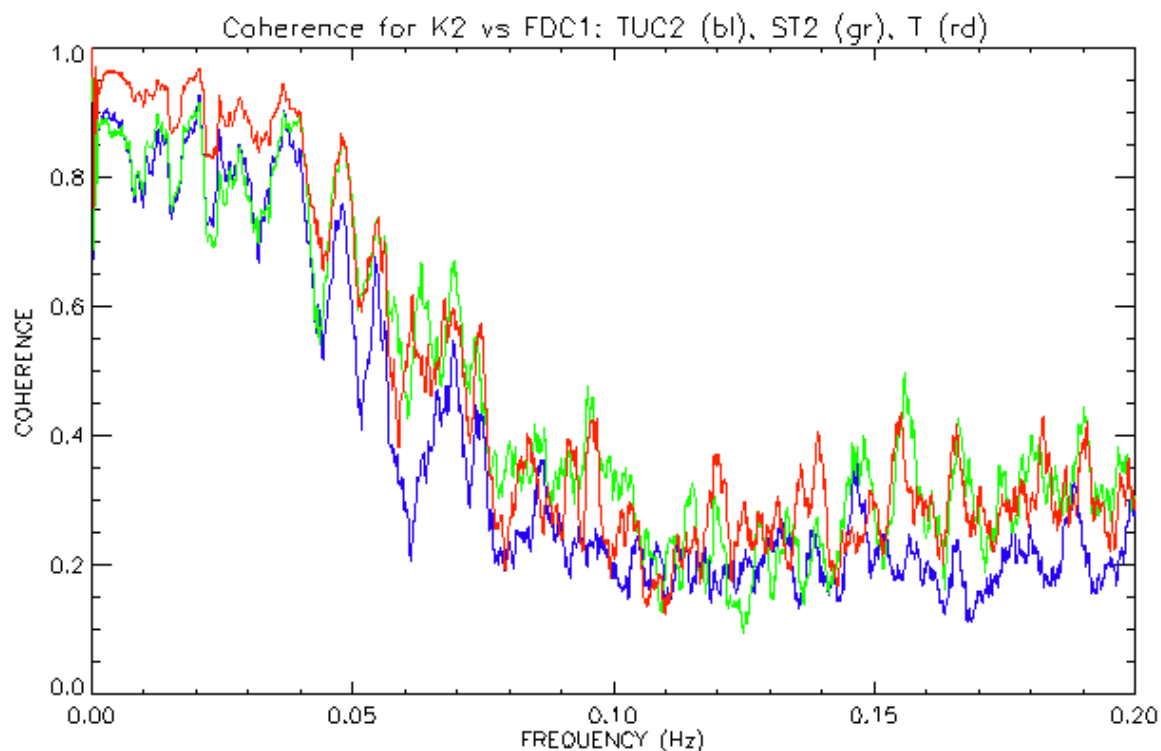


Figure A.33 Coherence of TF at K2 vs. TF at TUC2 (blue), ST2 (green), and T (red) for the night of July 12-13.

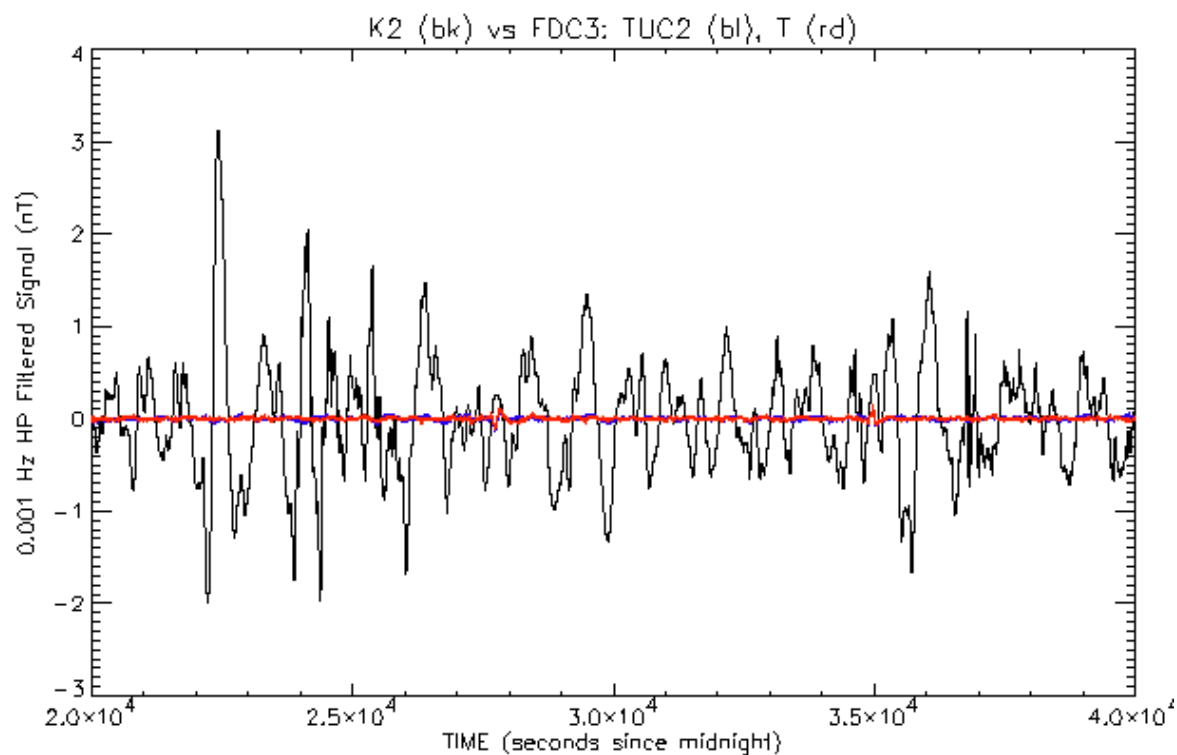


Figure A.34 TF from K2 (black) vs. Res3 from TUC2 (blue), and T (red) on the night of July 12-13.

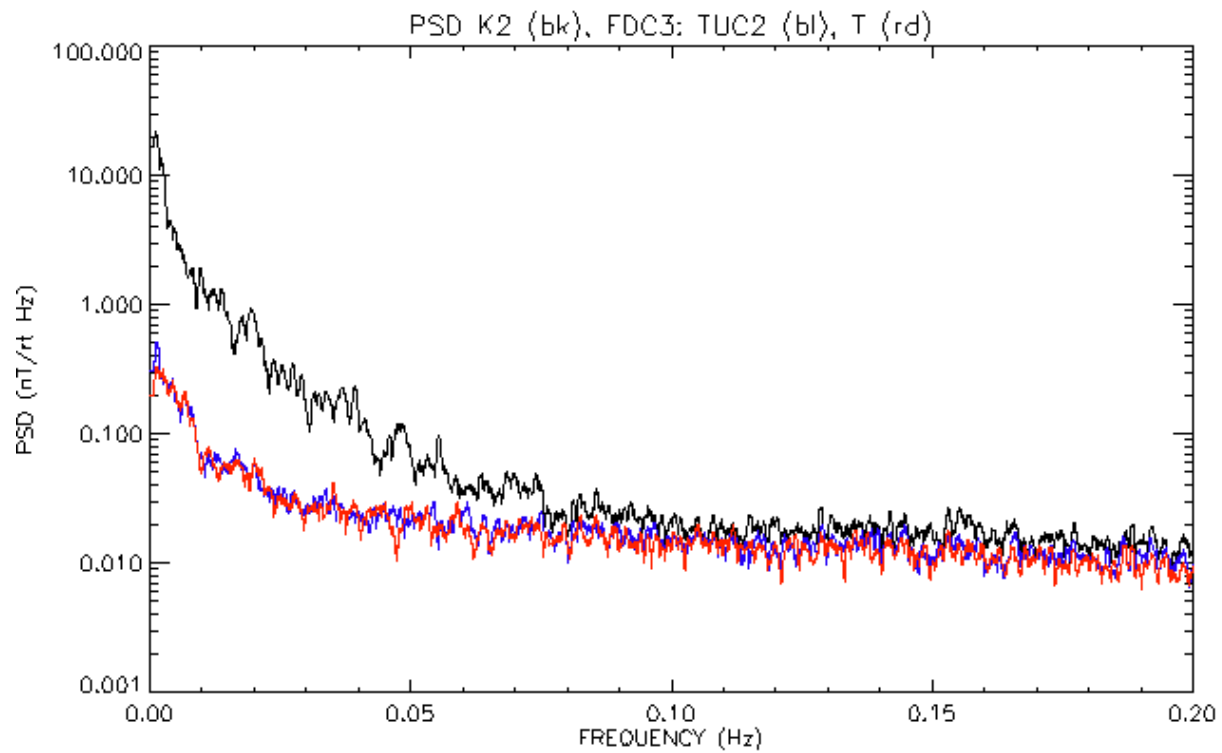


Figure A.35 PSD of TF at K2 vs. Res3 for TUC2 (blue), and T (red) for the night of July 12-13.

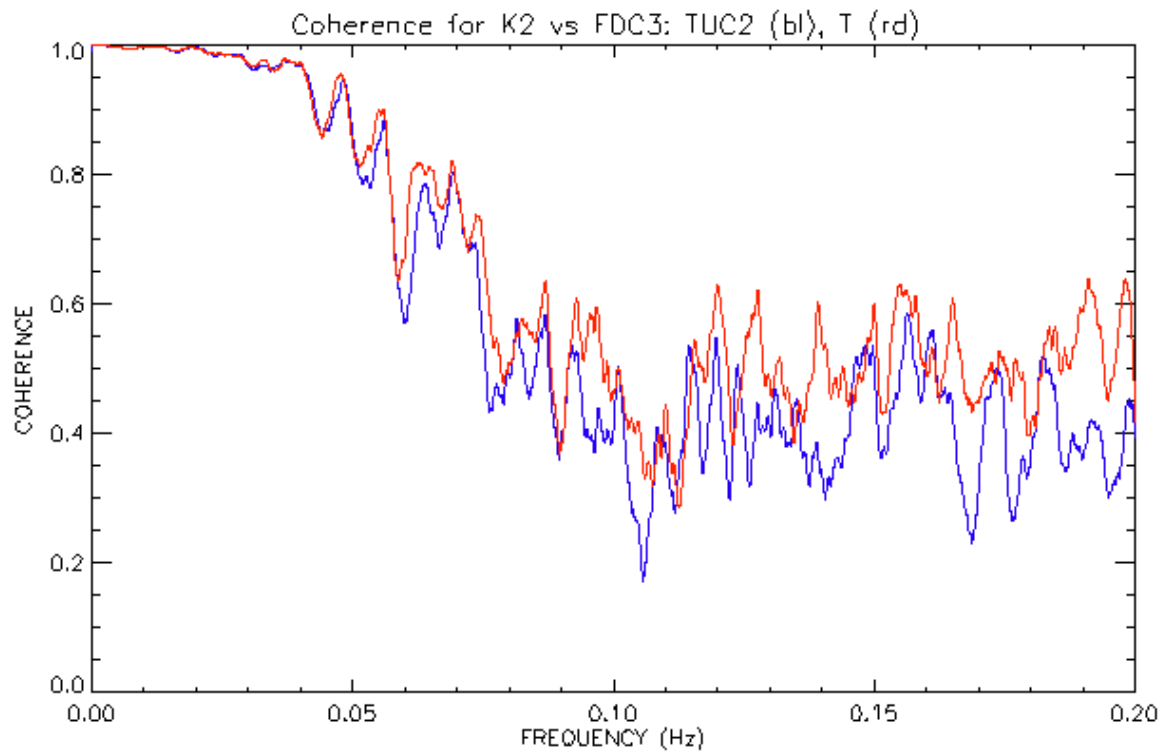


Figure A.36 Coherence of TF at K2 vs. (X,Y,Z) at TUC2 (blue), and T (red) for the night of July 12-13.

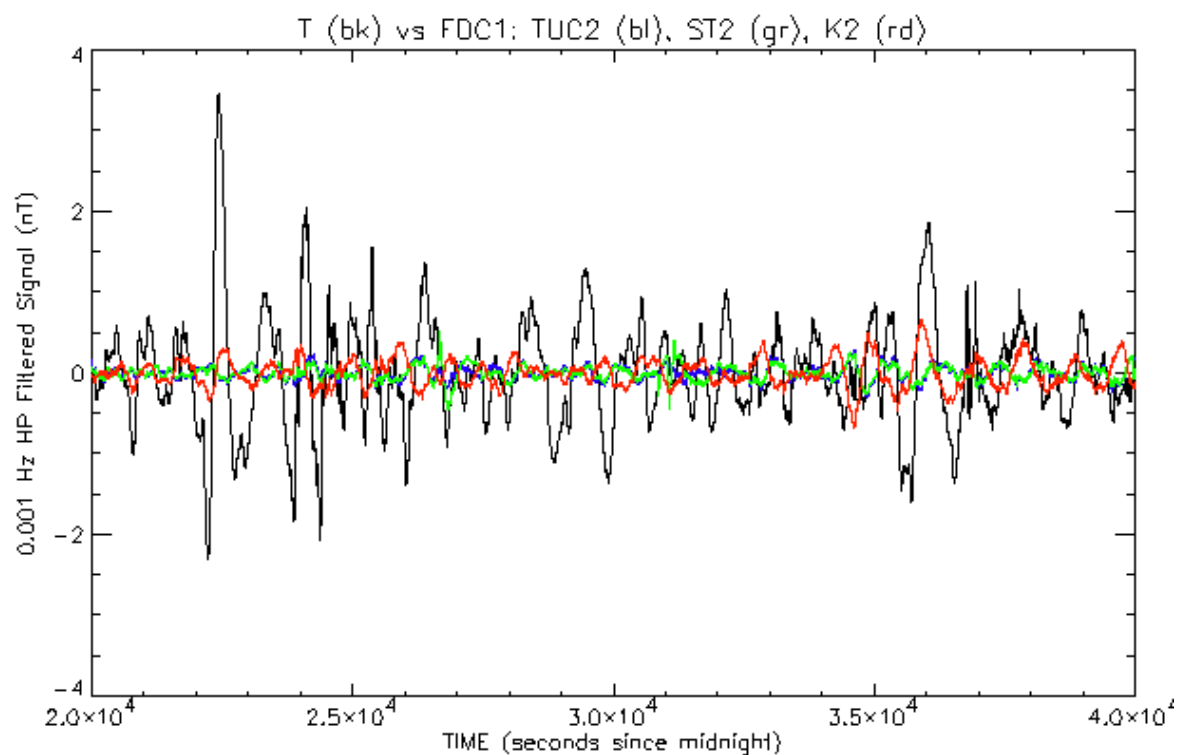


Figure A.37 TF from T (black) vs. Res1 for TUC2 (blue), ST2 (green), and K2 (red) on the night of July 12-13.

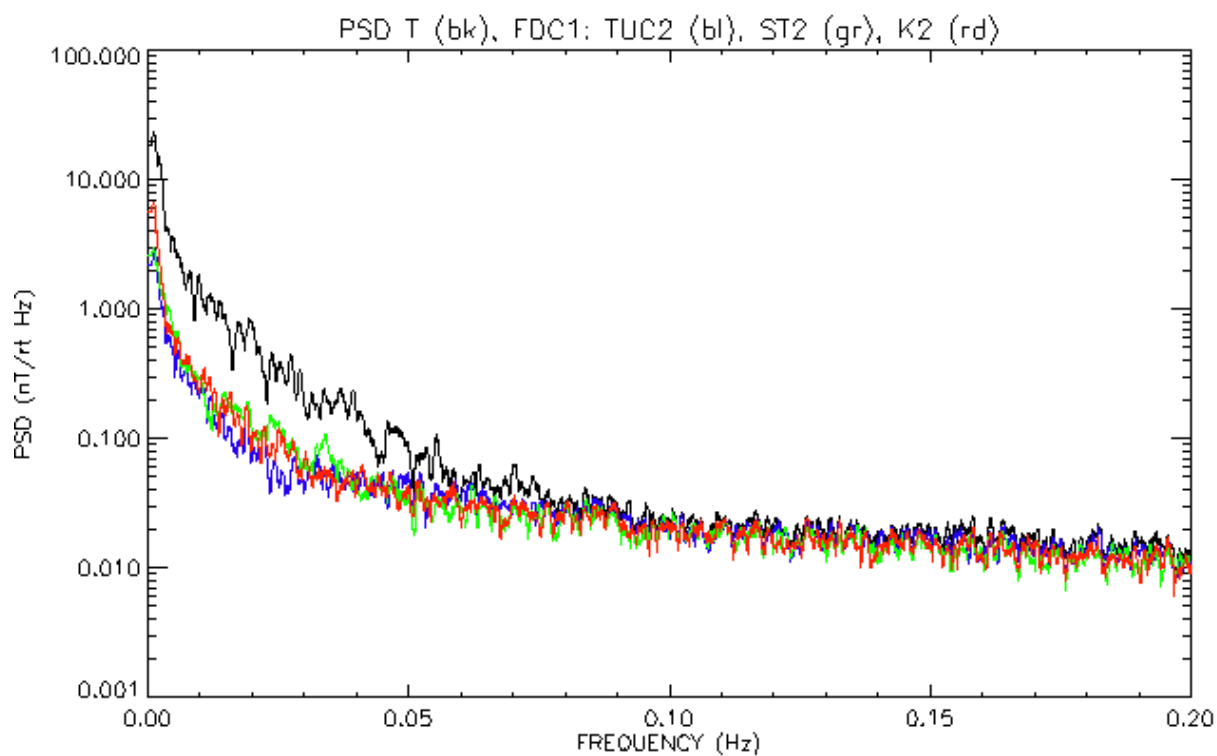


Figure A.38 PSD of TF at T (black) vs. Res1 for TUC2 (blue), ST2 (green), and K2 (red) for the night of July 12-13.

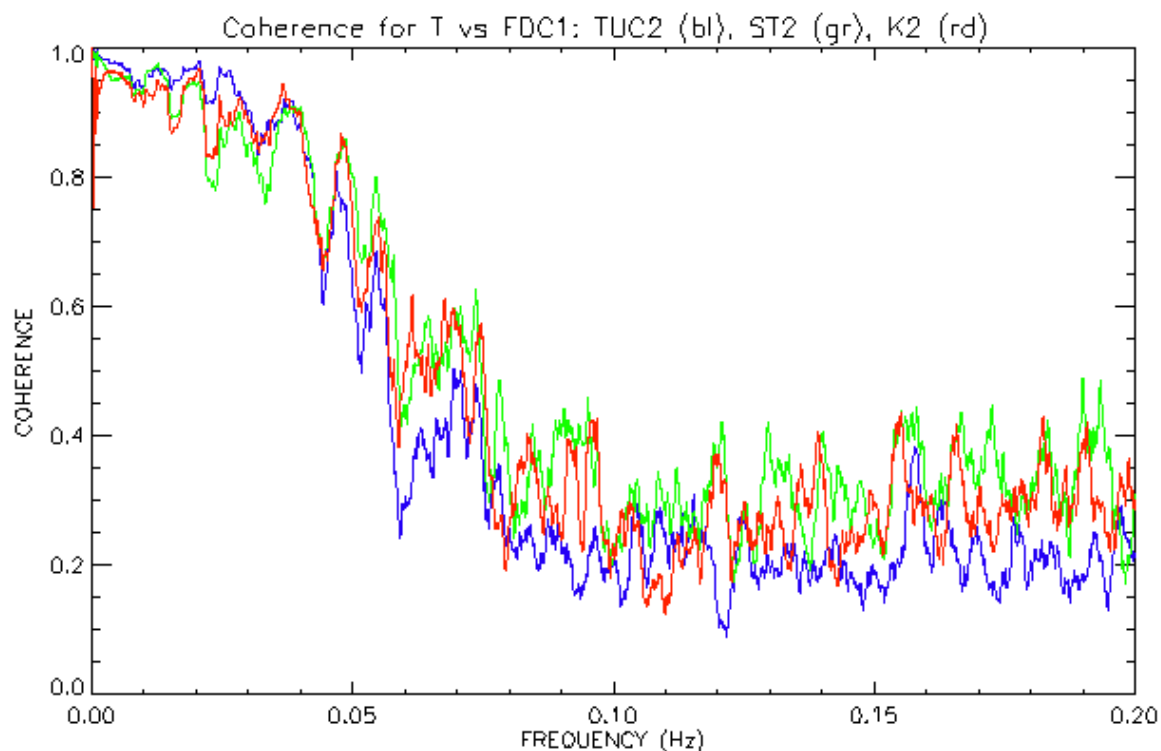


Figure A.39 Coherence of TF at T vs. TF at TUC2 (blue), ST2 (green), and K2 (red) for the night of July 12-13.

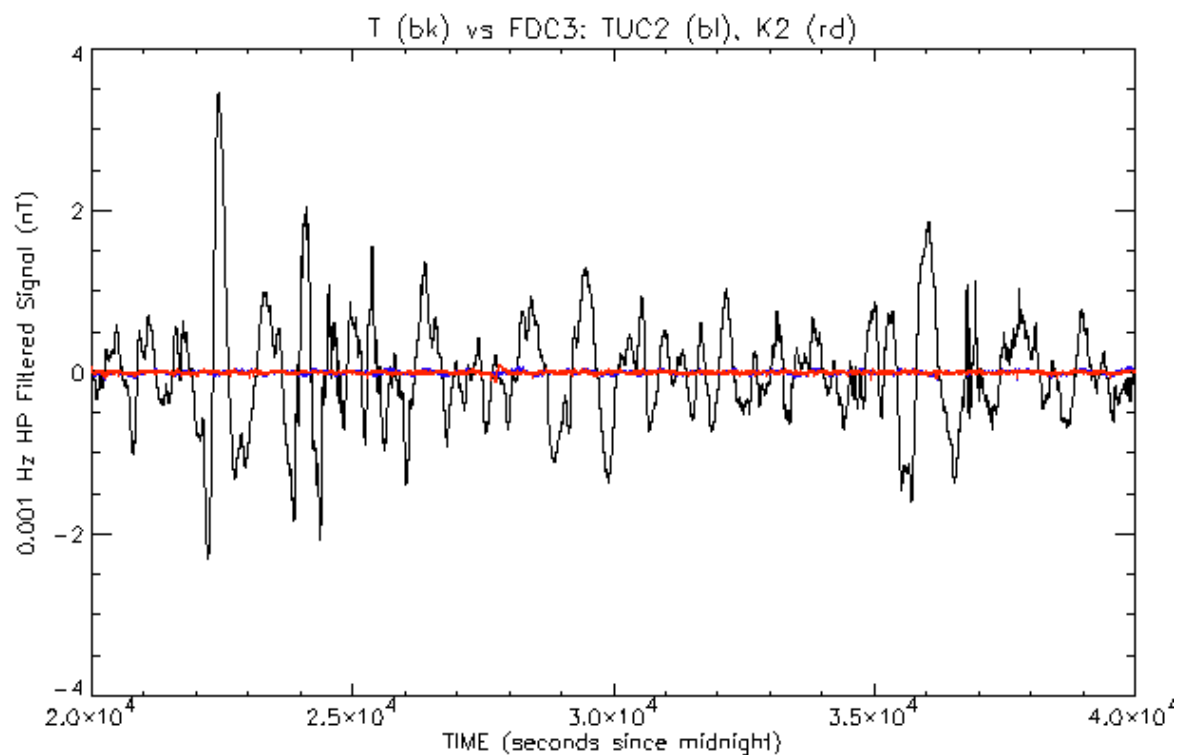


Figure A.40 TF from T (black) vs. Res3 from TUC2 (blue), K2 (red) on the night of July 12-13.

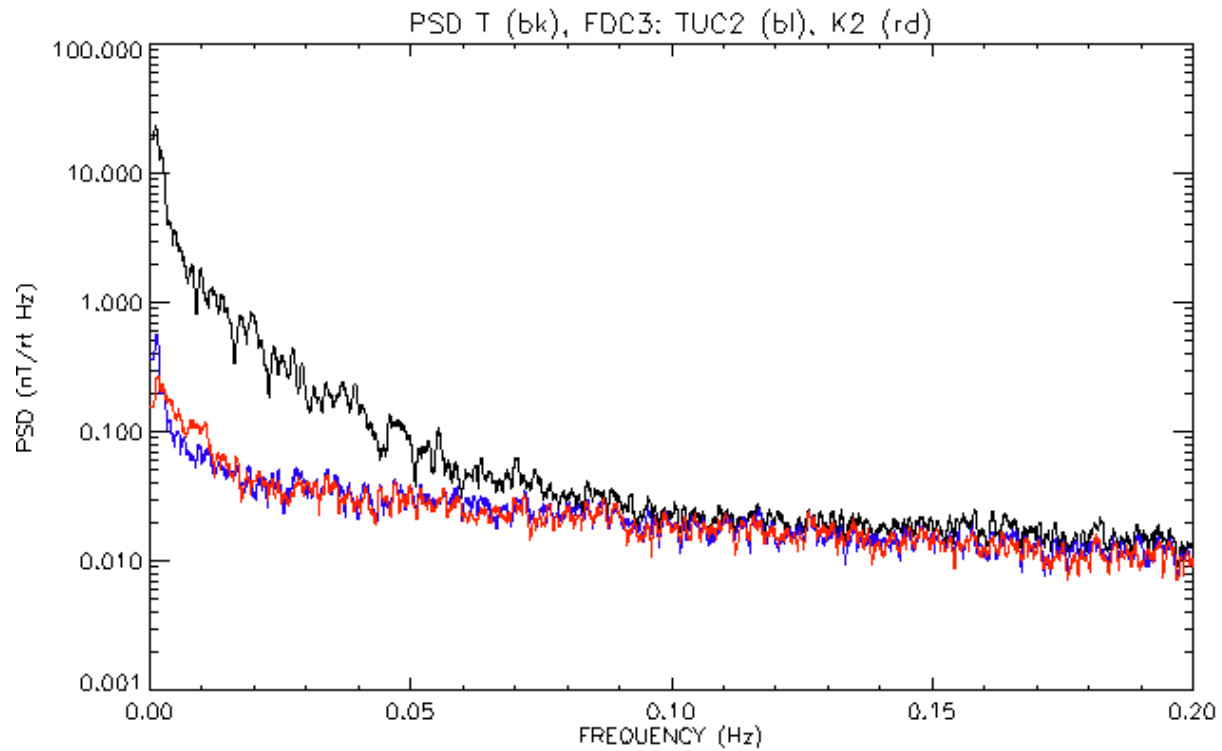


Figure A.41 PSD of TF at T vs. Res3 for TUC2 (blue), K2 (red) for the night of July 12-13.

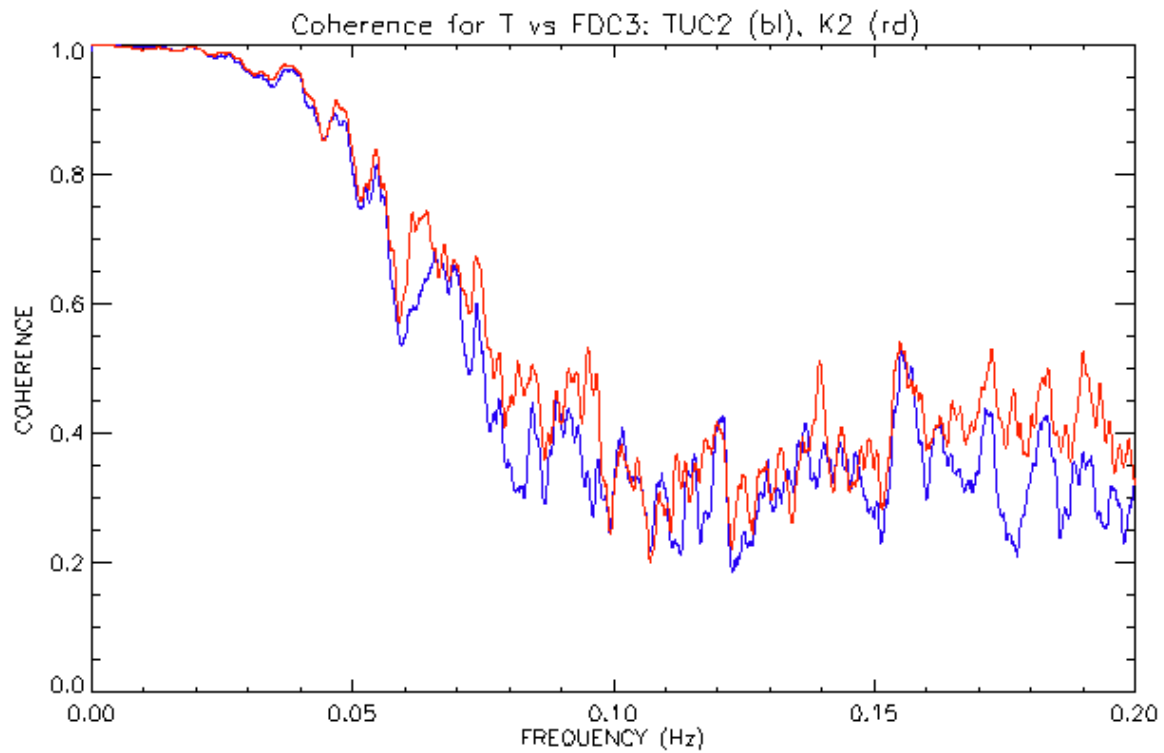


Figure A.42 Coherence of TF at T vs. (X,Y,Z) at TUC2 (blue), K2 (red) for the night of July 12-13.

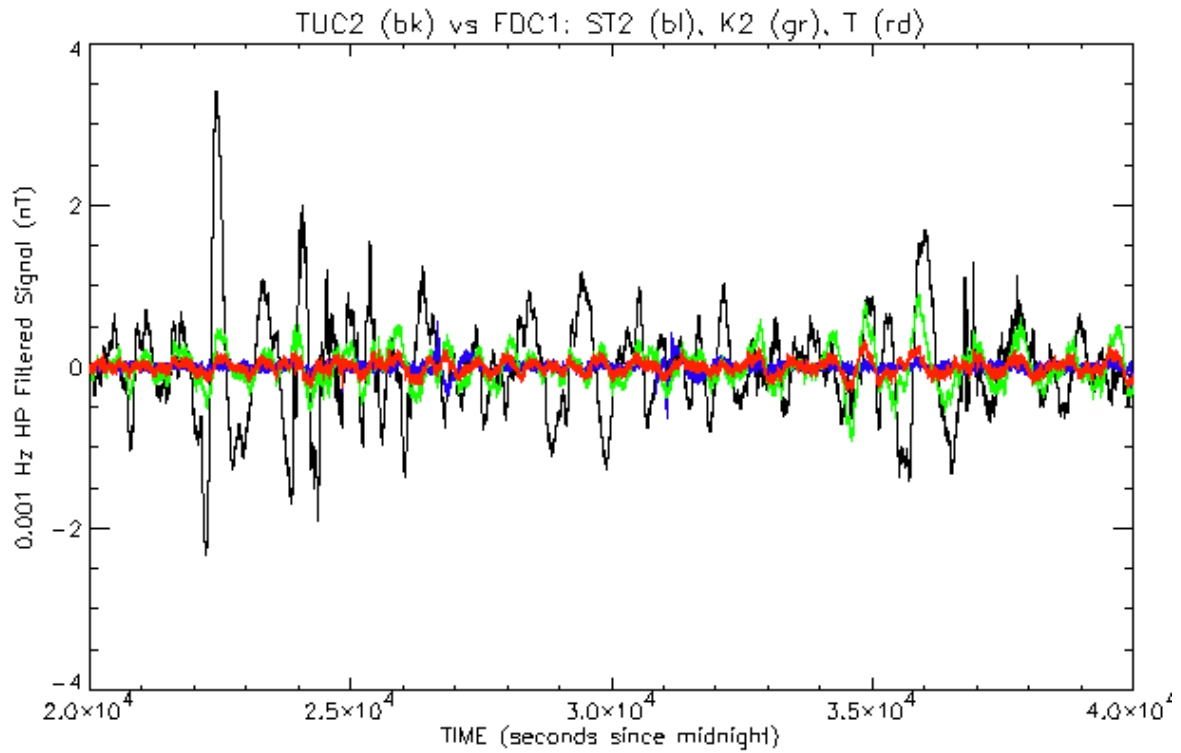


Figure A.43 TF from TUC2 (black) vs. Res1 for ST2 (blue), K2 (green), and T (red) on the night of July 12-13.

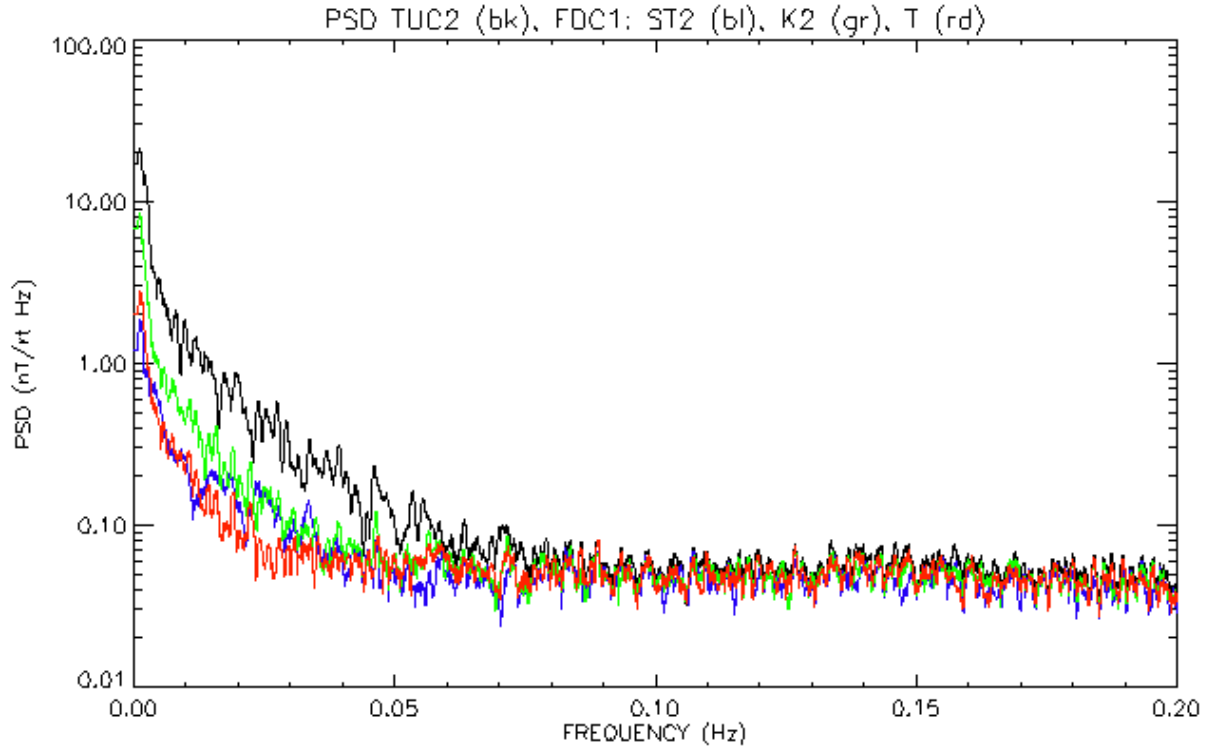


Figure A.44 PSD of TF at TUC2 (black) vs. Res1 for ST2 (blue), K2 (green), and T (red) for the night of July 12-13.

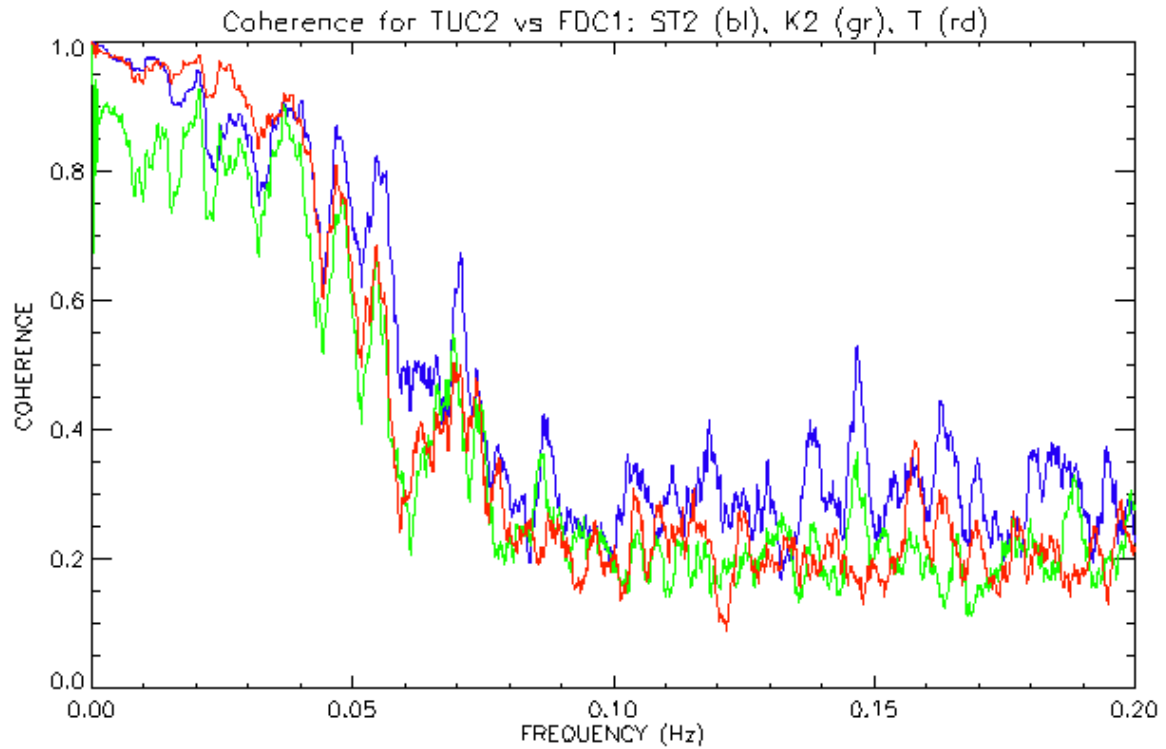


Figure A.45 Coherence of TF at TUC2 vs. TF at ST2 (blue), K2 (green), and T (red) for the night of July 12-13.

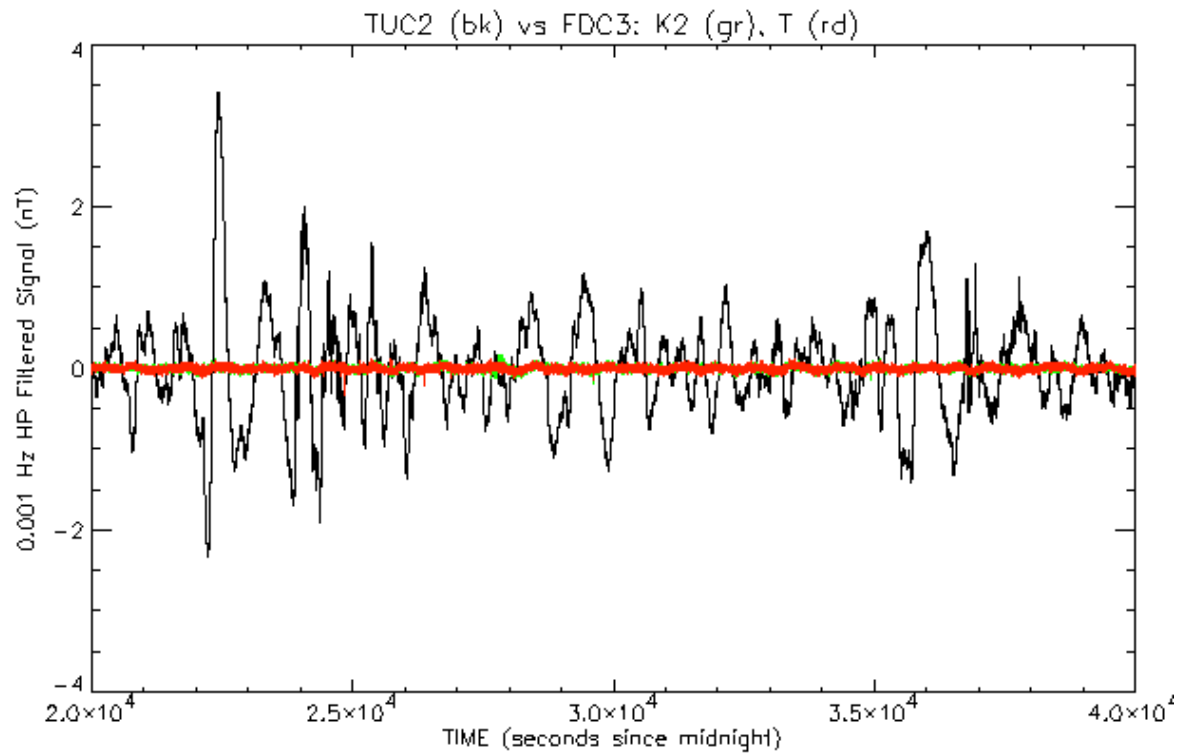


Figure A.46 TF from TUC2 (black) vs. Res3 from K2 (green), and T (red) on the night of July 12-13.

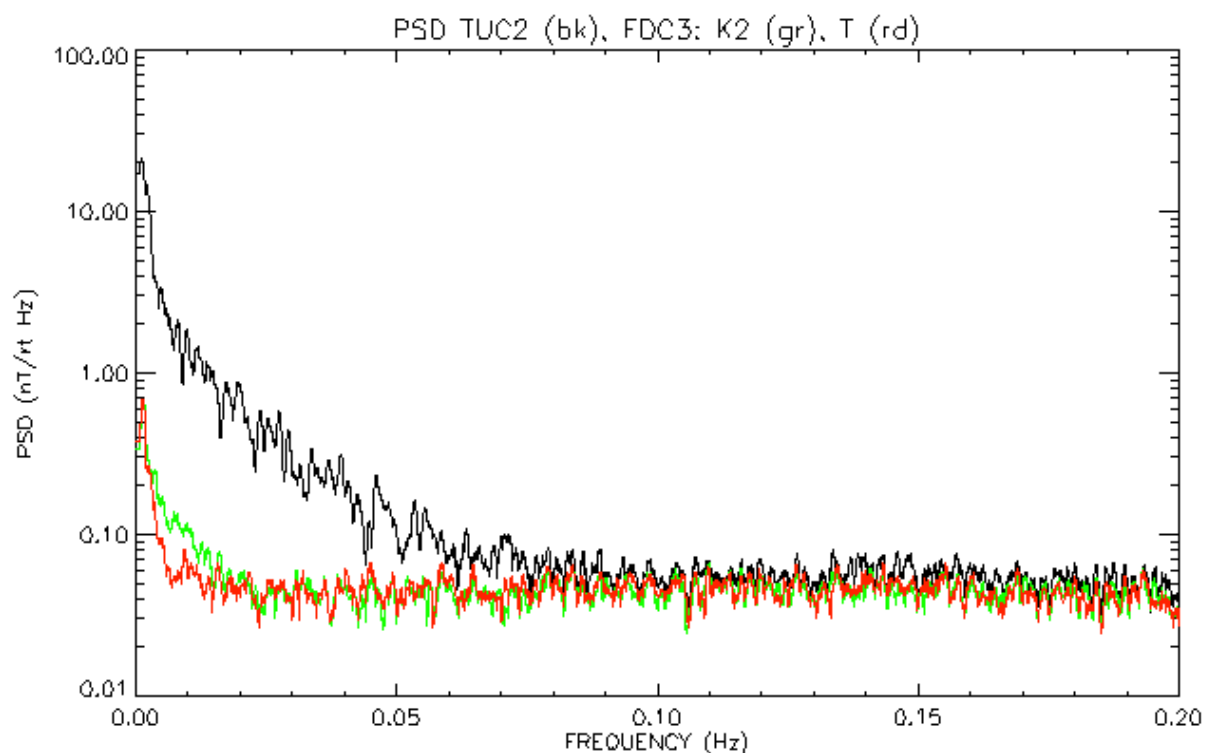


Figure A.47 PSD of TF at TUC2 vs. Res3 for K2 (green), and T (red) for the night of July 12-13.

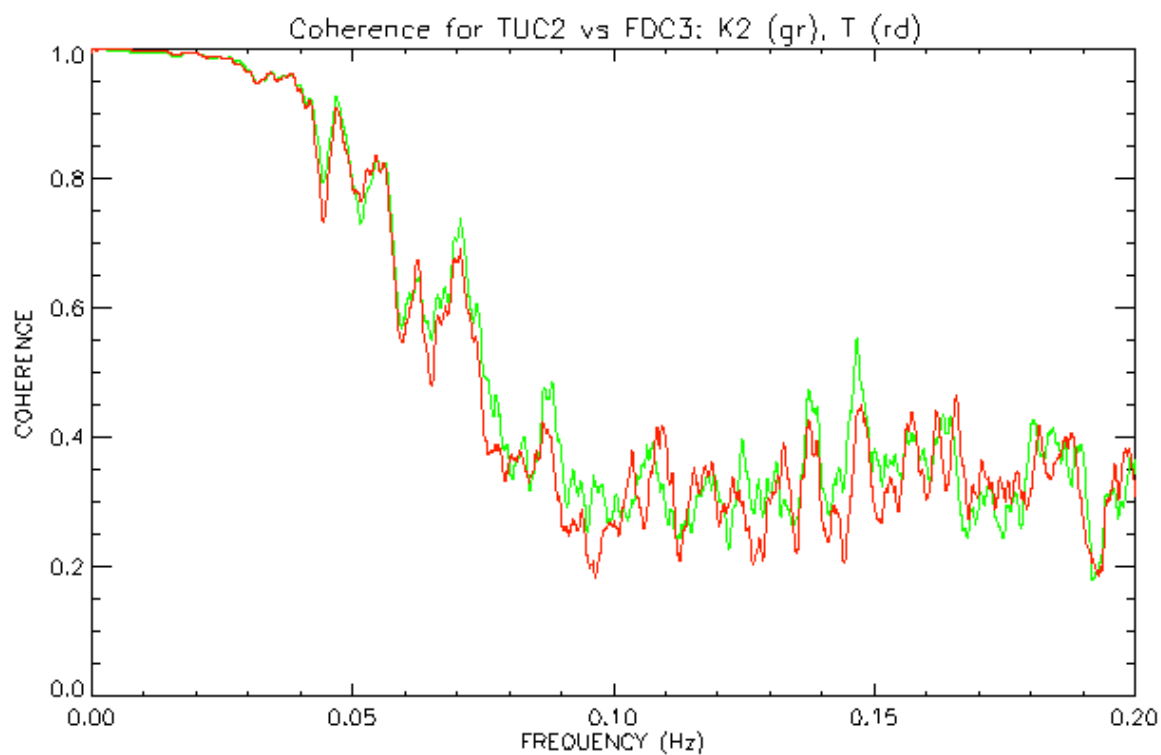


Figure A.48 Coherence of TF at TUC2 vs. (X,Y,Z) at K2 (green), and T (red) for the night of July 12-13.

A.3 Night of July Oct 8-9

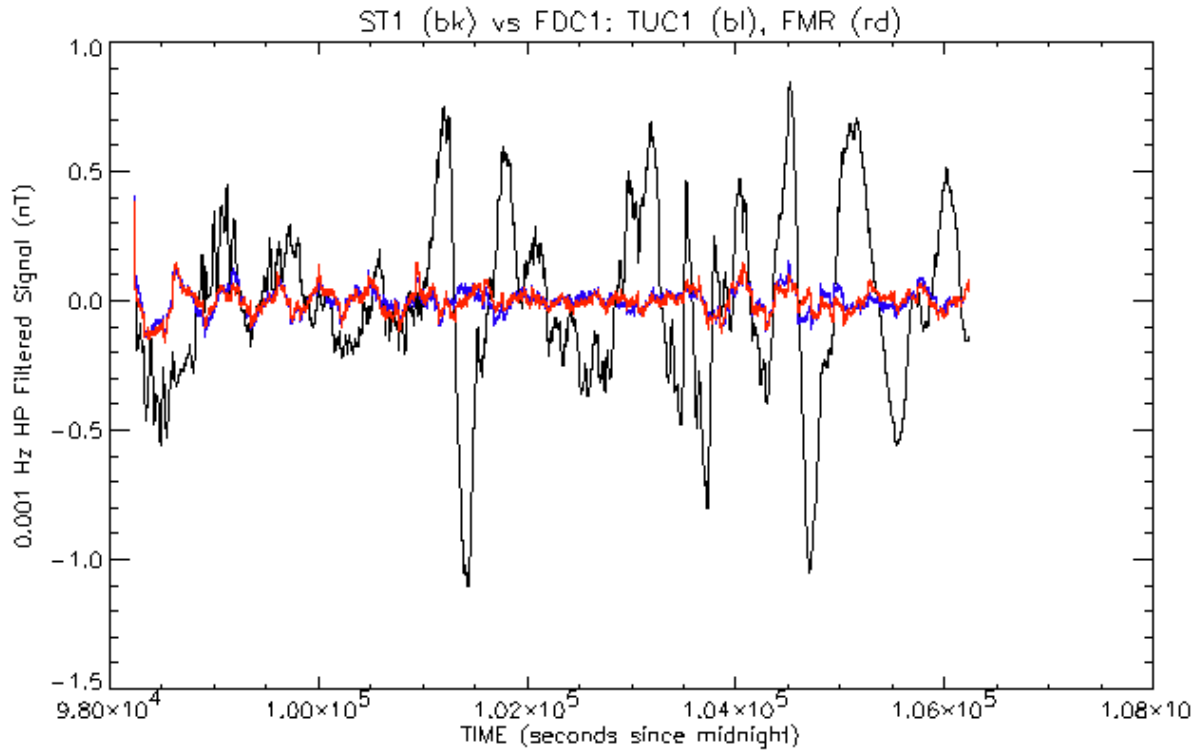


Figure A.49 TF from ST1 (black) vs. Res1 for TUC1(blue), FMR (red) on the night of Oct 8-9.

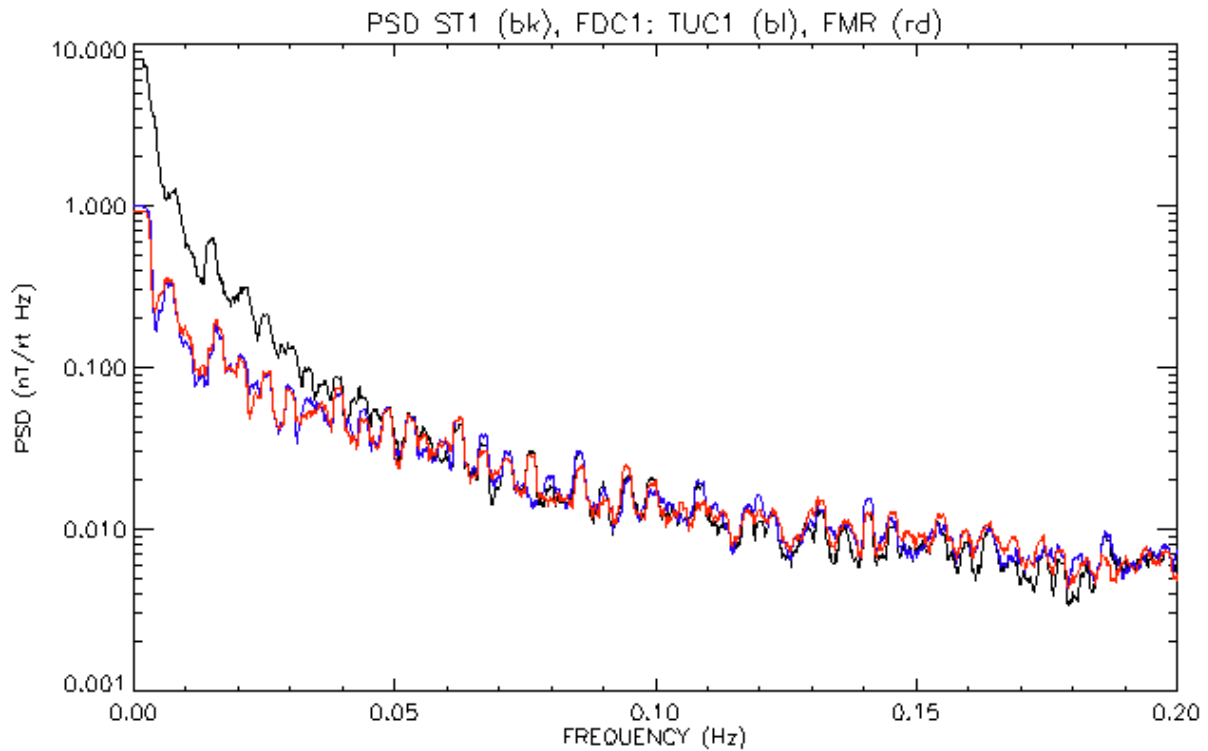


Figure A.50 PSD of TF at ST1 (black) vs. Res1 for TUC1 (blue), and FMR (red) for the night of Oct 8-9.

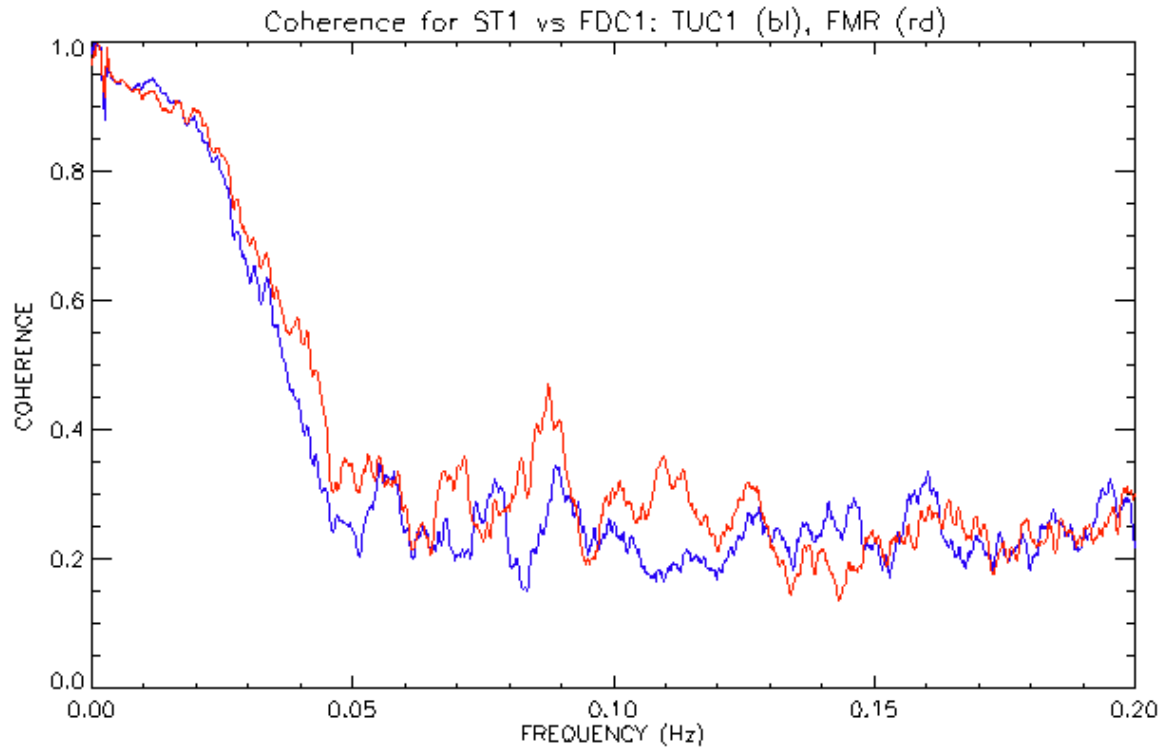


Figure A.51 Coherence of TF at ST1 vs. TF at TUC1 (blue), and FMR (red) for the night of Oct 8-9.

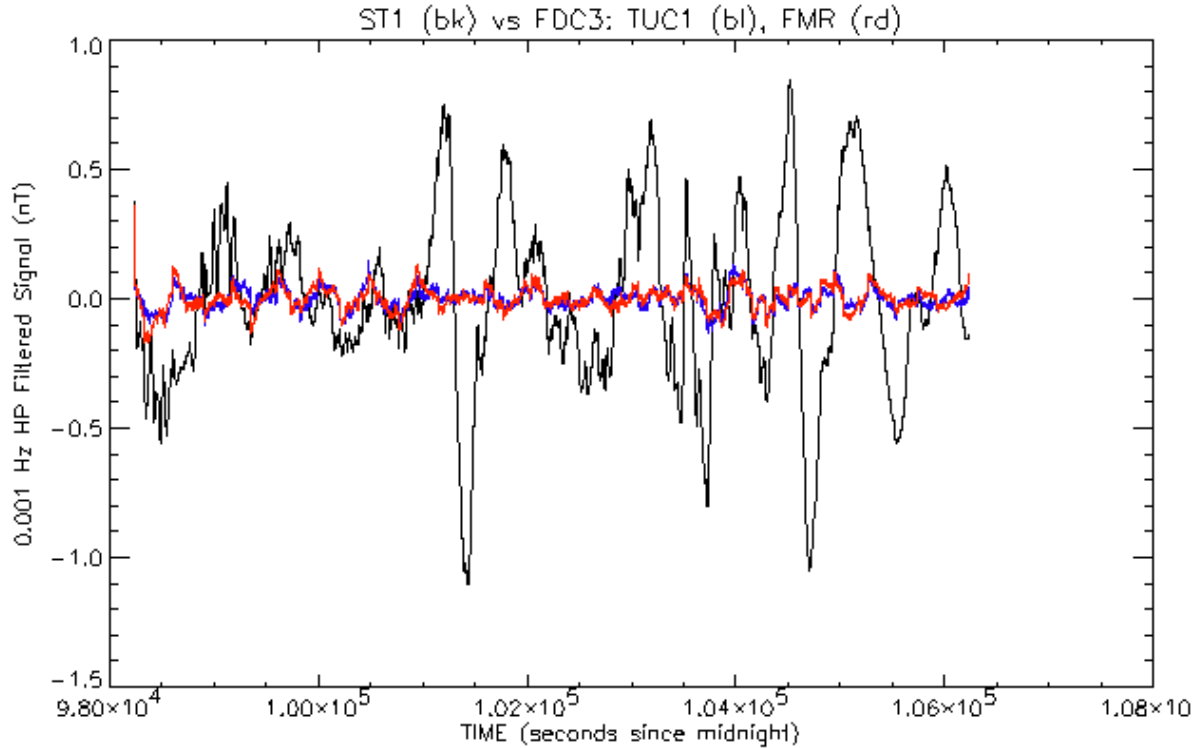


Figure A.52 TF from ST1 (black) vs. Res3 from TUC1 (blue), and FMR (red) on the night of Oct 8-9.

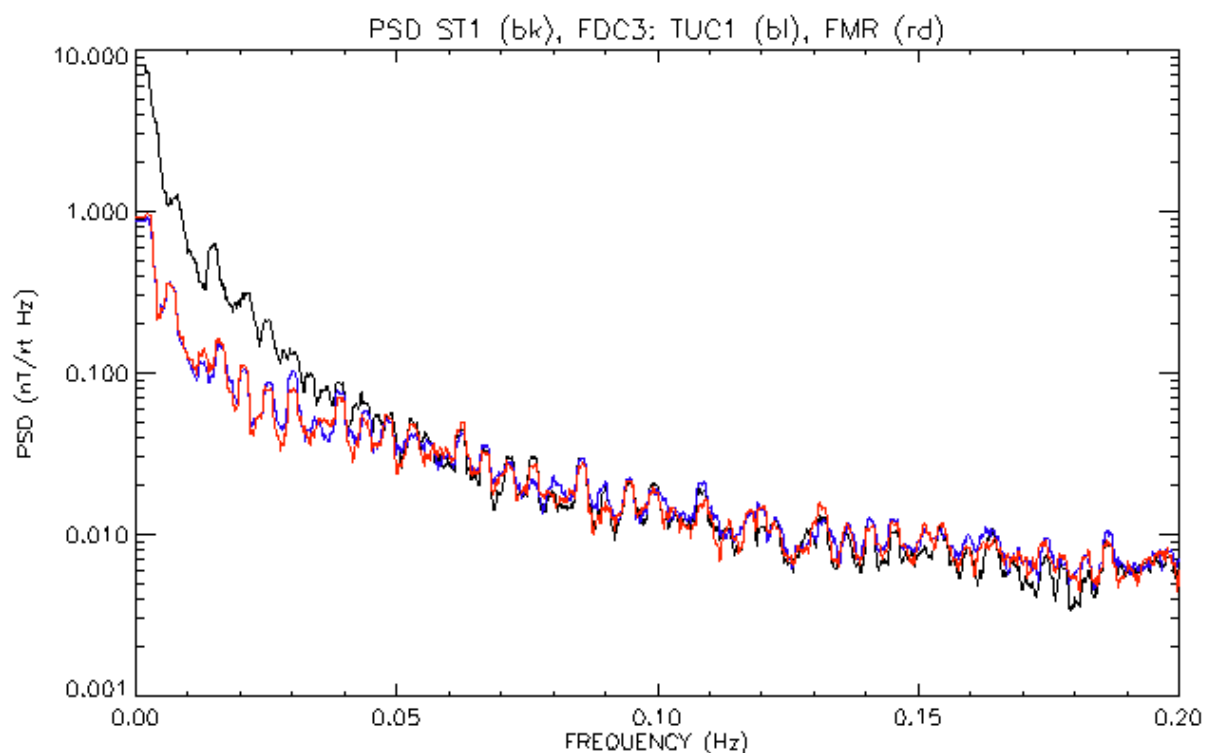


Figure A.53 PSD of TF at ST1 vs. Res3 for TUC1 (blue), and FMR (red) for the night of Oct 8-9.

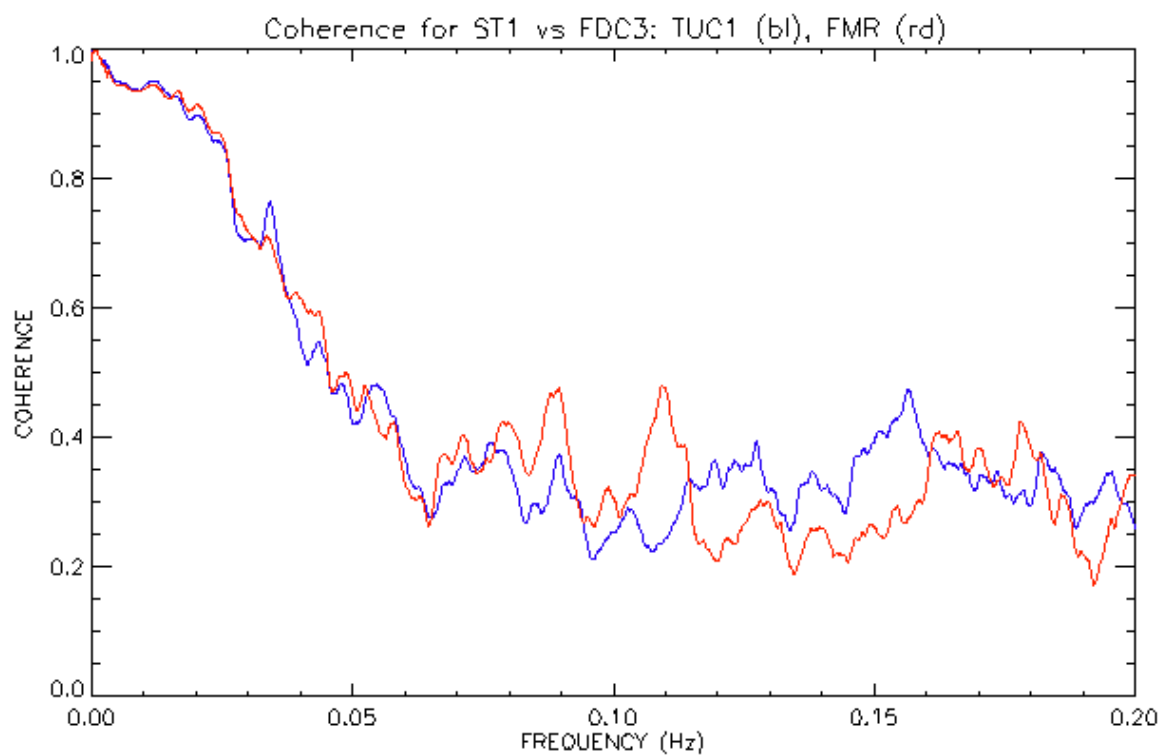


Figure A.54 Coherence of TF at ST1 vs. (X,Y,Z) at TUC1 (blue), and FMR (red) for the night of Oct 8-9.

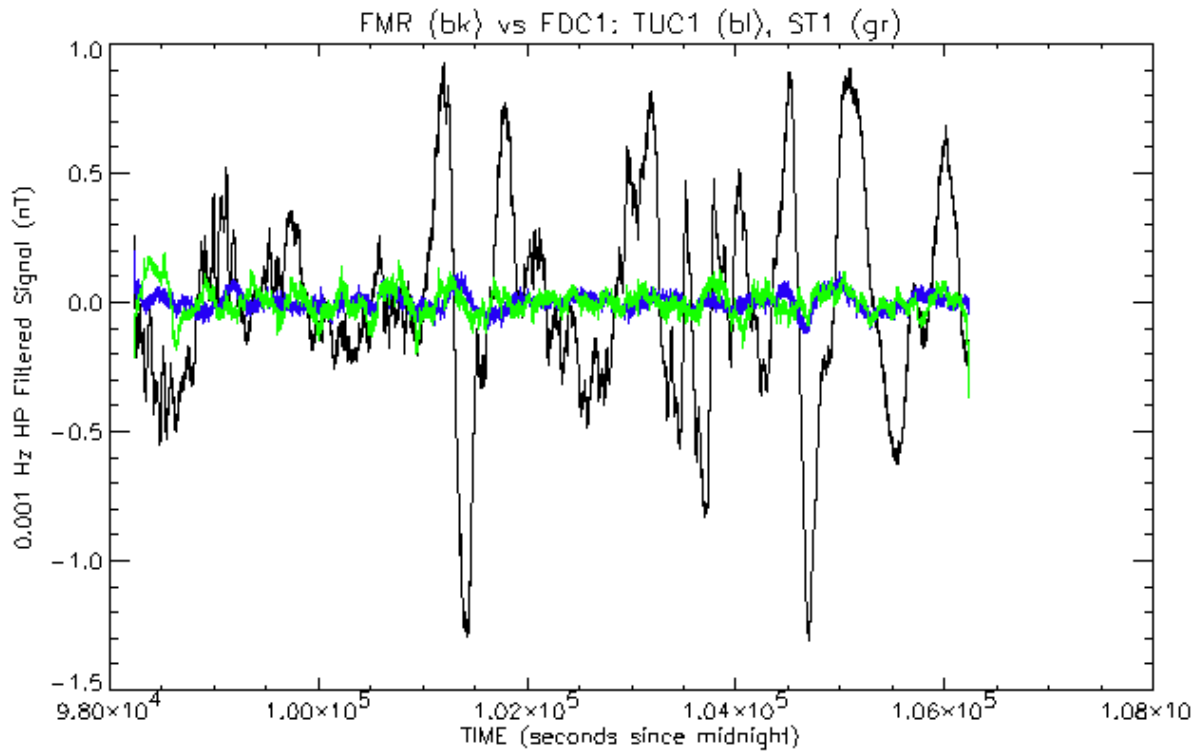


Figure A.55 TF from FMR (black) vs. Res1 for TUC1 (blue), ST1 (green) on the night of Oct 8-9.

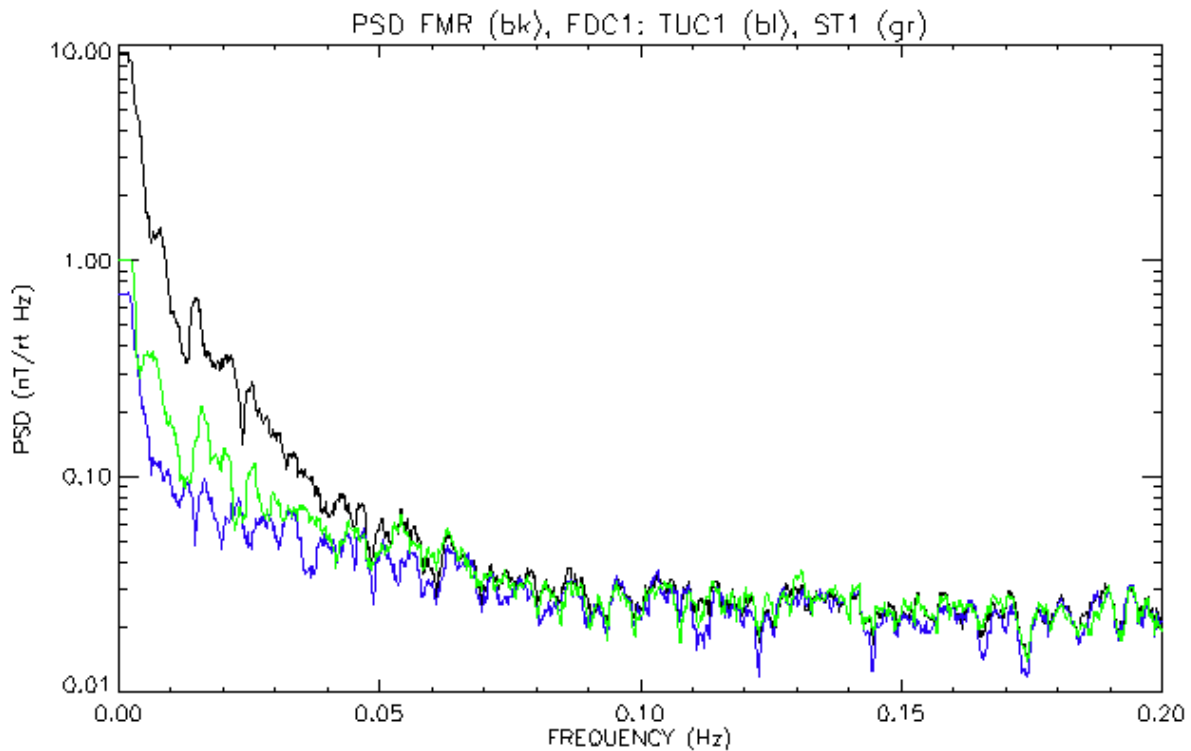


Figure A.56 PSD of TF at FMR (black) vs. Res1 for TUC1 (blue), ST1 (green) for the night of Oct 8-9.

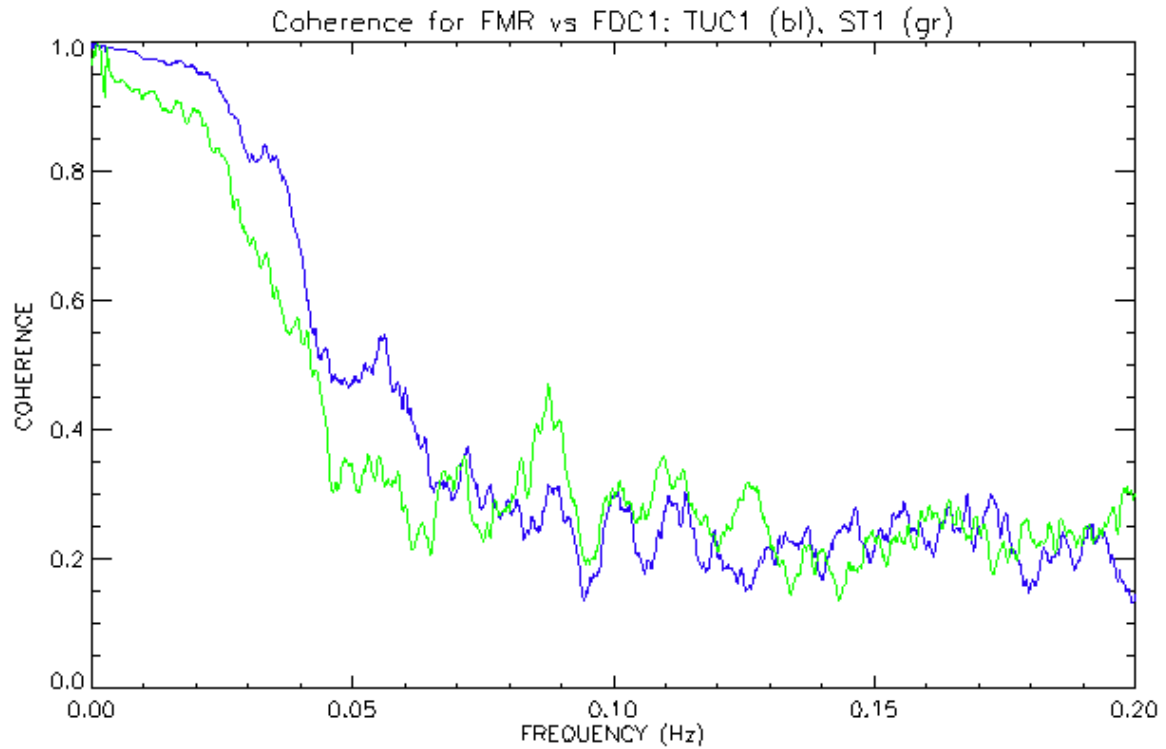


Figure A.57 Coherence of TF at FMR vs. TF at TUC1 (blue), ST1 (green) for the night of Oct 8-9.

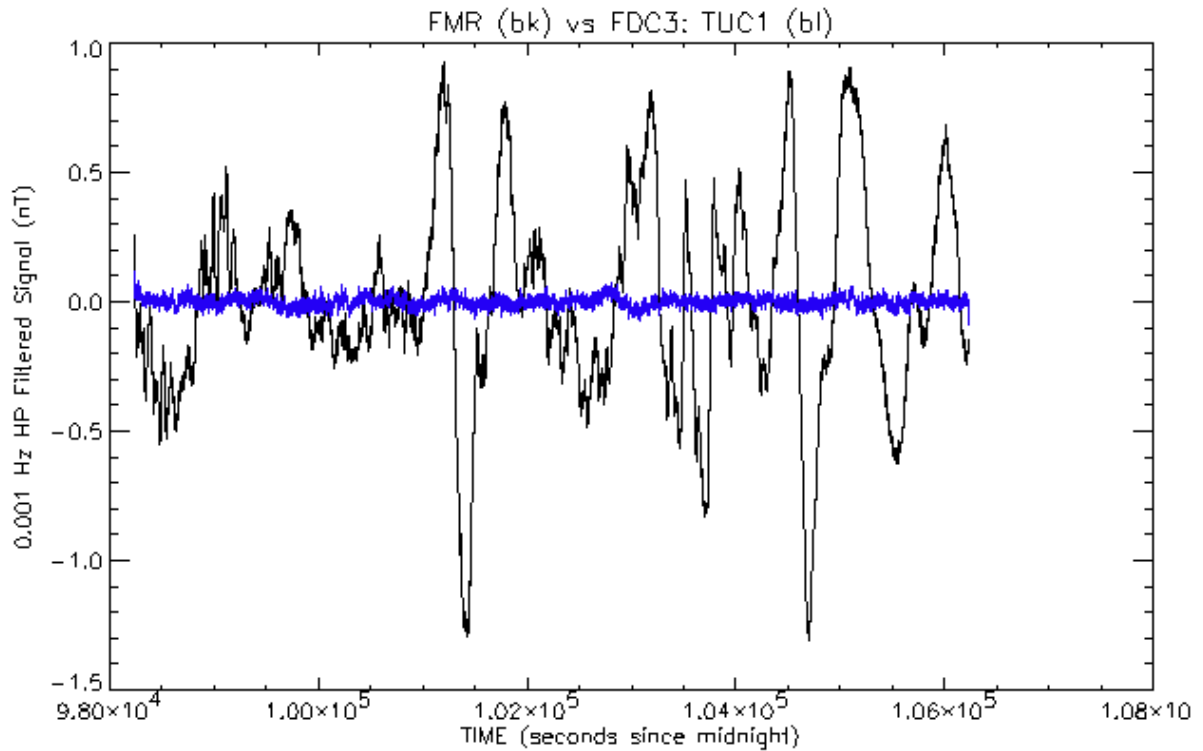


Figure A.58 TF from FMR (black) vs. Res3 from TUC1 (blue) on the night of Oct 8-9.

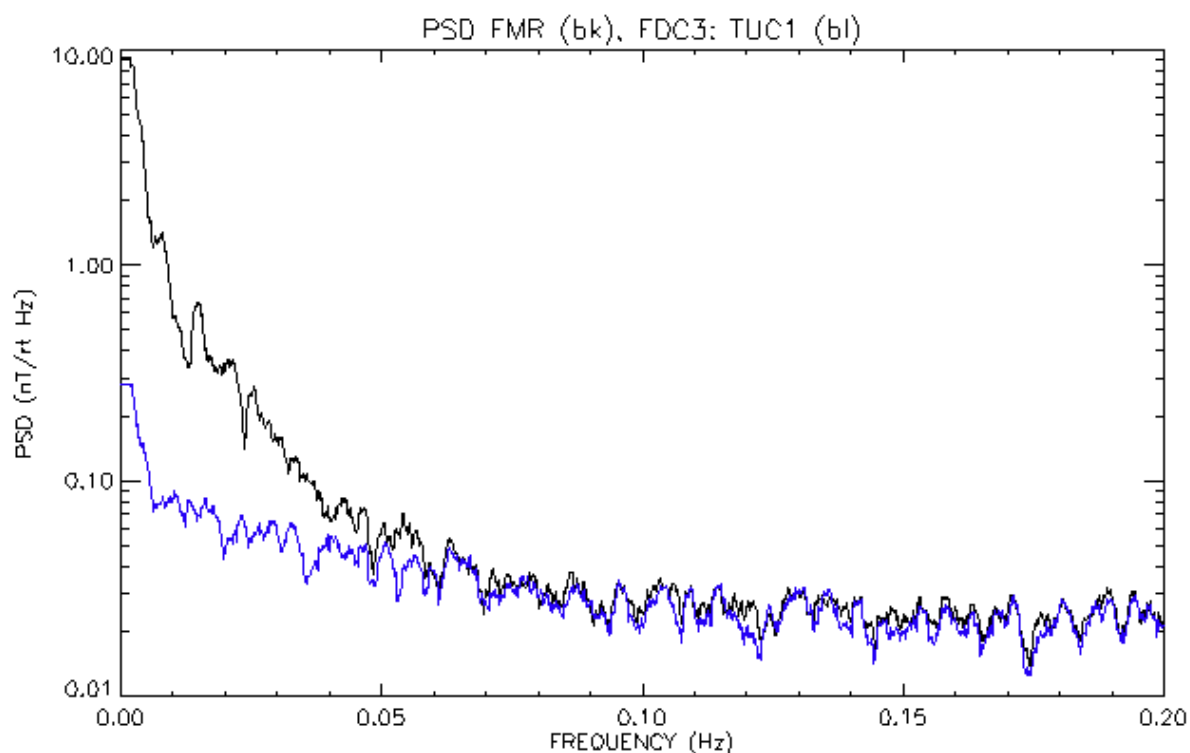


Figure A.59 PSD of TF at FMR vs. Res3 for TUC1 (blue) for the night of Oct 8-9.

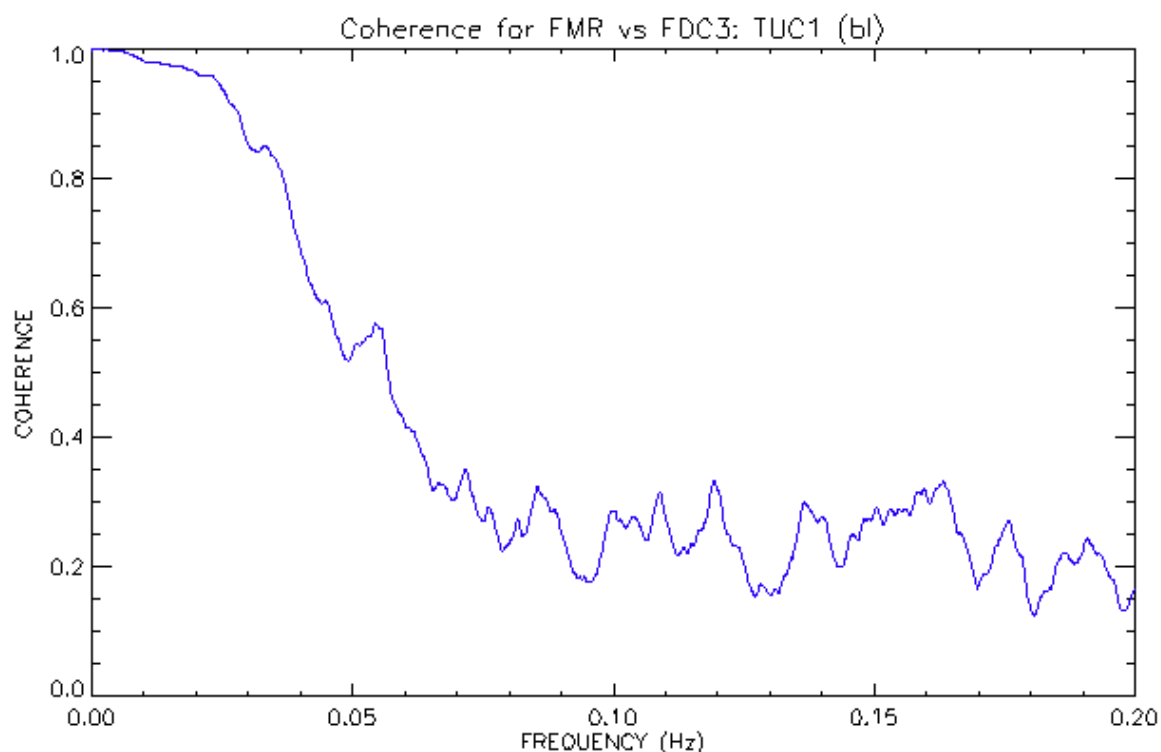


Figure A.60 Coherence of TF at FMR vs. (X,Y,Z) at TUC1 (blue) for the night of Oct 8-9.

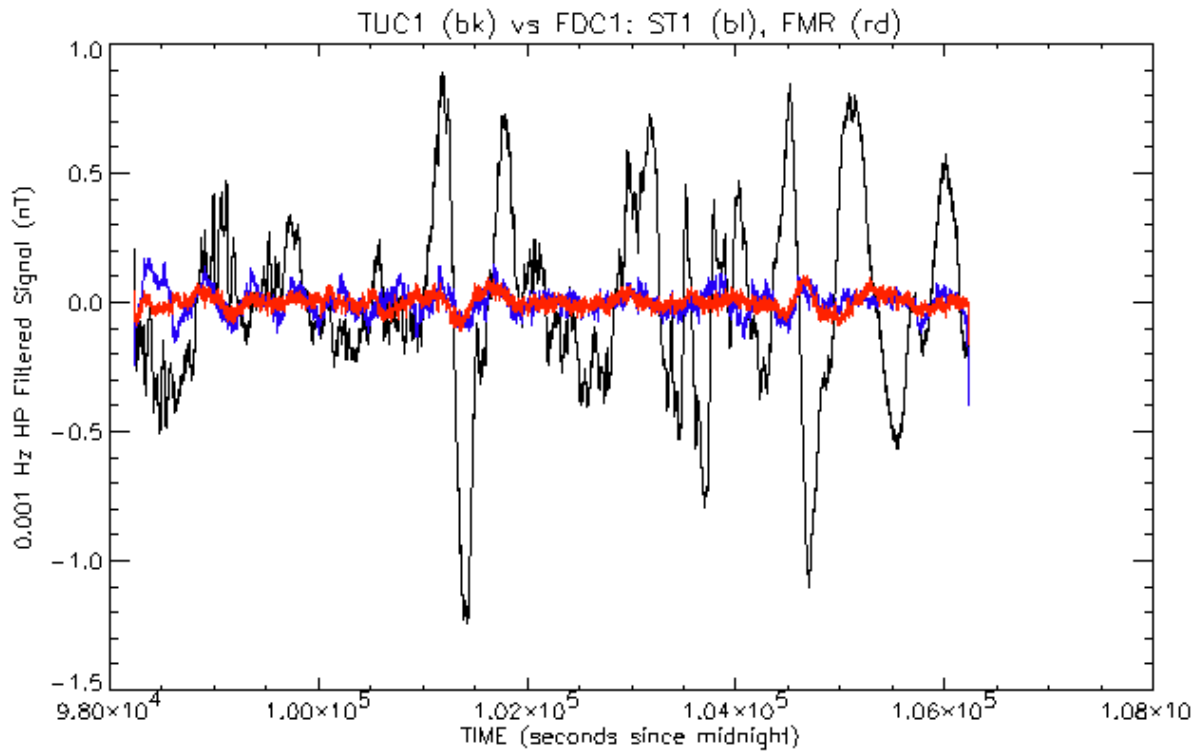


Figure A.61 TF from TUC1 (black) vs. Res1 for ST1 (blue), and FMR (red) on the night of Oct 8-9.

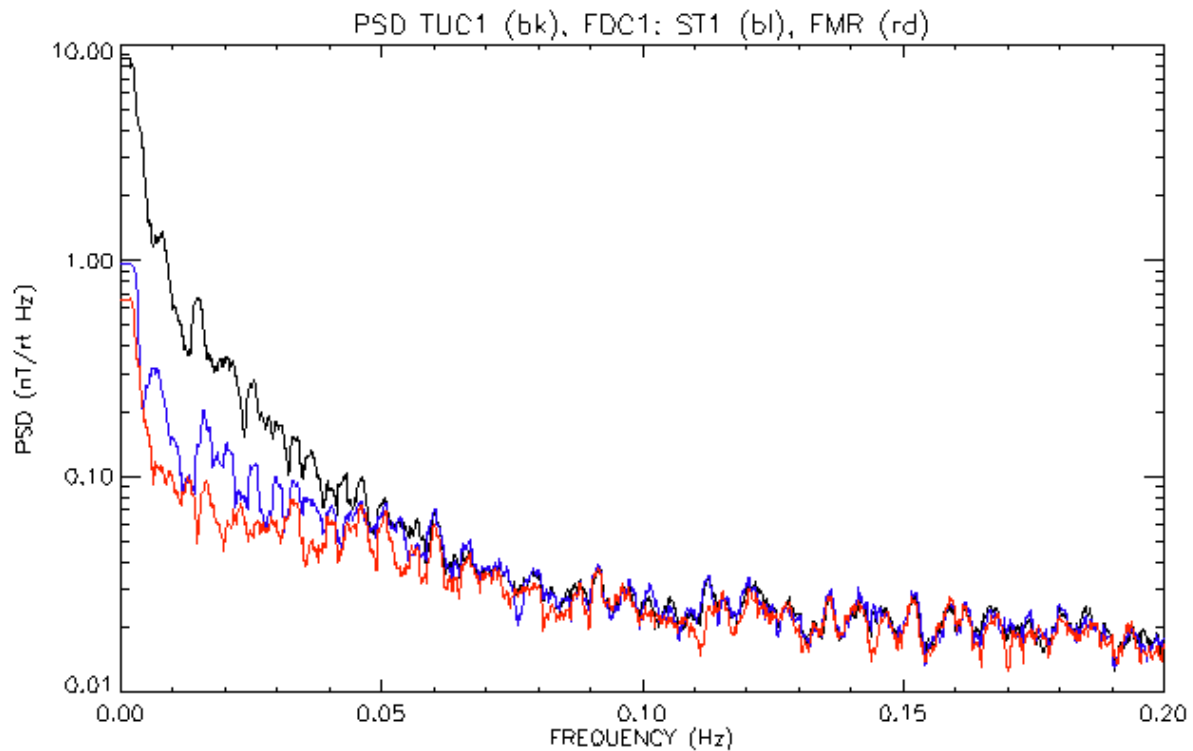


Figure A.62 PSD of TF at TUC1 (black) vs. Res1 for ST1 (blue), and FMR (red) for the night of Oct 8-9.

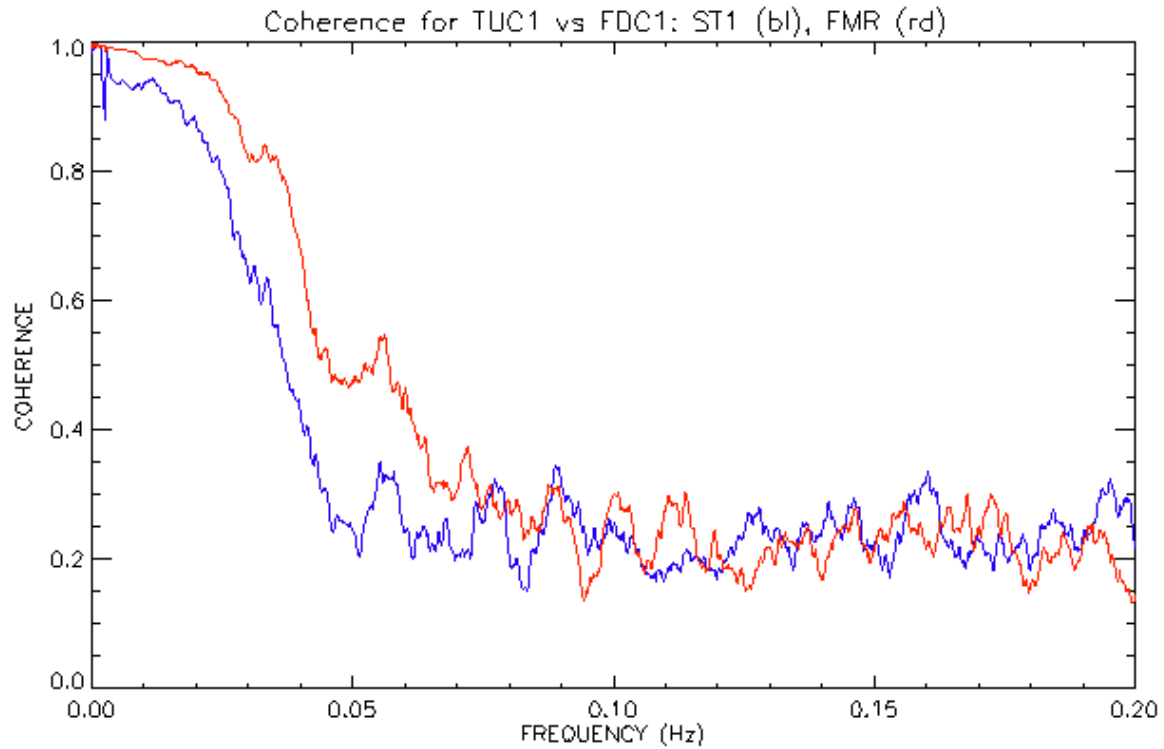


Figure A.63 Coherence of TF at TUC1 vs. TF at ST1 (blue), and FMR (red) for the night of Oct 8-9.

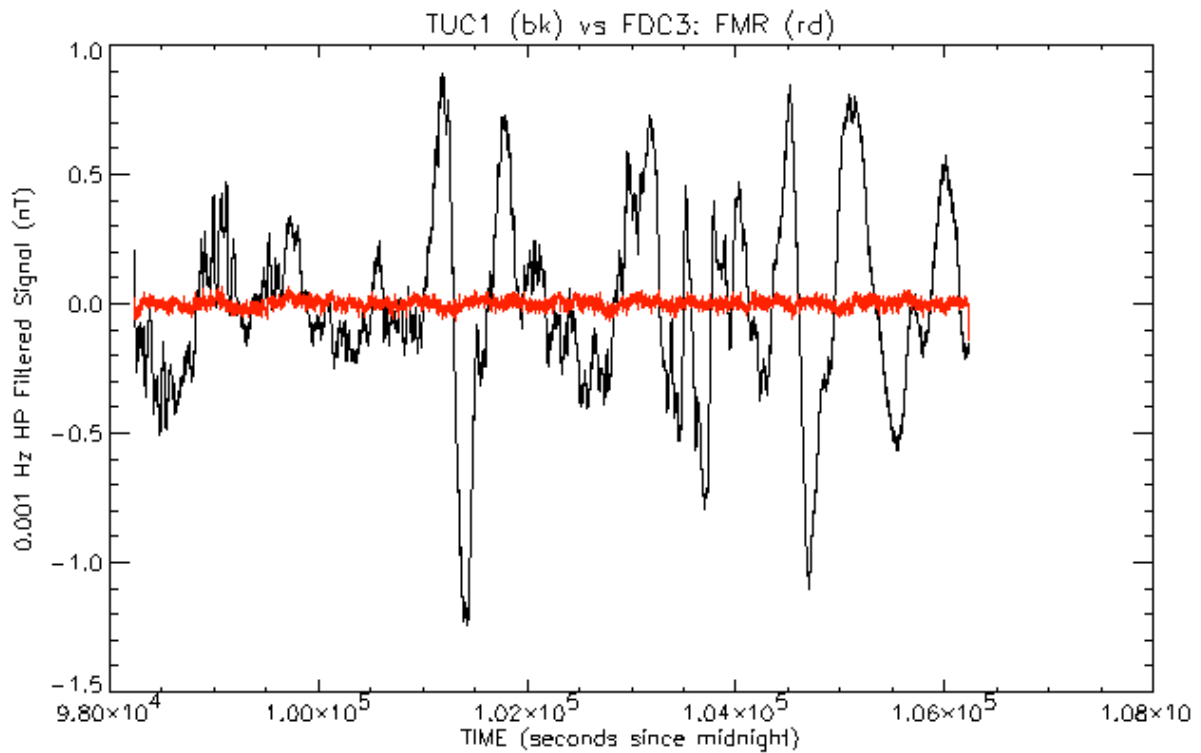


Figure A.64 TF from TUC1 (black) vs. Res3 from FMR (red) on the night of Oct 8-9.

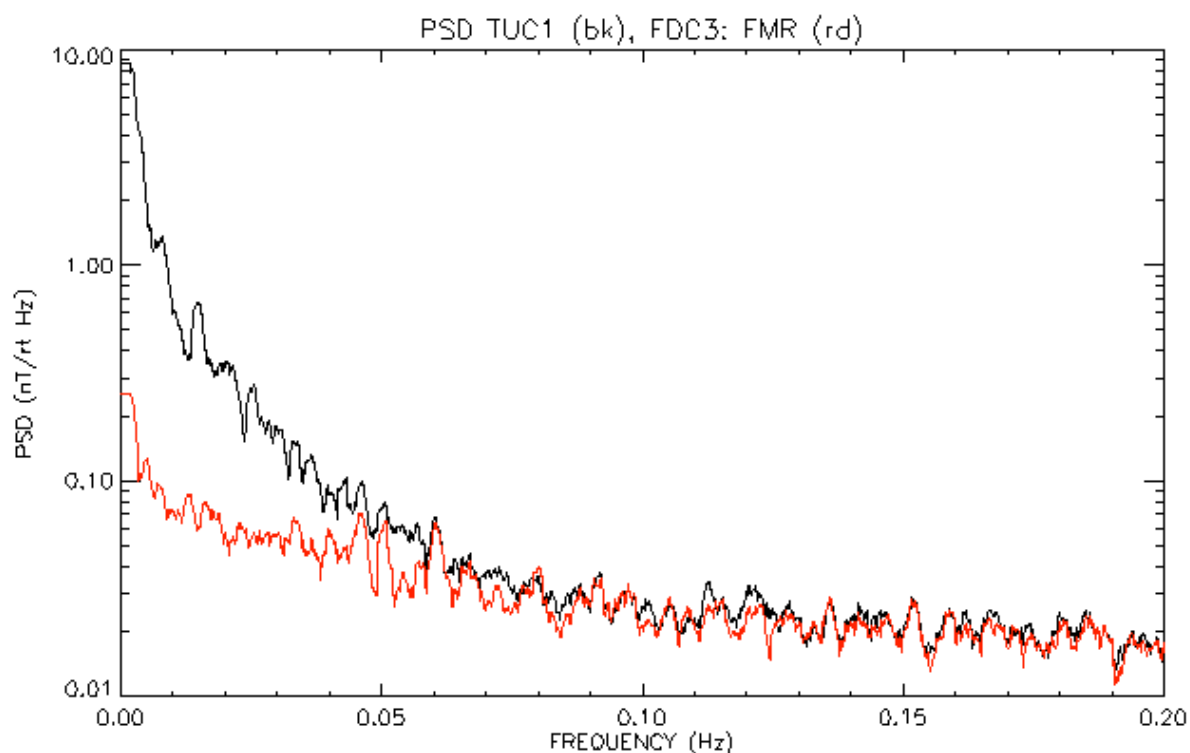


Figure A.65 PSD of TF at TUC1 vs. Res3 for FMR (red) for the night of Oct 8-9.

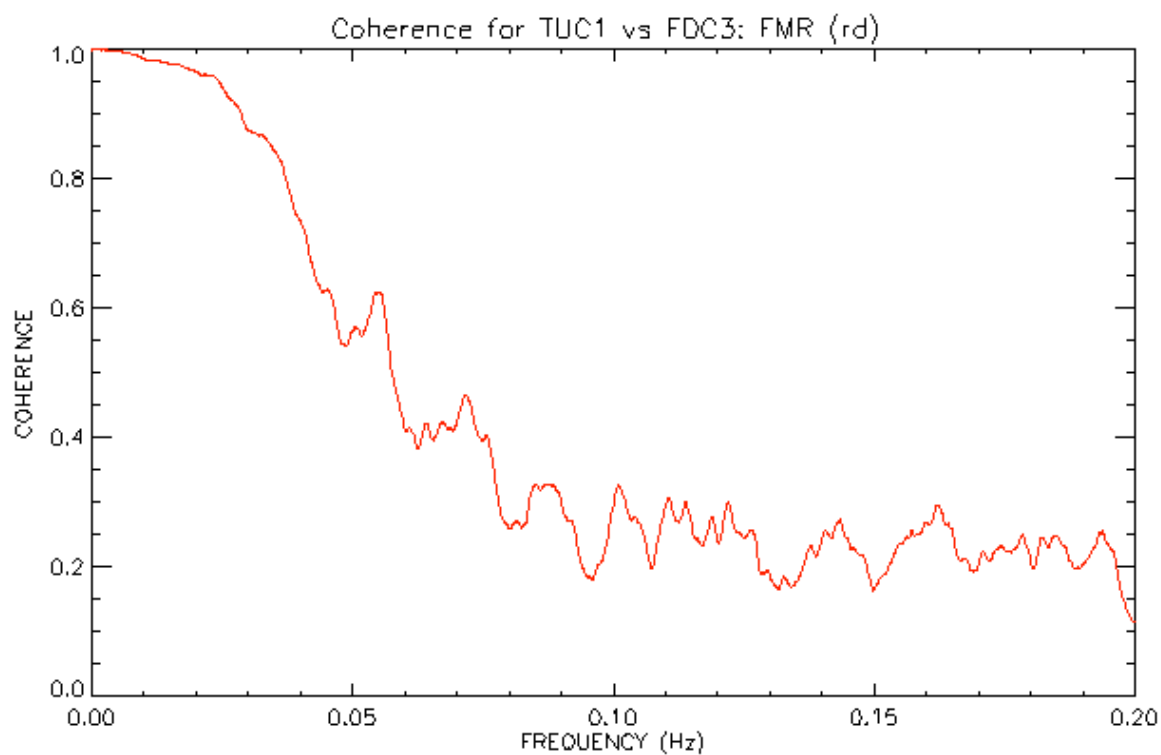


Figure A.66 Coherence of TF at TUC1 vs. (X,Y,Z) at FMR (red) for the night of Oct 8-9.

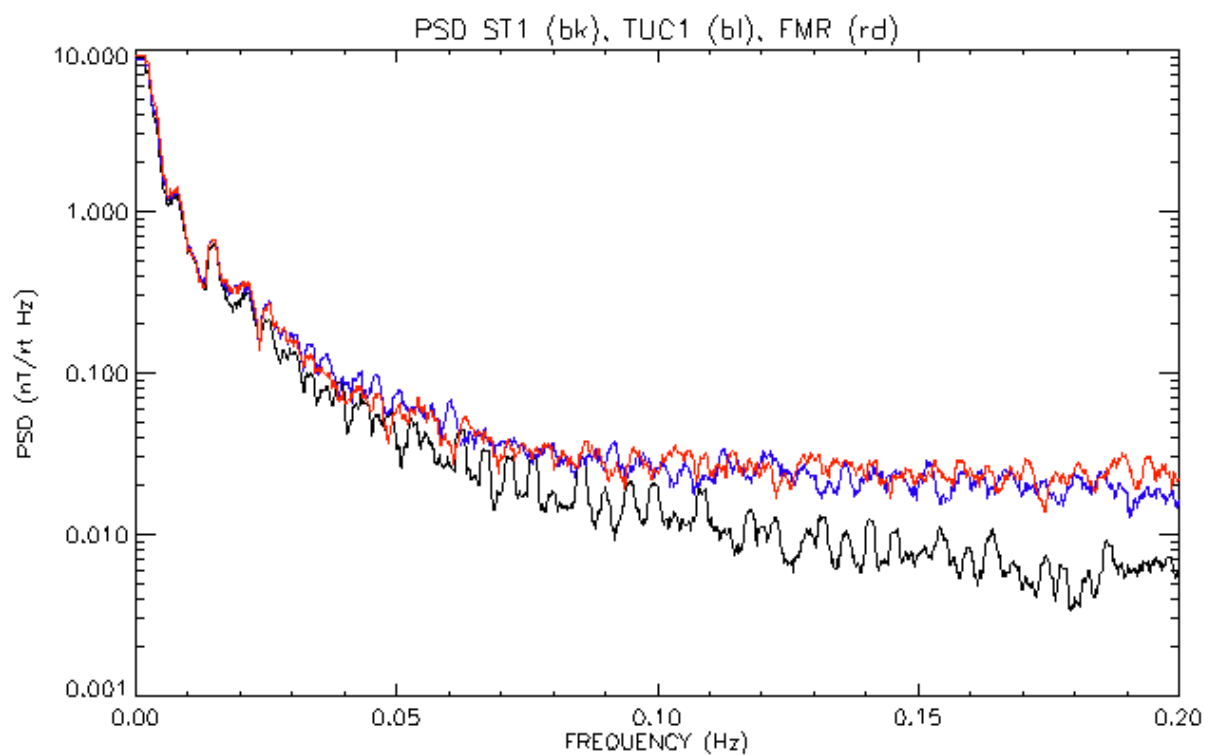


Figure A.67 PSD of TF at TUC1(black) vs. ST1 (blue), and FMR (red) for the night of Oct 8-9.

Distribution List

Report #	ASI-2016- 9 (N62909-15-1-2054-Task 1)
Report Type	Technical Report for Task 1
Title	Coherence of the geomagnetic field and implications for noise reduction using mesospheric magnetometry
Author	J. Bradley Nelson
Organization	Aeromagnetic Solutions Incorporated
Date	1 September 2016
Prepared for	Office of Naval Research Global (ONRG)
Contract/Award #	N62909-15-1-2054
Task #	Task 1
Classification	UNCLASSIFIED
Availability/ Distribution	Approved for Public Release; Distribution Unlimited
Organization/Copies	Address
ONRG (2)	ONRG HQ LIASION OFFICE, 86 Blenheim Crescent, Ruislip MX HA4 7HB
	N62909, 86 Blenheim Crescent, Ruislip MX HA47HB
Defense Technical Information Center (1)	8725 John J Kingman Road Ste 0944, Fort Belvoir, VA 22060-6218
Naval Research Laboratory (1)	ATTN: CODE 5596, 4555 Overlook Avenue SW, Washington, DC 20375-5320
ONR (1)	Attention: Steve Potashnik, 875 N. Randolph St., Arlington, VA, USA, 22203-1995